



8-2019

Virtual Synchronous Generator Operation of Full Converter Wind Turbine – Control and Testing in a Hardware Based Emulation Platform

Yiwei Ma

University of Tennessee, yma13@vols.utk.edu

Follow this and additional works at: https://trace.tennessee.edu/utk_graddiss

Recommended Citation

Ma, Yiwei, "Virtual Synchronous Generator Operation of Full Converter Wind Turbine – Control and Testing in a Hardware Based Emulation Platform. " PhD diss., University of Tennessee, 2019.
https://trace.tennessee.edu/utk_graddiss/5685

This Dissertation is brought to you for free and open access by the Graduate School at Trace: Tennessee Research and Creative Exchange. It has been accepted for inclusion in Doctoral Dissertations by an authorized administrator of Trace: Tennessee Research and Creative Exchange. For more information, please contact trace@utk.edu.

**Virtual Synchronous Generator Operation of
Full Converter Wind Turbine
– Control and Testing in a
Hardware Based Emulation Platform**

**A Dissertation Presented for the
Doctor of Philosophy
Degree
The University of Tennessee, Knoxville**

Yiwei Ma
August 2019

Acknowledgement

First, I would like to express my sincere gratitude to my advisor, Dr. Fred Wang, for his invaluable guidance, encouragement, and support throughout my Ph.D. studies. His knowledge and attitude toward research will definitely benefit both my future career and life. I am also very grateful to Dr. Leon Tolbert for his support, insights and advices during my study. In addition, I would like to thank Dr. Kevin Tomsovic and Dr. Mingzhou Jin for serving as my committee members and giving me suggestions on my dissertation.

The University of Tennessee CURENT center has provided such a great, inspiring and friendly atmosphere. All the faculty members, colleagues and friends here have made my research and life easier. I would like to thank Dr. Yilu Liu, Dr. Kai Sun, Dr. Daniel Costinett, Dr. Fangxing Li, Dr. Chien-fei Chen, Dr. Hua Bai, and Dr. Dong Jiang, Dr. Jingxin Wang, Dr. Mithat Kisacikoglu, Dr. Lakshmi GopiReddy, Dr. Zhuxian Xu, Dr. Fan Xu, Dr. Ben Guo, Dr. Zheyu Zhang, Dr. Jing Xue, Dr. Weimin Zhang, Mr. Bradford Trento, Dr. Bailu Xiao, Dr. Jing Wang, Dr. Yutian Cui, Dr. Wenchao Cao, Dr. Xiaojie Shi, Dr. Zhiqiang Wang, Dr. Yalong Li, Dr. Liu Yang, Ms. Yang Xue, Dr. Bo Liu, Dr. Shiqi Ji, Dr. Edward Jones, Dr. Xiaonan Lu, Dr. Sheng Zheng, Mr. Fei Yang, Dr. Tong Wu, Dr. Mitch Smith, Dr. Shuoting Zhang, Dr. Chongwen Zhao, Dr. Ling Jiang, Dr. Lu Wang, Dr. Ren Ren, Mr. Wen Zhang, Mr. Zhe Yang, Mr. Xingxuan Huang, Ms. Shuyao Wang, Ms. Jingjing Sun, Ms. Jessica Boles, Mr. Handong Gui, Mr. Mark Nakmali, Mr. Saeed Anwar, Mr. Ruirui Chen, Mr. Jacob Dyer, Mr. Geoff Laughon, Mr. Jiahao Niu, Mr. Craig Timms, Ms. Paige Williford, Mr. Dingrui Li, Mr. Haiguo Li, Ms. Le Kong, Mr. Liang Qiao, Mr. Zhou Dong, Mr. James Palmer, Mr. Zihan Gao, Mr. Montie Smith, Dr. Jiahui Guo, Dr.

Lingwei Zhan, Dr. Yin Lei, Dr. Lin Zhu, Dr. He Yin, Dr. Jiaojiao Dong, Mr. Yu Su, Mr. Chengwen Zhang, Ms. Ishita Ray, Dr. Haoyu Yuan, Dr. Xue Li, Dr. Hantao Cui, Dr. Qinran Hu, Dr. Yichen Zhang, Dr. Fengkai Hu, Dr. Weihong Huang, Dr. Xiaohu Zhang, and many many more... It was really a great honor and a pleasure to work with them, and those fond memories will be forever cherished.

I also owe my gratitude to all the staff members, including but not limited to, Mr. Robert Martin, Ms. Judy Evans, Mr. Erin Wills, Mr. Chris Anderson, Mr. Jay Cooley, Ms. Wendy Smith, Ms. Anne Skutnik, Mr. Ryan Smiley, Ms. Lisa Beard and Ms. Dana Bryson. Their professional help have always been reliable.

Finally, but most importantly, I would like to thank my dearest parents Yan Ma, Jie Li, and my wife Xingru Yan for their unconditional belief and love.

This dissertation was supported primarily by the Engineering Research Center Program of the National Science Foundation and Department of Energy under NSF Award Number EEC-1041877 and the CURENT Industry Partnership Program.

Abstract

Wind is one of the most promising renewable energy forms that can be harvested into the electrical power system. The high penetration of wind energy has brought about a number of difficulties to the power system operation due to its stochastic nature, lack of exhibited inertia, and differing responses to the traditional energy sources in grid disturbances. Various grid support functions have been proposed to resolve the issues. One solution is to allow the renewable energy sources to behave like a traditional synchronous generator in the system, as a virtual synchronous generator (VSG). On the other hand, testing the control of the future power grid with high penetration renewable often relies on digital simulation or hardware-based experiments. But they either suffer from fidelity and numerical stability issues, or are bulky and inflexible. A hardware testbed (HTB) is built to allow testing of both system level and component level controls, with a balance between fidelity and flexibility

This dissertation proposal investigates the VSG operation of the full converter wind turbine (FCWT), focusing on its control and testing in the HTB. Specifically, a FCWT emulator was developed using a single converter to include its physical model and control strategies. The existing grid support functions are also included to demonstrate their feasibility.

Comprehensive VSG controls are then proposed for a FCWT with short term energy storage. The dynamic response of the FCWT can be comparable to the traditional generation during grid disturbance. The control can also allow the FCWT to be dispatched by the system operator, and even operate stand-alone without other grid sources.

To study the system response under faults, a short circuit fault emulator was developed in the

HTB platform. Four basic types of short circuit faults with various fault impedance can be emulated using the emulator. The power system transient stability in terms of critical clearing time can be measured using the developed fault emulator.

Finally, operation of the VSG controlled FCWT under grid faults was studied. The impact of system transient stability is analyzed, and controls to improve it are proposed.

Table of Contents

1	Introduction	1
1.1	Background and Motivation.....	1
1.2	Dissertation Organization.....	4
2	Literature Review and Challenges	6
2.1	Power System Testing Methods.....	6
2.1.1	Digital Simulation	6
2.1.2	Hardware Based Testing	7
2.2	Hardware Testbed at CURENT Center in University of Tennessee, Knoxville [27]	8
2.2.1	Emulation Principle and Structure	9
2.2.2	Communication and Control Architecture	15
2.2.3	System Emulation Demonstration.....	18
2.2.4	Comparison of Existing Power System Testing Methods and Identified Needs	21
2.3	Wind Turbine Emulation Methods.....	24
2.4	Fault Emulation Methods.....	25
2.5	Grid Support Functions from Full Converter Wind Turbines.....	28
2.5.1	Basic Operation and Grid Support Functions of FCWT	28
2.5.2	Virtual Synchronous Generator Control.....	30
2.5.3	Operation of FCWT under Large Disturbance	31
2.6	Research Objectives	33
3	Emulating Full-Converter Wind Turbine in HTB Testing Environment.....	35
3.1	Developed Full-Converter Wind Turbine Model.....	35
3.1.1	Overview	35

3.1.2	Wind Model.....	36
3.1.3	PMSG Model.....	37
3.1.4	Converter Model.....	38
3.1.5	Control Functions Implemented into the FCWT Emulator.....	39
3.1.6	Emulator Output Current Reference.....	43
3.2	Simulation Results.....	44
3.3	Experiment	45
3.3.1	Case I: Short Period Variable Wind Speed Test	45
3.3.2	Case II: Long Period Variable Wind Speed Test	48
3.3.3	Case III: Frequency Support by Wind Turbine Test	49
3.3.4	Case IV: Two Area System Frequency Oscillation Test.....	50
3.3.5	Case V: Operation with Low Terminal Voltages	51
3.4	Discussion	52
3.5	Conclusion.....	53
4	Virtual Synchronous Generator Control of Full Converter Wind Turbine with Short Term Energy Storage	54
4.1	Structure and Basic Control Principle.....	54
4.2	Detailed Control Strategy.....	57
4.2.1	Grid Side Converter Control	57
4.2.2	Storage Side Converter Control	61
4.2.3	Machine Side Converter Control.....	61
4.2.4	Pitch Control.....	64
4.2.5	Discussion on Sizing of the Energy Storage	65
4.3	Experimental Results.....	67

4.3.1	Experiment Platform	67
4.3.2	Control Parameters	68
4.3.3	Grid Connected Operation of Proposed VSG Control	69
4.3.4	Stand-alone Operation of Proposed VSG Control	71
4.3.5	Current Limiting Operation During Fault	74
4.4	Conclusion.....	75
5	Short Circuit Fault Emulation in HTB Testing Environment	77
5.1	Operating Principle and Hardware Requirement for the Fault Emulator Converter.....	77
5.2	Control Strategies for the Fault Emulator Converter	79
5.2.1	Single-line-to-ground Fault	79
5.2.2	Double-line-to-ground Fault.....	81
5.2.3	Line-to-line Fault.....	82
5.2.4	Three-phase Short Circuit Fault	83
5.3	Hardware Based Testing Platform and Corresponding Controller Design	84
5.3.1	Control Parameter Design	85
5.3.2	Discussion	88
5.4	Experimental Results.....	91
5.4.1	Verification of Proposed Short Circuit Emulator.....	91
5.4.2	Application to Determine Critical Clearing Time	95
5.5	Conclusion.....	99
6	Enhancing Power System Transient Stability by VSG Control Using Wide-area Measurements	101
6.1	Previous VSG Control Method to Improve System Stability	101
6.2	Limitation Previous Methods and Proposed Control	103

6.3	Experiment Implementation and Test Results	107
6.3.1	Experimental platform.....	107
6.3.2	Implementation of Proposed Control	108
6.3.3	Experimental Results.....	110
6.4	Practicality Discussion	114
6.5	Conclusion.....	114
7	Impact of Limited Current to System Transient Stability and Its Mitigation.....	115
7.1	Transient Stability Analysis in a Single Machine Infinite Bus System	115
7.2	Impact of Limited Current in Single Machine Infinite Bus System	117
7.3	Proposed Control to Enhance Transient Stability When Current is Limited	121
7.4	Experimental Result in HTB	123
7.5	Limitation and Discussion.....	126
7.6	Conclusion.....	126
8	Conclusions and Future Work	128
8.1	Summary	128
8.2	Contribution	128
8.3	Recommended Future Work	129
	Reference	131
	Vita	144

List of Figures

Figure 1-1. Types of wind turbines.....	2
Figure 2-1. Emulator operating principles [27].	9
Figure 2-2. Structure of the HTB [27].	11
Figure 2-3. Power system emulation topology configurations in HTB [27].	12
Figure 2-4. Reconfiguration scheme of the HTB and emulator cabinet configuration [27].....	14
Figure 2-5. Photo of HTB Type II reconfiguration cabinet [27].	14
Figure 2-6. Photo of HTB Type I and Type III reconfiguration cabinet [27].....	15
Figure 2-7. Communication structure of HTB [27].	16
Figure 2-8. Control architecture of HTB [27].....	18
Figure 2-9. Test results of wide area damping control for two area system [27].	19
Figure 2-10. Test results of real-time voltage stability assessment and control in three area system [27].....	20
Figure 2-11. Test results of remedial action scheme of controlled separation for four area system [27].....	21
Figure 2-12. Test results of harmonic stability problem [27].	22
Figure 2-13. Two types of wind turbine emulator configurations.	24
Figure 2-14. Schematics of the fault emulators [79].....	27

Figure 3-1. Block diagram of the model of the wind turbine emulator [136].	36
Figure 3-2. Implemented control functions of the FCWT emulator.	40
Figure 3-3. Hierarchical control diagram of full-converter wind turbine [136].	41
Figure 3-4. Power reference calculation with MPPT and frequency support function [136].	41
Figure 3-5. MPPT characteristic of FCWT emulator [136].	42
Figure 3-6. Implemented reactive power control for FCWT emulator [136].	43
Figure 3-7. Approaches of current reference selection.	44
Figure 3-8. Simulation waveforms of wind turbine output power, turbine speed and pitch angle by switching model and emulator model [136].	46
Figure 3-9. Experimental waveforms when emulated wind speed change [136].	48
Figure 3-10. Experimental results of FCWT operation in a 50% penetration system.	49
Figure 3-11. Experiment waveforms of grid frequency, turbine speed, and wind turbine output power during frequency drop disturbance [136].	50
Figure 3-12. Experiment waveforms of grid frequencies of two area system with wind turbine penetration [136].	51
Figure 3-13. Experimental results of FCWT fault operation.	52
Figure 3-14. System level control of the FCWT.	53
Figure 4-1. FCWT system under study [139].	54
Figure 4-2. Operation diagram for VSG controlled FCWT [139].	56

Figure 4-3. Operation state machine for VSG controlled FCWT [139].	56
Figure 4-4. GSC control to mimic SG behavior in power system: (a) overall control diagram; (b) electrical model; (c) mechanical model [139].	58
Figure 4-5. GSC inner closed-loop output voltage control for d axis: (a) single loop; (b) double loop with inner current control loop [139].	60
Figure 4-6. SSC control to maintain dc voltage [139].	61
Figure 4-7. MSC control to adjust turbine rotor speed [139].	62
Figure 4-8. Wind characteristic curve showing the sector definition and pre-determined MPP curve $f(\omega)$ [139].	63
Figure 4-9. Pitch control to reduce excessive power [139].	65
Figure 4-10. Emulated two-area system topology [139].	68
Figure 4-11. Experimental results of grid-connected operation with mode transitions between VSG normal operation and VSG MPPT mode [139].	70
Figure 4-12. Grid-connected operation experimental results to compare traditional MPPT and VSG MPPT mode [139].	71
Figure 4-13. Experimental results with variable wind speed showing VSG mode carry out the dispatch commands [139].	72
Figure 4-14. Experimental results of dynamic performance of the VSG control showing better frequency responses [139].	72

Figure 4-15. Experimental results of FCWT in stand-alone condition, adjusting the operating points to accommodate the load [139].	73
Figure 4-16. Fault operation experimental results showing FCWT terminal voltage and output current. (a) without current limits, (b) with current limits [139].	74
Figure 5-1. Schematics of the shunt connected fault emulator converter [79].	78
Figure 5-2. Equivalent circuit of the fault emulator converter.	79
Figure 5-3. Control block diagram of single-line-to-ground fault for phase a [79].	80
Figure 5-4. Single phase control block diagram with electrical model in abc axis.	81
Figure 5-5. Control block diagram of double-line-to-ground fault for phase a and phase b [79].	82
Figure 5-6. Control block diagram of line-to-line fault for phase a and b [79].	83
Figure 5-7. Current control block diagram for line-to-line fault with electrical model in abc axis.	84
Figure 5-8. Control block diagram of three-phase fault control in dq axis. [79].	85
Figure 5-9. Bode plot of open loop transfer function of V_F/V_F^* in abc axis for single-line-to-ground, double-line-to-ground and line-to-line fault emulations.	87
Figure 5-10. Bode plot of closed loop transfer function of V_F/E_{Thev} in abc axis for single-line-to-ground, double-line-to-ground and line-to-line fault emulations.	87
Figure 5-11. Bode plot of open loop transfer function of I_F/V_F^* in abc axis for line-to-line fault emulation.	89

Figure 5-12. Bode plot of closed loop transfer function of I_F/E_{Thev} in abc axis for line-to-line fault emulation.....	89
Figure 5-13. Experimental results of single-line-to-ground short circuit with 1 Ω grounding resistance [79].	92
Figure 5-14. Experimental results of single-line-to-ground short circuit with 1 Ω pure inductive grounding impedance [79].	92
Figure 5-15. Experimental results of double-line-to-ground short circuit [79].	93
Figure 5-16. Experimental results of line-to-line short circuit [79].	94
Figure 5-17. Experimental measurement of voltages for three-phase short circuit [79].	94
Figure 5-18. Experimental measurement of currents for three-phase short circuit [79].	95
Figure 5-19. Experimental results of a series three-phase short circuit fault at two-area system to determine the critical clearing time.....	96
Figure 5-20. Oscilloscope measurements of a series three-phase short circuit fault at two-area system to determine the critical clearing time.	97
Figure 5-21. Simulated generator frequencies in cases of three-phase short circuit faults with different fault clearing time, in comparison with experimental results.	98
Figure 5-22. Simulated generator output powers in cases of three-phase short circuit faults with different fault clearing time, in comparison with experimental results.	98
Figure 5-23. Simulated angle differences between G1 and G3, in cases of three-phase short circuit faults with different fault clearing time.	99

Figure 6-1. Adaptive frequency changing method during transient to minimize frequency disturbance.	102
Figure 6-2. Simulation results comparison of applying adaptive inertia control of VSG with different fault location.....	105
Figure 6-3. System frequency after load bus 9 fault.....	106
Figure 6-4. Simulation results of applying improved adaptive inertia control of VSG with different fault location.	108
Figure 6-5. Measured time-delay.....	109
Figure 6-6. Experimental result for Case 3 with 0.26 s fault clearing time using literature method.	112
Figure 6-7. Experimental result for Case 3 with 0.36 s fault clearing time using proposed method.	113
Figure 6-8. Experimental result comparison for Case 2 with 0.28 s fault clearing time with different controls.....	113
Figure 7-1. Simulation configuration for single machine infinite bus system.....	116
Figure 7-2. System response for a short circuit fault in a single machine infinite bus system, without current limitation.	118
Figure 7-3. Diagram of VSG voltage closed-loop control.....	119
Figure 7-4. Current limitation methods.	120

Figure 7-5. System response for a short circuit fault in a single machine infinite bus system, with limited current.	121
Figure 7-6. Proposed method to set artificial electrical power output to mitigate the impact of the limited current.	122
Figure 7-7. System response for a short circuit fault in a single machine infinite bus system, with proposed control to enhance the transient stability.	123
Figure 7-8. Oscilloscope measurement for a short circuit fault at bus 9 in the HTB two area system setup to compare the stability with no current limit, with current limit and proposed control, and with current limit and no control.	125
Figure 7-9. Oscilloscope measurement for a short circuit fault at bus 7 in the HTB two area system setup to compare the stability with no current limit, with current limit and proposed control, and with current limit and no control.	125

List of Tables

Table 3-1. Parameters of the experiment platform.	47
Table 3-2. Transmission Line Impedances of the Experimental Platform	47
Table 4-1. Voltage Closed-Loop Controller Parameters	68
Table 4-2. Under-frequency Load Shedding Settings.....	73
Table 5-1. Parameter Setting of the Experimental Platform.....	86
Table 5-2. Controller Parameters for Short Circuit Fault Emulators.....	90
Table 6-1. Truth Table of Adaptive Inertia VSG Control	102
Table 6-2. Base case configuration and CCT	109
Table 6-3. Measured CCT with different control method	111

1 Introduction

1.1 Background and Motivation

Due to the continuously increasing power demand and the requirement of clean energy, renewable energy sources and the related topics have drawn significant attention nowadays [1]. With over 370 GW total capacity installed worldwide by 2014, wind power is one of the largest and most promising renewable energy sources [2]. The U.S. Department of Energy has envisioned that wind power will supply 20% of all U.S. electricity by 2030 [3].

Wind turbines (WT) installed in the electric power system can generally be categorized into four types, as shown in Figure 1-1. Type-1 WT is usually called fixed-speed wind turbine, which is the most basic WT in operation. It employs an induction machine that directly connects to the grid through transformers. The rotor speed of the induction machine synchronizes with the power grid frequency, and keeps almost constant for all different wind speeds. The generated wind power is not optimal, and can only be controlled through the pitch control of the wind blades.

To capture more power from wind, variable speed wind turbines are designed. Type-2 WT is the simplest one, usually called variable slip wind turbine. It employs a set of variable resistors connected to the rotor of the induction machine. This would help to regulate the rotor speed of the WT, and capture the wind power more efficiently. To improve, power electronics converters are used to replace the variable resistor in Type-3 WT. This type of wind turbine is called doubly fed induction generator (DFIG). The flexible control of the power electronics converter enables the induction machine to operate with a wider range of rotating speed than Type-2 WT with less losses. It is thus able to capture more wind power with different wind speeds.

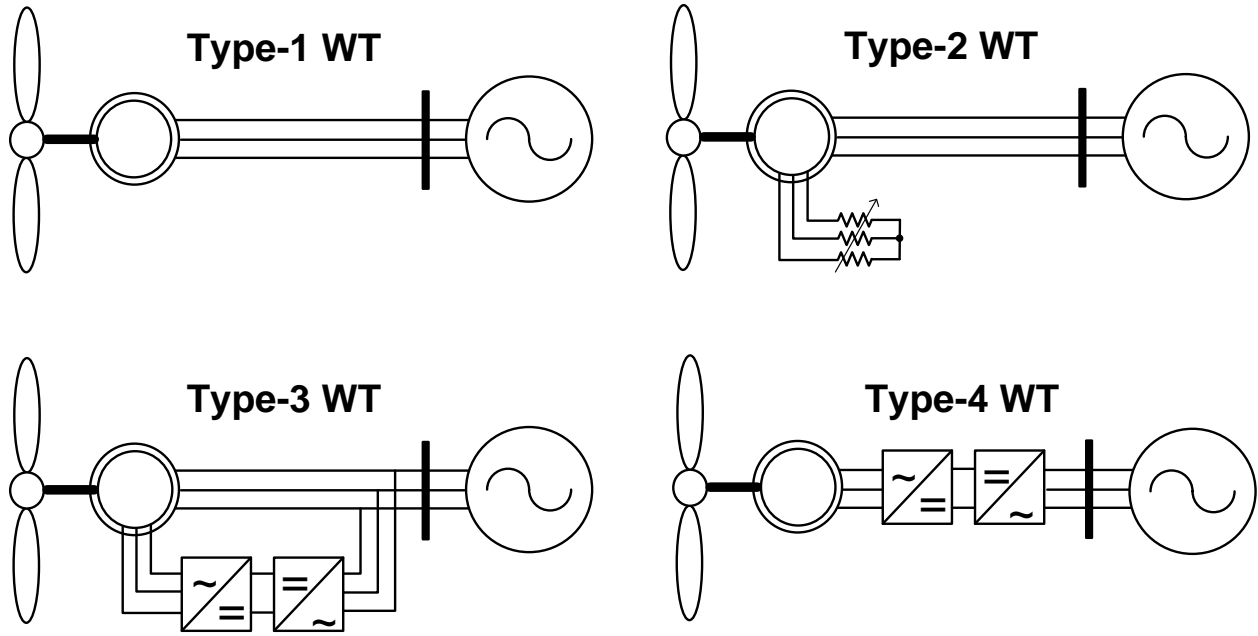


Figure 1-1. Types of wind turbines.

Similarly, full converter wind turbine (FCWT), also known as Type-4 WT, uses ac/dc/ac power electronics converter to connect the induction machine or permanent magnet synchronous machine (PMSM) with the grid. It can also adjust turbine rotational speed to allow for accurate maximum power point tracking (MPPT). Additionally, the ac/dc/ac converter allows it to operate decoupled with the grid conditions, and can achieve better performance during grid disturbance and faults. FCWT is now one of the most commonly installed types of WT. The global market share has been increasing and reached 40.8% in 2013 [4].

Nowadays most WTs are controlled to output the maximum power available and do not react to grid disturbances except for severe faults, and the power fluctuation is balanced by conventional synchronous generators (SGs). However, the case will be different when the penetration becomes

larger with more traditional SGs replaced by WTs. The loss of system controllability and decrease of the system inertia will cause fluctuations in grid voltage and frequency. In addition, the uncertainty and variation of the wind will also pose challenges to the system operators [5].

Thus, grid support control functions from WTs will need to be integrated in the future grid. Various kinds of grid support controls have also been developed for these FCWTs. With appropriate control, the FCWTs will be able to change the active and reactive power injections in addition to the MPPT operation during grid disturbances [5-9]. However, they cannot be regulated and dispatched like the traditional SGs by the system operators.

Researchers then seek to develop controls for the grid interfacing power electronics converters to mimic the behaviors of SGs, and to provide both short term grid support and long term power dispatch functions [10-14]. This Virtual Synchronous Generator (VSG) control allows the renewable energy source to exhibit the same characteristics of the SGs, and can potentially be a promising solution to integrate more WTs in the future grid with high penetration of renewables. But there are still challenges that need to be resolved before the practical applications:

- 1) Most previous academic research rely on simulation due to the complexity of the interconnected electric power system. Experiments are necessary to reveal the interaction and inter-operability of different controls and components, and demonstrate their feasibilities.
- 2) All currently developed VSG technology assumes unlimited energy storage to balance the renewable generation and grid demands, which is not always the case. It is crucial to have the appropriate control strategy for WTs with limited availability of energy storage.

- 3) The system stability impact of integrating VSG controlled renewable energy sources under large disturbances, such as short circuit faults, is not well understood.

The objectives of the proposed research are to develop a testing platform to test and demonstrate wind turbine controls in experiments, to develop a VSG control strategy for FCWT with limited energy storage, and to investigate fault operation of the FCWT with VSG control.

1.2 Dissertation Organization

The organization of the chapters in this dissertation is described as follows.

Chapter 2 provides literature review of the research activities in the proposed research area. It starts with different power system testing methods; and it follows to introduce the converter based power system testing platform in the UTK; then, the existing test emulators for the WTs and short circuit faults are introduced; and finally, the grid support functions and fault operations of FCWTs are presented. Based on the literature review, the research challenges and the detailed objectives of this proposal are given.

Chapter 3 develops a power electronics converter based emulator to represent FCWT in the power system testing platform. It incorporates the existing grid support functions, and it is used for the demonstration of the FCWT operation in a grid with high renewable penetration.

Chapter 4 proposes the VSG control algorithm for FCWT with limited energy storage, considering the energy balance of the FCWT generation and grid demands. It allows the FCWT to behave like a SG in the power system, and operate stand-alone without the main grid.

Chapter 5 develops a power electronics converter based short-circuit fault emulator to perform

four basic types of short-circuit faults in the testing platform. The test results of utilizing it to estimate a critical clearing time is also presented.

Chapter 6 proposed to utilize the flexibility of VSG controlled generation unit to improve the power system transient stability after a short circuit fault in the system, and tested the results using the emulator and platform developed in Chapter 3 and Chapter 5

Chapter 7 analyzes the impact to the power system transient stability from the VSG with limited output current, and proposes control methods to improve the stability.

Chapter 8 summarizes the advances made in this dissertation so far and gives recommendations for potential future work.

2 Literature Review and Challenges

This chapter reviews the research activities in the previous proposed research area of power system testing methods and components, and grid support functions of the WTs. The research challenges are then identified based on the review, and the detailed objectives of the proposed dissertation are presented.

2.1 Power System Testing Methods

This section briefly summarizes different kinds of power system testing methods, and compares the advantages and disadvantages among them, in order to justify the power electronics converter based power system emulation testing platform introduced in the next section.

2.1.1 Digital Simulation

Offline digital simulation has been used widely to predict the behavior of an electrical system in time domain due to its low cost, easy accessibility, and flexible configuration. However, due to the limitations of the computational resources and run time, the simulation accuracy and fidelity suffer from different levels of model reductions. Often the results depend on the solver and time steps selected, and have numerical stability and convergence issues [15].

In recent years, the revolution of integrated circuits such as microprocessors or FPGAs has enabled real-time digital simulations, such as RTDS [16] or Opal-RT [17]. With deliberately designed network solutions and parallel computing techniques, these tools can simulate a large system in real-time with fixed time-step. They can incorporate with digital and analog inputs and outputs to connect with the physical world to form a Hardware in the Loop (HIL) simulation. It

allows the real-time testing of the developed system controllers without having to develop a real hardware test platform [18]. Since they are still using mathematical models, the numerical stability of digital simulation can still sometimes be an issue.

These non-real-time or real-time digital simulation tools offer a large diversity of pre-defined models, and have the capability to integrate custom built models. Nevertheless, many critical conditions in the simulations tend to be simplified or ignored by the users, such as measurement error, control and communication time delay, device physical bounds and saturation, electromagnetic interference, etc. Accounting for the uncertainties in the simulations is computationally challenging, but failing to address these issues could cause unrealistic or incorrect results [19].

2.1.2 Hardware Based Testing

On the other hand, hardware-based system testing can reveal the impact of the neglected aspects of digital simulation. It is an essential step before the deployment of any proposed controllers or developed devices. To assist with such a testing need, a real-time digital simulator can be paired with a power amplifier to form a Power HIL (PHIL) test platform. The PHIL platform can be connected to an equipment under test (EUT), and evaluate its behavior with the remainder of the system represented by the simulator [20]. While it has great fidelity to test the equipment, the overall system simulation accuracy is not better than digital simulation.

To study the *system* behavior, researchers have also built down-scaled electrical power system or transient network analyzer (TNA) to produce a hardware-based power testbed as early as the 1920s [21, 22]. The capability of such a system has been enhanced to incorporate new technologies

in recent years. Examples include National Renewable Energy Laboratory's (NREL) Energy Systems Integration Facility (ESIF) [23] and the Consortium for Electric Reliability Technology Solutions' (CERTS) microgrid testing platform [24].

While these down-scaled hardware-based testing platforms provide superior fidelity, they are generally bulky and costly. Their topology and configurations are difficult to change, usually requiring physical rewiring and component replacements for the testing in a different system configuration or parameters. Another challenging issue is rescaling. To precisely represent a power component with different power and voltage, the emulator should have the same per unit value of the original one. It is relatively easy for the passive components like resistor, inductors, and capacitors, but difficult for rotating machines with different impedances, inertia and saturation levels [25, 26]. Transmission lines also pose challenges since many cascaded circuits made up with inductors and capacitors are required to represent the distributed parameters.

2.2 Hardware Testbed at CURENT Center in University of Tennessee, Knoxville [27]

Taking advantage of the fast, accurate, and flexible closed-loop control of power electronics converters, it is feasible to program them to mimic the static and dynamic behaviors of electrical power components [28]. There have been industrial products developed that use power electronics based emulator for the testing of electrical vehicles, aircraft, motor drives, grid integration of energy storage, PV, etc. [29-31]. This provides a flexible and easy way to test and analyze the characteristics of the emulated objects.

Based on this idea, a Hardware Testbed (HTB) has been established at CURENT at the University of Tennessee by connecting multiple modular converter emulators together [32]. It is

utilized to emulate large scale power system transmission network using interconnected reconfigurable modular converters. Each converter represents a single or a aggregated element of power sources or loads. This allows system testing and demonstration in the desired environment without requiring full scale transmission, generation, and load equipment.

2.2.1 Emulation Principle and Structure

Each individual converter in the HTB serves as an emulating unit. It has the same steady-state and dynamic response as the emulated object with respect to its terminal voltage and current. The local voltage or current information is measured as the input of the object model, and the output current or voltage reference is calculated for the controller to track, ensuring the converter emulator behaves the same as the emulated object. The block diagram is shown in Figure 2-1.

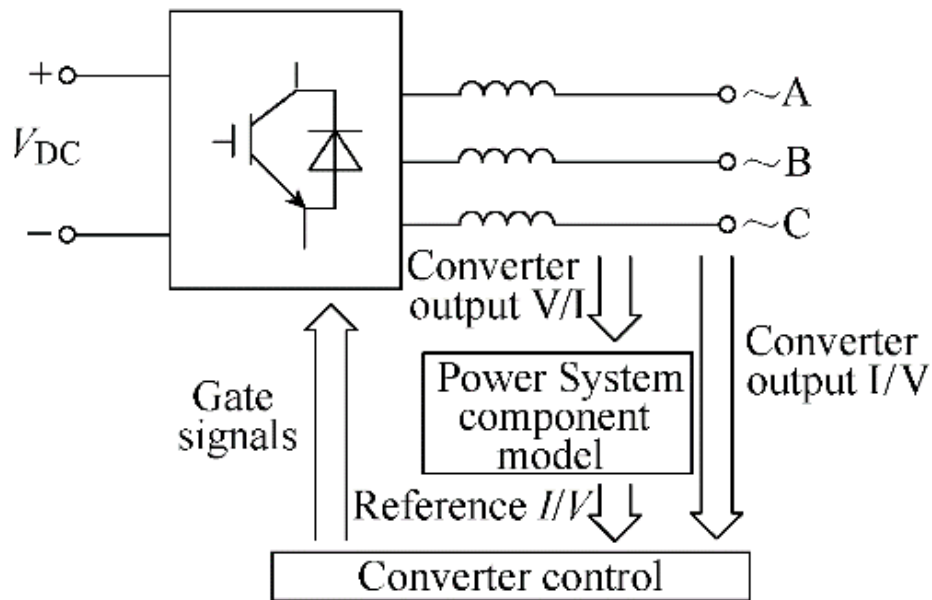


Figure 2-1. Emulator operating principles [27].

The components in an electrical system could be considered as either voltage source or current source. Analogously, the converter emulators have two kinds of control schemes, one type regulates the terminal voltage, and the other controls the output current. For example, the load emulating converter often employs a current type of control, i.e., measures the emulated grid voltage, and generates the desired emulation current; and the generator emulating converter more naturally uses a voltage type of control.

Many types of emulators have been developed in the HTB. Available emulators include SG [33-35], static and dynamic loads [36-38], PV [39], flywheel [40] and batteries [41, 42]. In addition to single converter emulators, a transmission line can be emulated by a set of back-to-back converters [43-46]. Short circuit faults within the emulated transmission line can also be modeled and represented by the converter emulator sets [44]. The emulators for HVDC transmission lines and multi-terminal HVDC (MT-HVDC) grid emulators with corresponding faults and protection have also been developed [47].

The HTB has a paralleling converter structure as shown in Figure 2-2. Converter emulators share the same DC link, which is supported by an active rectifier, with its voltage regulated to a constant level. The AC terminals of the converters are connected together by filter inductors. Thus, the AC link of the converters can be considered as the emulated power system. Active power generated by the generator emulators is absorbed by the load emulators, reducing the total power consumption of the system. The undesired zero sequence and switching period circulating currents introduced by this paralleling topology are controlled and reduced [48], so that the emulating current flowing between the converters would represent the actual power flow. Between the

converter emulators, inductors are used to emulate local connecting lines.

Because of the power circulating structure and large DC capacitance of the paralleled converters, the DC link voltage of the HTB remains relatively stable during system transients. The closed loop control of the individual emulators allows decoupling of the DC link voltage and emulated AC network behaviors.

Currently, three different power system topologies have been designed and tested using the HTB platform, as shown in Figure 2-3. The first one is developed based on Kundur's two-area system [49], which has 2 generators and 1 load in each area, and a long transmission line between the areas, as shown in Figure 2-3(a). Later, the capability of the system was enhanced by adding a third area representing a load center, a down-scaled MT-HVDC network, and two wind farm emulators. The topology of the three-area system is shown in Figure 2-3(b). The third system configuration was derived from a reduced model from Western Electricity Coordinating Council (WECC) interconnection, with the MT-HVDC network as an overlay. It is referred to as the four-area system. Figure 2-3(c) shows an example with 80% of renewable penetration by replacing some traditional synchronous generators with renewable energy sources.

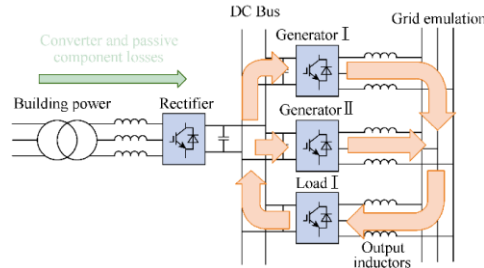
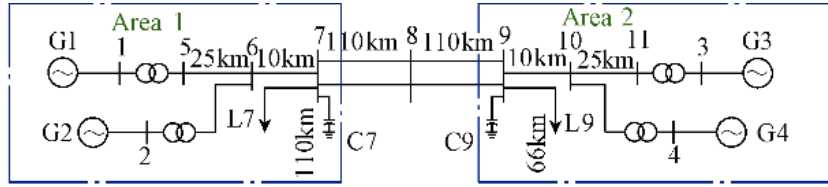
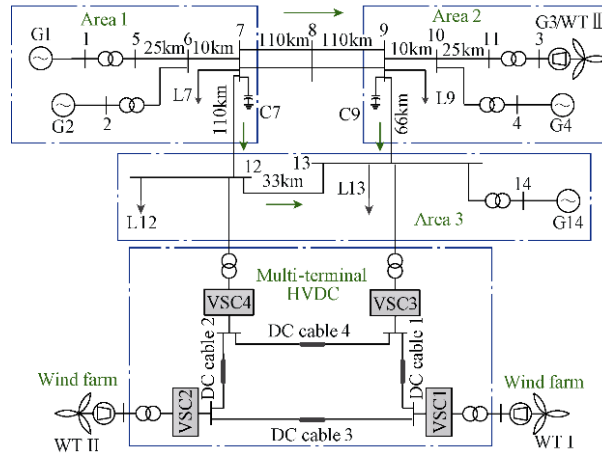


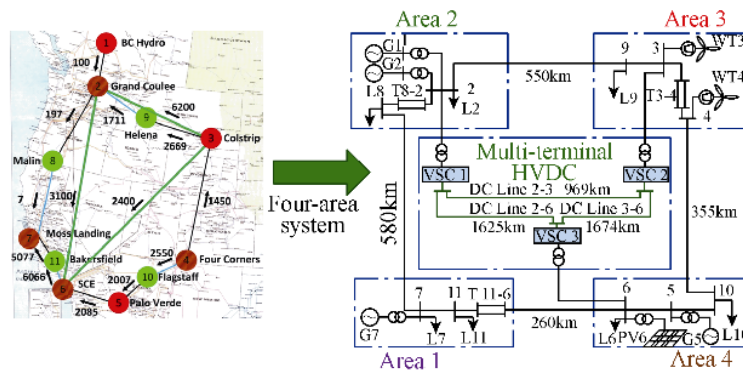
Figure 2-2. Structure of the HTB [27].



(a) Two-area system



(b) Three-area system



(c) Four-area system

Figure 2-3. Power system emulation topology configurations in HTB [27].

Figure 2-4 shows the reconfiguration scheme of the HTB to allow rapid transition between different system configurations. Each emulator in Type I Cabinets can be reconfigured to represent different components of power systems by loading the corresponding programs. The parameters of the components, such as generator inertia, load composition, battery capacity, can also be easily set. Long distance transmission line and HVDC lines are installed in Type III cabinets. The emulated impedance can be set through system control.

To change the system topology in an arbitrary way, a switchable inductor cabinet (Type II Cabinet) that consists of contactors and inductors of different values has been developed, as shown in Figure 2-5. By opening or closing the contactors that are in parallel connection with the inductors, the impedance of the emulated line can be adjusted to the desired value. Type II Cabinet connects with Type I and Type III cabinets using isolation contactors. This way, the system topology can then be easily reconfigured by changing the wire connections on the front panel.

Figure 2-6 shows a photograph of the HTB Type I and Type III cabinets. Each converter emulator is repurposed from a 600 V, 75 kW DC-fed motor drive manufactured by VACON (acquired by Danfoss), with DSP28335 as the controller. Each Type I cabinet has four single unit emulators, and each Type III cabinet has 3 back-to-back transmission line emulators. Real measurements are integrated into the system, including potential transformers (PT), current transformers (CT), phasor measurement units (PMU) and frequency disturbance recorder (FDR).

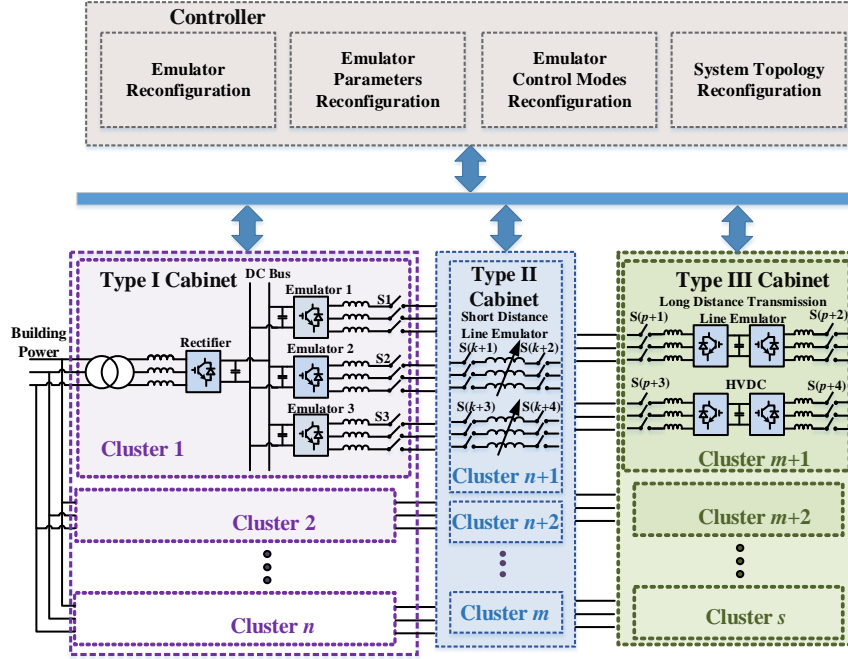


Figure 2-4. Reconfiguration scheme of the HTB and emulator cabinet configuration [27].



Figure 2-5. Photo of HTB Type II reconfiguration cabinet [27].



Figure 2-6. Photo of HTB Type I and Type III reconfiguration cabinet [27].

The HTB has also been combined with RTDS to further enhance the testing platform capability. Connected to RTDS through a power amplifier, the HTB can emulate one part of the electrical system, and RTDS is used to simulate the rest of the system [50]. Actual power equipment with HTB ratings can also be connected to the HTB as an EUT for PHIL testing.

2.2.2 Communication and Control Architecture

The converter emulators can be controlled and monitored remotely through communication links established by National Instruments' CompactRIOs (cRIO) using CAN bus. In addition, cRIOs can gather the data from PTs, CTs from analog input; and send data to computer for monitoring, closed-loop control, and visualization. PMUs and FDRs can directly communicate to the computer using OpenPDC software. The overall communication structure is shown in Figure 2-7.

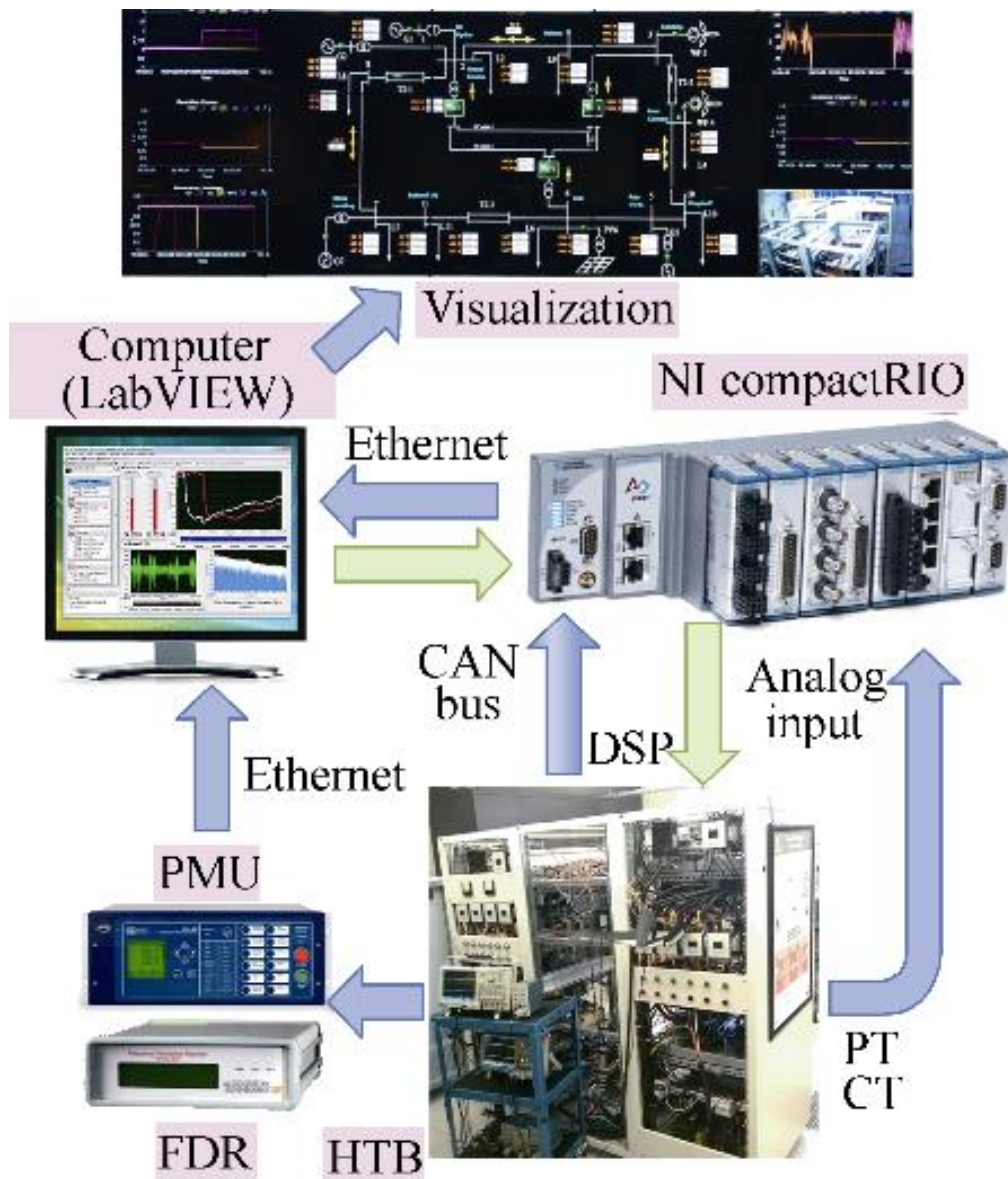


Figure 2-7. Communication structure of HTB [27].

Figure 2-8 shows the control architecture, which can be divided into three layers. The system controls reside in the computer – they oversee the operations of different power system areas, provide functions like system level protection, data logging, visualization and human machine interface (HMI). Profile setpoints and start/stop commands can be determined by the operators and sent to the lower layers for the specific controls.

The area control level manages the components within the area, and do not have full information of the other areas. The control functions include state estimation and other monitoring and closed-loop controls such as automatic generation control (AGC), wide area damping control, voltage stability assessment, and renewable energy sources operating mode selection.

The bottom layer is the component controls, which are integrated in the DSP of the converter emulators in addition to the physical model. Each type of emulator has its own set of component controls. For example, the renewable energy source can be controlled to track the maximum power point, provide frequency and voltage support to the grid disturbance, ride through and protect itself during emulated grid faults, etc. The control functions implemented are shown in Figure 2-8.

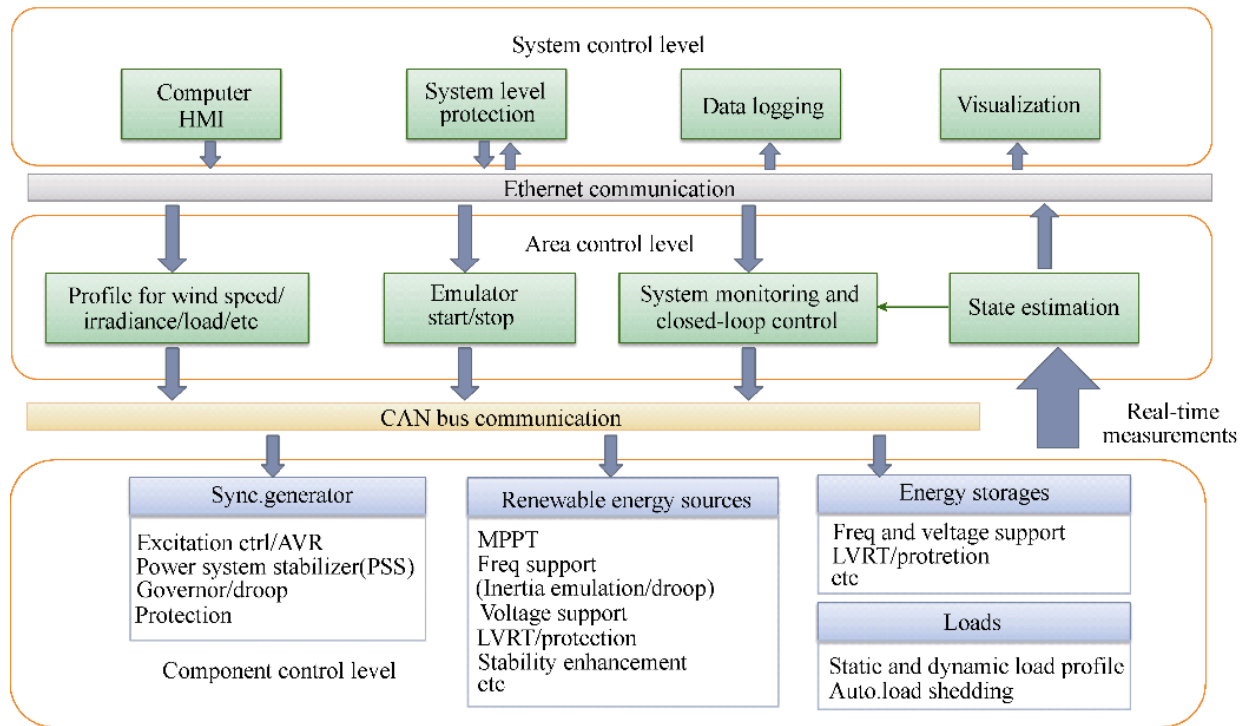


Figure 2-8. Control architecture of HTB [27].

2.2.3 System Emulation Demonstration

This reconfigurable converter-based testing platform offers a platform for development, testing and demonstration of various power system researches. This section presents several examples to illustrate the system emulation and testing capabilities of the HTB.

Inter-area oscillation often results from a poorly damped power system with weak transmission lines, and limits the power transfer capabilities. In the HTB two-area system, a measurement based wide area oscillation damping strategy has been tested and verified. As shown in Figure 2-9, the frequency difference between G1 and G3 has a low damping ratio to a load step

change event at L7. A proposed adaptive WADC control strategy can successfully suppress the oscillation, while the conventional one that does not consider the communication delay could trigger another oscillation mode in the testing system [51-54].

Online voltage stability assessment helps the operators foresee potential voltage instability and takes control action promptly to mitigate the situation. Power transfer limits of the transmission lines are calculated in real-time using the measured voltage and frequency data. Figure 2-10 shows the algorithms in action in the three-area system, where the loads at bus 12 and bus 13 are ramping up. The transferred power on the tie-lines 7-12 and 9-13 increases and gradually reaches the calculated limits by the algorithm. When the margin is low enough, the reactive power support will be enabled from the HVDC station, and voltage collapse is avoided [55].

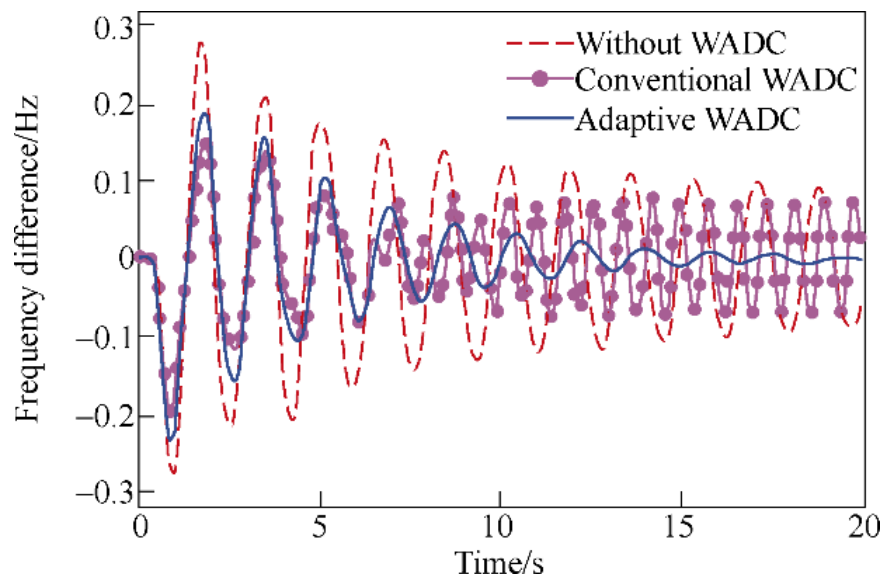


Figure 2-9. Test results of wide area damping control for two area system [27].

Power system separation scheme divides a system into multiple islands to prevent system instability following a large disturbance. Remedial action scheme (RAS) is built into the HTB four-area system controller. When there is a three-phase short-circuit event at the transmission line 3-4, it will be tripped due to overcurrent. RAS action saves the system by also tripping the line 2-8, so that the system is separated into two stable islands as shown in Figure 2-11.

The fast closed-loop controls of the inverter may interact with one another and create small-signal stability problem, even if the inverters are all designed stable individually. This problem can introduce a higher order harmonic or subsynchronous resonance. Figure 2-12 shows an example of output currents exhibiting a 600Hz harmonic resonance when connected to the rest of the system. After tuning the control parameters using the impedance based stability criterion, the voltages and currents can return to stable operation [56-58].

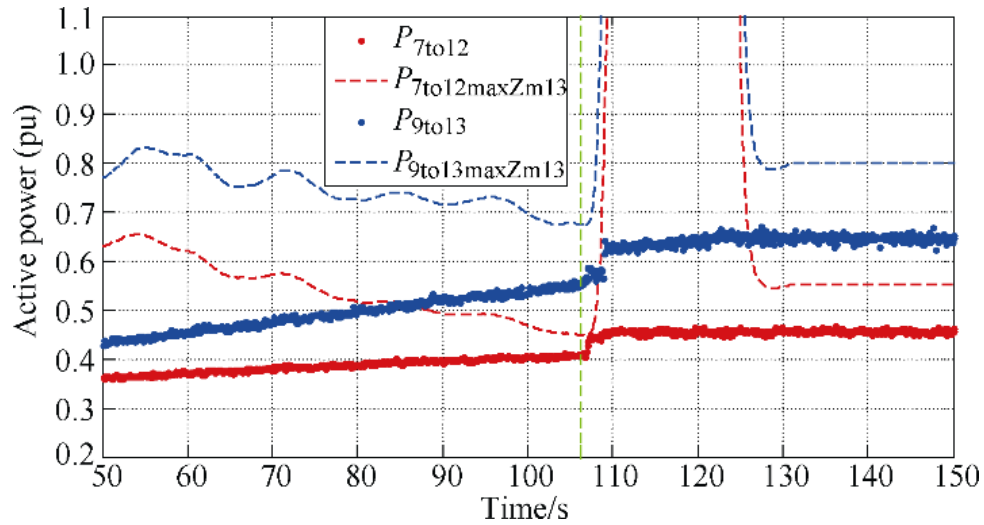


Figure 2-10. Test results of real-time voltage stability assessment and control in three area system [27].

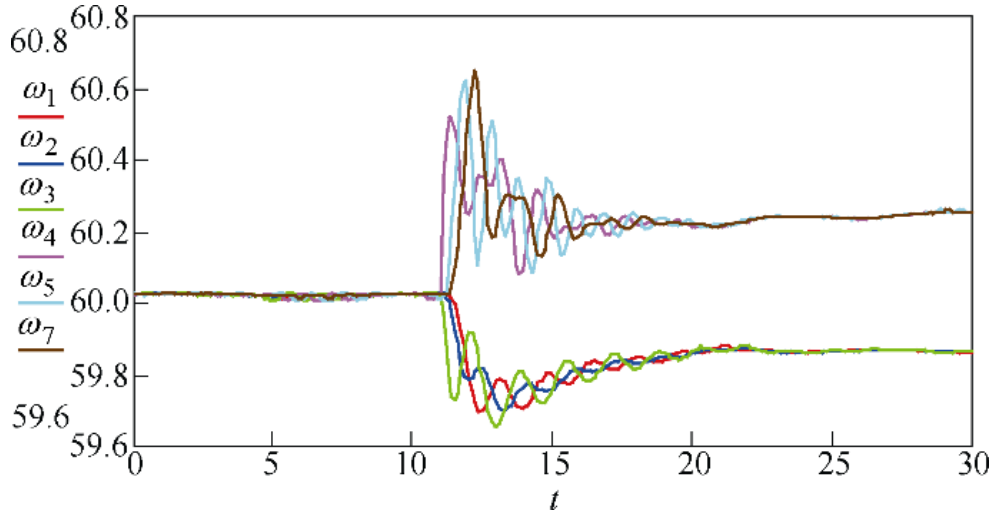
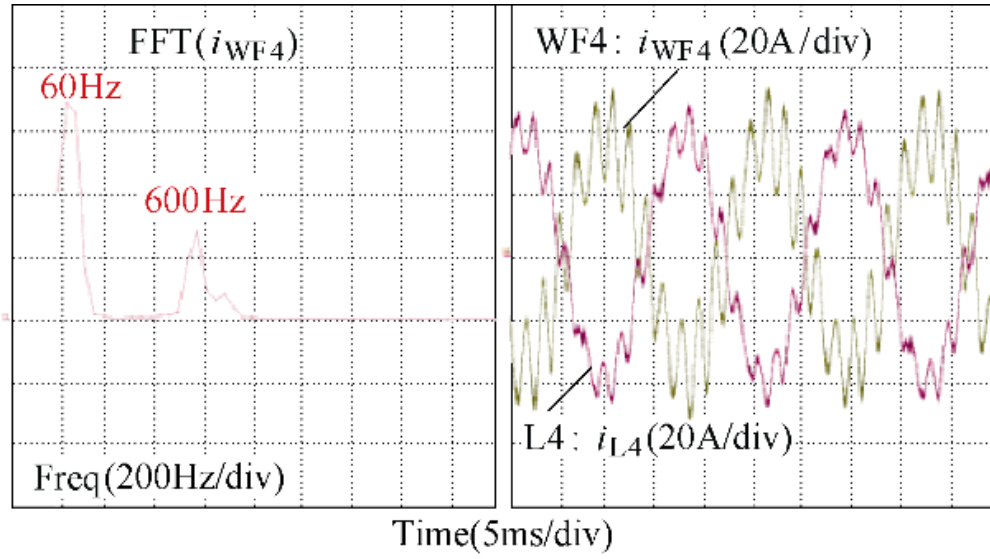


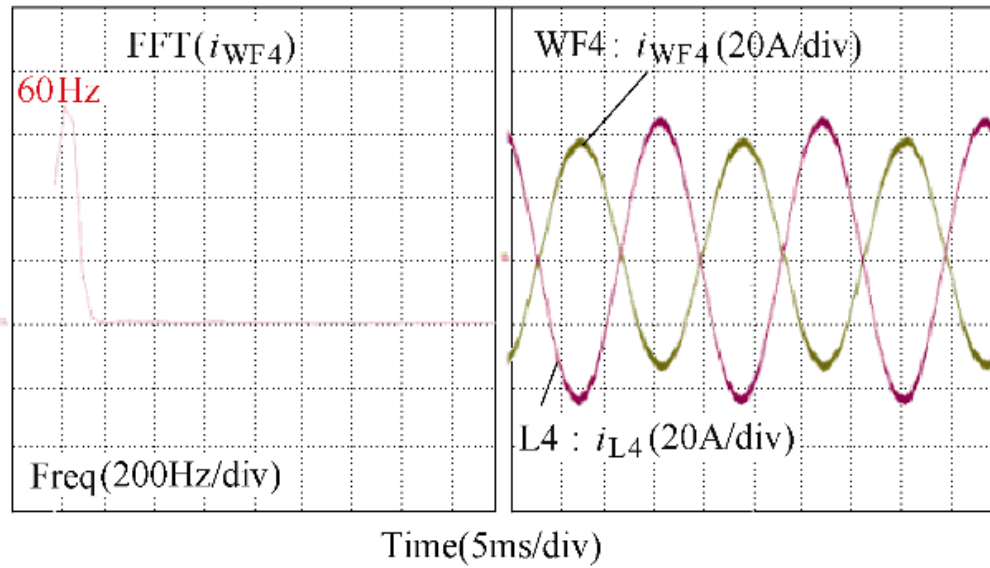
Figure 2-11. Test results of remedial action scheme of controlled separation for four area system [27].

2.2.4 Comparison of Existing Power System Testing Methods and Identified Needs

Compared with traditional hardware-based testing platform with actual down-scaled components, the HTB allows more precise and flexible scaling and modeling of many electrical components, such as rotating machines [35]. The emulators can be easily reprogrammed both in terms of model types and parameters to enable flexible reconfiguration and representation of different components. The power circulation scheme between sources and loads significantly reduces the need for laboratory power capacity and saves energy.



(a) Unstable case with parameters designed for ideal grid



(b) Stable case with properly designed parameters

Figure 2-12. Test results of harmonic stability problem [27].

On the other hand, HTB is fundamentally different from real-time digital simulation. It is essentially an analog emulator with real power flows between real hardware emulating power system components. The HTB incorporates more realistic power hardware, especially in the case of power electronics based hardware such as converter interfaced renewable energy sources. It is also easy for the HTB to integrate real communication, measurement, control and protection equipment. Even though the emulators still largely rely on numerical models, similar to the case of real-time digital simulators, these models are truly distributed, and computation is truly paralleled. As a result, HTB has shown to have much less numerical convergence problems. The limitation on the emulated number of buses is purely due to the space and resource issues. HTB also handles multi-physics models better covering shorter time-scale switching events to longer-term power system events.

Nevertheless, the HTB also has disadvantages compared with hardware based test platforms: the emulators are not perfect; the imperfections of the converter, measurements and closed loop control will introduce error; it is digital simulation inside of each converter emulator, and as such there could still be numerical issues; and emulator controls might have harmonic interactions that do not belong to the system behavior if not designed properly.

The HTB testing environment allows different types of power system testing with various emulators to represent the actual components in the electric power system. Two essential emulators among them are WT emulator and short circuit fault emulator to enable even more testing capabilities of the HTB, especially the case to represent the future grid with high penetration of renewables

The next two sections will introduce the existing methods to emulate the FCWT and faults in a hardware based power system testing platform.

2.3 Wind Turbine Emulation Methods

For digital simulation, there have been many works discussing the model of FCWT. WECC generic models use the single-line model, and are focused on the disturbances and consequences of the power system [59]. DIgSILENT gives detailed physical and control models which satisfy the need of RMS and EMT (Electromagnetic Transient) simulation [60]. Reference [61] developed a detailed simulation model considering the flicker effect caused by wind shear and tower shadow.

Based on the established model, physical emulators have been built in the hardware base testing platform for real-time HIL studies. These WT emulators can be categorized into 2 types – rotating machine type and real-time model type, as shown in Figure 2-13.

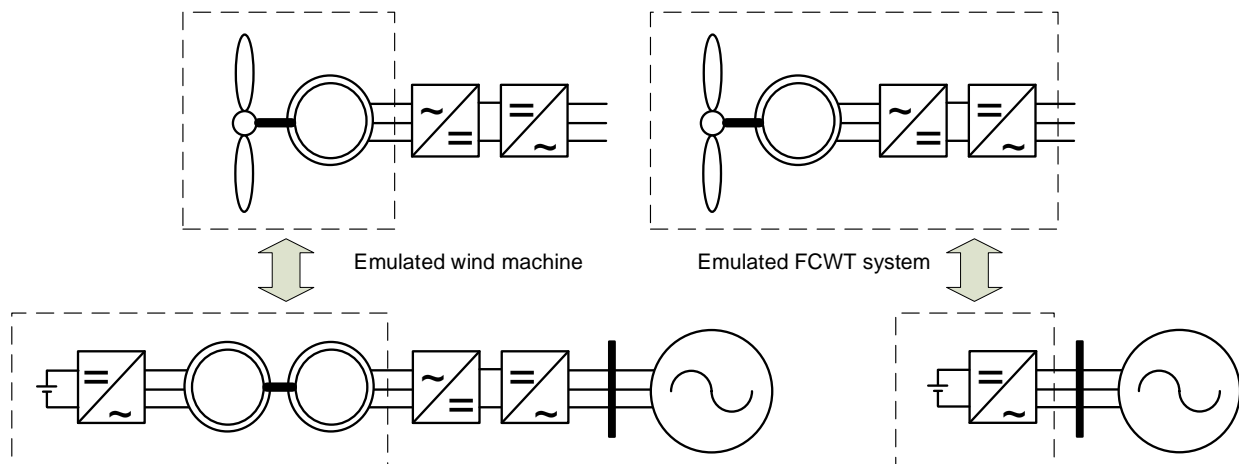


Figure 2-13. Two types of wind turbine emulator configurations.

Rotating machine type usually requires a torque controlled motor to represent the wind torque and turbine inertia, and another motor to serve as the wind turbine generator [26, 62-64]. These emulators are mainly used for testing the control algorithms to manage the torque and rotating speed of the WT, rather than its impact to the grid.

While most of the WT emulators are rotating machine type, a few other research works used a different approach as real-time model type [65-67]. For these emulators, the FCWT conversion system is modeled in software instead of represented by physical machines. The model can generate output current reference according to the terminal voltage of the emulator. A power electronics converter can be served as an amplifier, which connected with the rest of the emulated grid. Currently, these works are only at proof-of-concept stage, and are only used for testing their own control algorithm. The developed emulators are not placed in a larger system of multiple components to study the system impact; and the emulators do not include other possible control algorithm for comparison.

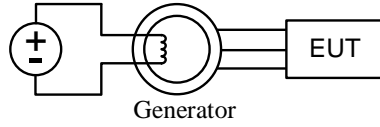
For HTB, the rotating machine type WT emulator cannot be applied, since the emulator can only be configured to represent the wind turbine. The flexibility of changing the emulated components with different controls cannot be achieved. Thus, in order to demonstrate the impact of a future grid with high wind penetration in the HTB system, an amplifier type WT emulator with different control algorithm needs to be developed.

2.4 Fault Emulation Methods

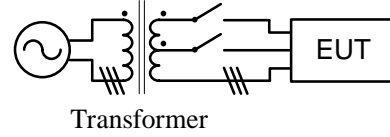
To study the dynamic response of a power system disturbance caused by a short circuit fault, computer based simulation tools can be utilized. But the results are often subjected to numerical

stability issues, especially with power electronics penetrated power systems [68, 69]. In contrast, field tests with real hardware can provide reliable testing results under short circuit fault, but it is often costly and non-repeatable. Thus, real-time hardware based laboratory test systems have been widely used to test the performance of the equipment or system under fault in a fully controlled environment. Testing platforms have been proposed and implemented to verify the fault ride-through (FRT) compliance of grid-connected equipment [70-72], to test the power system protection controls and devices [73], and also to analyze the system performance under disturbances [32, 74, 75].

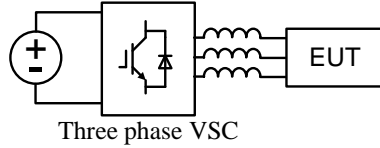
Figure 2-14 shows the schematics of the fault emulators to create voltage sags previously proposed in the literature. In [76], the authors control the excitation system of a synchronous generator to create symmetrical sags in the terminal voltage of the equipment under test (EUT), as shown in Figure 2-14(a). The voltage sags can also be generated by a transformer with a combination of switches, such as the topology given in Figure 2-14(b) [77]. Configurations like Figure 2-14(c) only require a controllable three phase voltage source converter (VSC) directly connected to the EUT to emulate the grid fault. By controlling the output voltage of the VSC, it can generate various types of grid faults, such as sags, swells, harmonics, unbalances, and phase shifts [70-72, 78]. These methods are suitable to test the fault performance of a single component like a wind turbine in a stand-alone environment. But since they are incapable of creating any actual fault current, impacts such as CCT of a short circuit fault for a system that consists of multiple components cannot be studied.



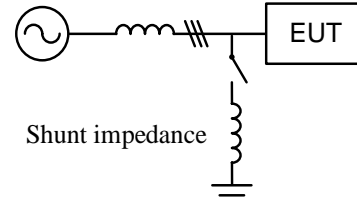
(a) Rotating generator to create voltage sags



(b) Transformer to create voltage sags



(c) Series connected VSC to create abnormal
voltages



(d) Shunt impedance to emulate short circuit
faults

Figure 2-14. Schematics of the fault emulators [79].

The shunt impedance method in Figure 2-14(d) was adopted in [80, 81]. The fault current flows through the shunt impedance, and creates a low voltage at the terminal. This allows the generation of one to three phase voltage sags with different depth values, by modifying the switches and grounding impedance. By providing the fault current, a system with multiple components can be put under investigation. But the drawback of this method is that it requires bulky equipment and is not flexible to create different scenarios.

In order to fully investigate the fault impact on a power system with actual transient fault current, and at the same time maintain testing flexibility, a short circuit fault emulator needs to be developed for HTB.

2.5 Grid Support Functions from Full Converter Wind Turbines

This section briefly summarizes basic operation of the FCWT, and its corresponding grid support controls. The existing works around VSG control are introduced, and the gaps of applying the VSG control to the FCWT are explained. In addition, the fault operation of the FCWT is also presented in this section.

2.5.1 Basic Operation and Grid Support Functions of FCWT

Similar to most of the other power electronics interfaced renewable energy sources, FCWTs utilize a phase locked loop (PLL) to synchronize with the main grid, and inject maximum available power to the grid by current closed-loop control.

To maximize the harvested wind energy, different MPPT control algorithms are proposed [82]. The turbine speed is controlled to maintain the optimal tip-speed ratio (TSR), with known or unknown information about wind speed variations.

As pointed out in the introduction section, it is observed that as the power electronics interfaced renewable penetration gets higher, dynamic frequency response of the power system becomes worse. During a power system disturbance, the frequency excursion could become larger, and eventually damages or triggers the protection of the equipment [83].

To avoid this, active power support functions are proposed to enhance the existing MPPT functions. The general idea is to mimic the behavior of the traditional SGs – to inject more active power when frequency is lower than the nominal value, and vice versa.

For traditional SGs, when a grid frequency drop disturbance first occurs, the rotating speed of

the generator would also decrease to synchronize with the rest of the grid. Thus, kinetic energy from the generator rotor would be released in the short period. So, the short-term frequency response of the WT is usually called inertia emulation or synthetic inertia [6, 84, 85]. Extensive studies from academia and industry have proven the effectiveness of this control [86-88].

For longer-term, generators have governor controls to limit the power generated from their prime movers if frequency is high, and hence reduce the rotor speed and reach equilibrium with the rest of the system. The mechanism is called droop control, as the actual rotor speed is allowed to “droop” or decrease to the reference value [89]. This concept was also migrated to the inverter controls for parallel operations [90]. WT also adopt such strategy for frequency regulation, where its pitch or rotor speed of the WT can be controlled to reduce the captured wind energy [6, 91, 92]. On the other hand, during a frequency drop event, WT cannot provide additional power if already at the maximum power point. Thus, de-loading or curtailment control of the WT is developed to allow it only to generate a percentage of the maximum available power, and have head-room to increase the generation for droop control [93].

On the other hand, reactive power output from WT may also introduce problems. Over-voltage or under-voltage may occur if the reactive power output from the WT is not regulated. The system may even collapse due to voltage stability issues. For this reason, various reactive power control from WT are proposed, including constant power factor control, terminal voltage control, virtual impedance control [94], etc. Analysis has also been conducted extensively for the effectiveness of the proposed controls [95-98].

Standards and grid codes are developed to require WT to have grid support functions

available for the system installation and operation [99].

2.5.2 Virtual Synchronous Generator Control

Despite different grid support control algorithms have been proposed, new problems still arise as the penetration level gets higher, especially the case when the grid is weak [100-102], i.e. the grid impedance is high or short-circuit ratio (SCR) of the system is small. One of the reasons is because the current closed-loop control and PLL synchronization of the power electronics converters are intrinsically different than the traditional SGs. Thus, the VSG control is proposed for the converters to fully emulate the SGs to avoid the problems.

Rather than the PLL, the VSG control utilizes the swing equation to synchronize with the grid [103]. Thus, the built-in droop and inertia characteristics of the VSG control can provide better active power - frequency response for grid connected converters [104]. The inertia constant and the damping ratio of the emulated SG can be adjusted to accommodate system conditions [105]. Reactive power control and load sharing are achieved [106]. The small signal model and stability of the VSG control are also studied in the literature [107-109], results have shown that it has superior performance in weak grid conditions [110].

However, previous works on the virtual synchronous generator (VSG) controls are mostly focused on the grid interfacing controls. Energy storage is assumed to be large enough to support all the power balance of the renewable generation system, which is not always the case. In [111], the authors presented the VSG control for the FCWT. While it can represent some of the SG dynamics including the inertia response, it can only operate around the maximum power point. This means the output power of the FCWT cannot be regulated and dispatched, and it is not suitable

for stand-alone operation without other sources to balance the power difference between the wind generation and load consumption.

On the other hand, there are studies to control the FCWT at non-optimal power point to provide head-room for active power support, and load tracking [112, 113]. But the coordination of wind turbine control and grid side VSG control is not well-established.

Combining the WTs with short term energy storage has been studied in academic fields and implemented in industry products [114-116]. With minute-level energy capacity, the storage helps to compensate the power fluctuation of the wind generation and provide dynamic grid support. The balancing and coordination control of the energy storage for VSG controlled WTs is not reported in the literature.

Therefore, it still remains a challenge to maintain the power balance and the control coordination between the renewable generation and grid integration, with limited capacity of the energy storage.

2.5.3 Operation of FCWT under Large Disturbance

Previously in the early 2000s, renewable energy sources were required to trip or disconnect to the main grid, if its terminal voltage deviations from the nominal value [117]. As the penetration gets higher, the tripped generation may lead to cascaded failure, which may cause blackout of a major part of the power system [118, 119]. The delayed recovery of the renewable sources may also exacerbate the cold load pick-up issue, when the system is back on-line [120].

Thus, low voltage ride through (LVRT) or fault ride through (FRT) function is demanded for

the distributed renewable energy sources in the new standards and grid codes [121]. It is required that the distributed renewable energy sources have the capability to stay connected to the main grid when a transient fault occurs, and it is required to continue operation after the fault clears. Some European countries even have grid codes to demand them to inject active or reactive current during the fault to support the under-voltage locally [99, 122].

A large disturbance may also trigger the problem of system rotor angle stability, which is also known as transient stability. It describes the ability of a system to remain in synchronism when subjected to a large disturbance [49]. The triggering event includes short circuit fault, large loads switching on/off, or large generator tripping. These events lead to large excursion of generator rotor angles. Once the angle difference between two generators in the system is large enough to pass the unstable equilibrium point, the system enters the unstable region, and cannot recover to the original operating condition.

To improve system stability, VSG controlled FCWT provides much more flexibility to the output characteristics than the traditional SGs. Under a disturbance, the VSG controlled FCWT does not have to have the same exact response as SG. It is possible to alter the generator inertia under grid disturbance [123-127]. So that the frequency and voltage response after a short circuit fault may be completely different than the traditional generator. However, these previous studies mainly focus on small signal stability, or large signal stability where only unrealistic infinite bus system was considered. It is still a challenge to use this concept to enhance the large signal transient stability where multiple generations are present.

On the other hand, power electronics devices are not designed to withstand as large fault

current as the traditional SGs. The output fault currents from the converter need to be bounded to prevent any damage to itself. This is relatively easy for current closed-loop controlled converters that operate to inject active and reactive power to the grid [128]. For voltage closed-loop controlled converters, since the output current is usually determined by the outside circuit or loads, control algorithms are also proposed to limit the output current during fault [129-131].

There has been some recent research work started to analyze the VSG's impact to power system transient stability [132-135], especially when the faults are not severe enough to trigger current limiting function [132-134]. But there has not been a comprehensive study to demonstrate the impact and potential improvement to the system transient stability using VSG controlled energy sources.

2.6 Research Objectives

According to the literature review above, many issues are still unsolved to the proposed research area. The main challenges include:

- (1) Lack of a WT emulator in CURENT's HTB power system emulation platform, with different grid support functions to study system impacts, and demonstrate system operation with high renewable penetration.
- (2) VSG control of a FCWT to maintain the power balance and the control coordination between the renewable generation and grid integration, with limited capacity of the energy storage.
- (3) Lack of a short circuit fault emulator in the HTB platform to study the power system

behavior under fault.

- (4) The operation of a VSG under and after a grid fault to provide grid support are not well understood, especially for power system transient stability analysis.

Corresponding to the challenges listed above, the main tasks of this dissertation are identified as follows.

- (1) Develop a FCWT emulator in the HTB system with all available grid support control algorithms implemented to test the system performance with high renewable penetration.
- (2) Propose a comprehensive VSG control strategy of FCWT with the consideration of limited energy storage, to allow it to exhibit SG dynamic behavior to support the grid, and also allow it to work under both grid-connected and stand-alone condition.
- (3) Develop a short circuit fault emulator in HTB system to test the system performance under various types of faults for any fault duration.
- (4) Propose control strategies for VSG to enhance the transient stability of the power system.

3 Emulating Full-Converter Wind Turbine in HTB Testing Environment

This chapter presents a FCWT emulator using a single converter to be implemented in the HTB system [136]. As explained in Section 2.3, an amplifier type of the emulator is used for this application. The developed FCWT emulator is used for testing the proposed and existing FCWT control algorithms.

3.1 Developed Full-Converter Wind Turbine Model

3.1.1 Overview

As stated in Section 2.2.1, the implemented power system component model of an converter emulator determines its output characteristics. Figure 3-1 shows the block diagram of the model of the developed FCWT emulator. The model consists of both physical parts and control strategies of the FCWT, including the wind model, permanent magnet synchronous generator (PMSG) model, converter model, and their controls. Each part of it can be designed and implemented independently. This flexibility enables the evaluations of different converter topology, generator structure or control methods. The detailed models also help to set physical constraints like DC-link voltage, converter output duty-ratios, and thus make the emulation more realistic. Detailed explanations of the physical models, corresponding control strategies, and calculation of the emulation current reference are presented in the following parts.

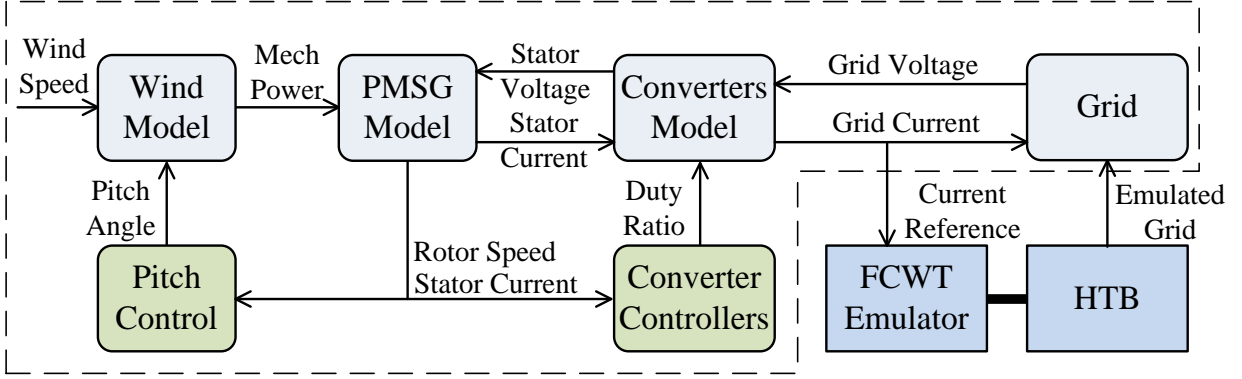


Figure 3-1. Block diagram of the model of the wind turbine emulator [136].

3.1.2 Wind Model

The wind power input can be characterized by:

$$P_w = \frac{1}{2} \rho A_r c_p(\lambda, \beta) v_w^3 \quad (3-1)$$

where P_w is the power extracted from the wind; ρ is the air density; c_p is the performance coefficient or power coefficient; λ is the tip speed ratio – the ratio between blade tip speed v_t and wind speed v_w ; β is the pitch angle of rotor blades; and A_r is the area covered by the rotor.

Numerical approximations have been developed to calculate the coefficient:

$$c_p = 0.73 \left(\frac{151}{\lambda_i} - 0.58\beta - 13.2 \right) e^{18.4/\lambda} \quad (3-2)$$

with

$$\lambda_i = \frac{1}{\frac{1}{\lambda - 0.02\beta} + \frac{0.003}{1 - \beta^3}} \quad (3-3)$$

The parameters are extracted from [137].

3.1.3 PMSG Model

For the electrical model, the variations of the rotor magnetics are neglected including the saturation, eddy current and field current dynamics. Single-mass model is used to demonstrate the shaft torque in the mechanical model of PMSG. Other detailed models could also be easily implemented. The overall PMSG model in dq axis is:

$$\frac{d}{dt} i_d = \frac{1}{L_d} v_d - \frac{R}{L_d} i_d + \frac{L_q}{L_d} p \omega_r i_q \quad (3-4)$$

$$\frac{d}{dt} i_q = \frac{1}{L_q} v_q - \frac{R}{L_q} i_q + \frac{L_d}{L_q} p \omega_r i_d - \frac{\psi p \omega_r}{L_q} \quad (3-5)$$

$$T_e = 1.5p[\psi i_q + (L_d - L_q)i_d i_q] \quad (3-6)$$

$$\frac{d}{dt} \omega_r = \frac{1}{J} (T_e - T_m - F \omega_r) \quad (3-7)$$

where v_d, v_q, i_d, i_q are the stator voltage and current of PMSG in the d-q axis; R is the stator winding resistance; L_d, L_q are the inductance in the d-q axis; ω_r is the angular velocity of the rotor; p is the pole pair number of the generator; ψ is the amplitude of the flux induced by the permanent magnet in the rotor; T_e and T_m are the electrical and mechanical torque; F represents

the friction coefficient; and finally J is the combined moment of inertia of the wind turbine blades and generator.

3.1.4 Converter Model

The two-level active voltage source AC-DC converter is chosen for both generator side converter and grid side converter. If the switching ripple is omitted, it can be modeled as:

$$v_d = d_d \cdot v_{DC} \quad (3-8)$$

$$v_q = d_q \cdot v_{DC} \quad (3-9)$$

$$i_{DC} = d_d \cdot i_d + d_q \cdot i_q \quad (3-10)$$

where d_d and d_q are the duty ratio in d-q axis; v_d , v_q and i_d , i_q are the voltage and current on the AC side; v_{DC} and i_{DC} are the voltage and current on the DC side.

In some PMSG applications, the generator side converter uses a topology of diode rectifier in series with DC/DC chopper, whose model is explained in [15-17], and could be implemented as well.

The DC-link capacitor can be modeled as:

$$i'_{DC} = i_{DC} - C \frac{dV_{DC}}{dt} \quad (3-11)$$

where i_{DC} and i'_{DC} are the DC-link currents of generator side and grid side converter; V_{DC} is the DC-link voltage; and C is the DC-link capacitance.

For the application of low-voltage ride through, a brake chopper which consists of a resistor and an active switch is installed in the DC-link. During voltage sags, the FCWT system may not inject the full captured wind power. The chopper would engage and dissipate excessive energy and prevent the over-voltage of the DC-link. The model can be expressed as:

$$i_{bc} = \frac{V_{DC}}{R} \quad (3-12)$$

where i_{bc} is the current flow through the brake resistor, and R is the resistance. The brake chopper is served as an emergency back-up plan, and is only enabled when the V_{DC} is above the preset threshold.

3.1.5 Control Functions Implemented into the FCWT Emulator

Shown in Figure 3-1, the control functions are essential parts of the FCWT emulator. They define the behaviors that the FCWT exhibit as wind speed changes and during grid disturbances. As reviewed in Chapter 2 Section 5, the control of FCWT is usually based on the internal current closed-loop controller, and FCWT can inject captured wind energy to the power grid. There are different active and reactive power support scheme proposed in the literature, and they are included in the developed FCWT emulator to showcase their impact to the power system in the HTB system.

Figure 3-2 shows the control functions that are implemented into the controller, it included the existing current closed-loop control, and proposed voltage closed-loop controls. In this section, only current closed-control loop will be presented, and the voltage closed-loop control will be introduced and discussed in the next chapter.

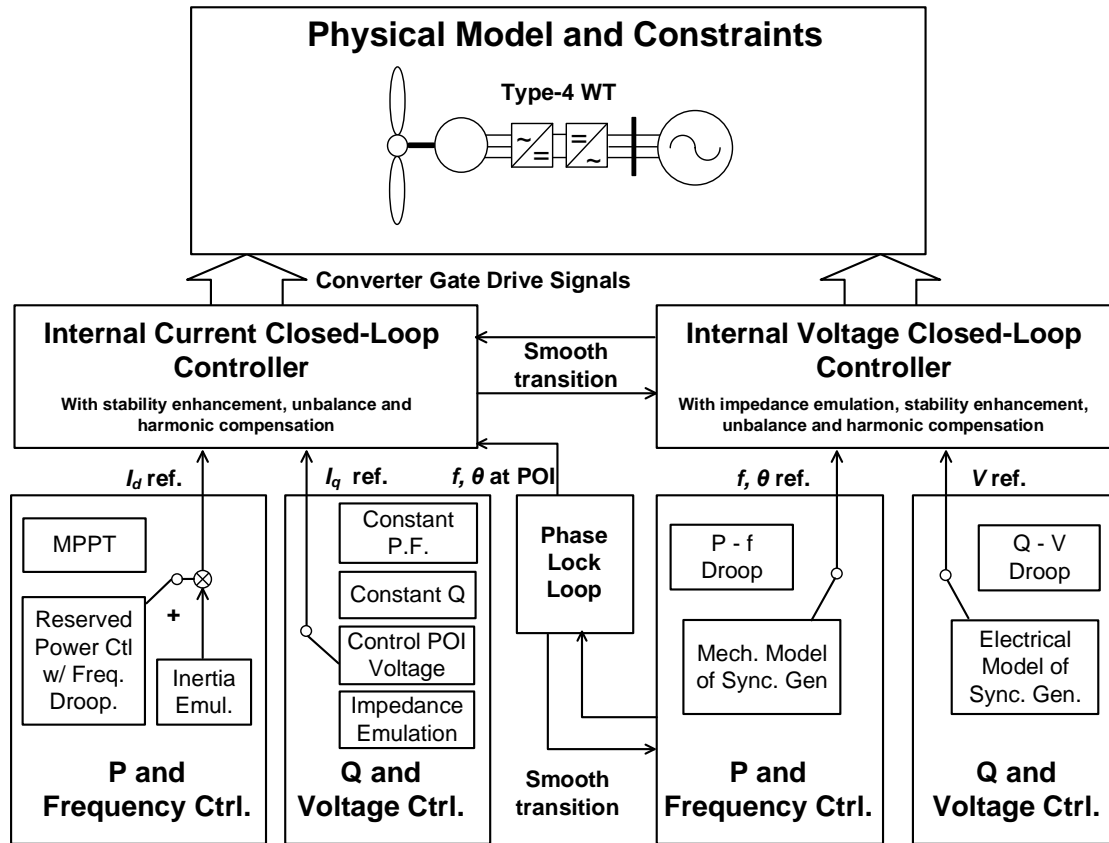


Figure 3-2. Implemented control functions of the FCWT emulator.

The controls have a hierarchical structure shown in Figure 3-3. The current level control is common current feedback control, with cross-coupling terms and voltage feed-forward loop. And it is the same for both generator and grid side converters. For power level control, the power output is controlled by the generator side converter, and the DC-link voltage is controlled by the grid side.

The output power reference is given by the sum of maximum power point tracking (MPPT) algorithm and frequency support control. Figure 3-4 gives the block diagram of the power reference.

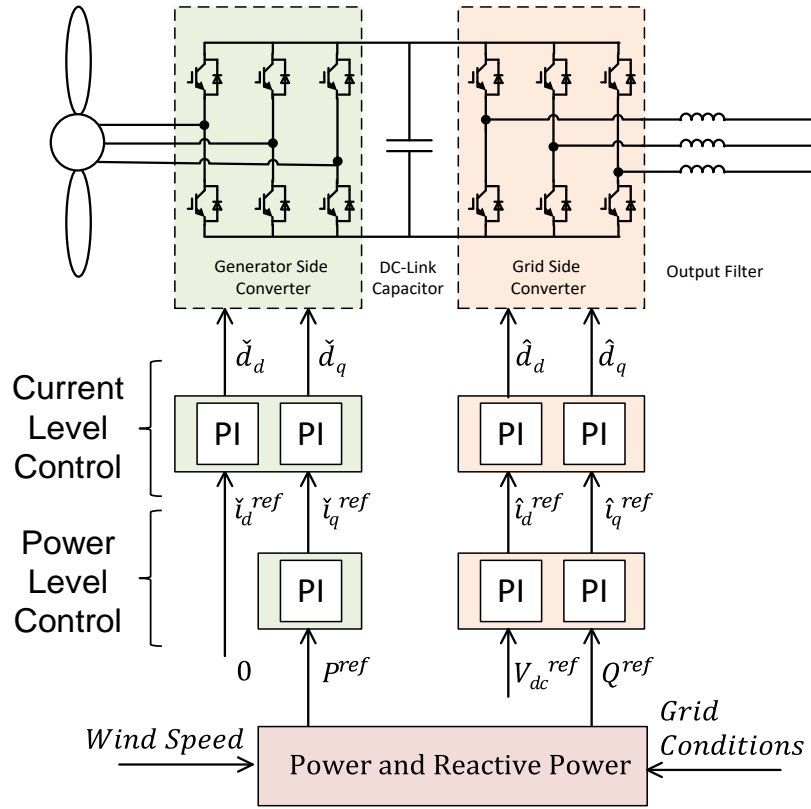


Figure 3-3. Hierarchical control diagram of full-converter wind turbine [136].

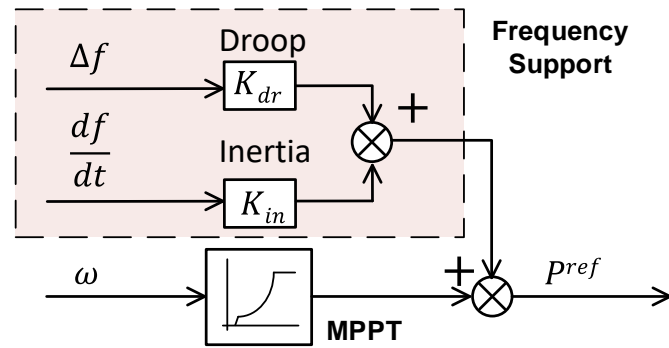


Figure 3-4. Power reference calculation with MPPT and frequency support function [136].

The frequency support part in Figure 3-4 has two aspects. Droop control branch is realized through the deviation of the grid frequency and provides the primary frequency control. Inertia emulation branch is realized by the derivative of the grid frequency change, mimicking the mechanical model of the generator – if the speed of the generator reduces, the kinetic energy must be released.

MPPT methodology is explained in Figure 3-5. Without frequency disturbance, the frequency support function will not trigger, the operating point would converge to the intersection point of the wind power curve and the power reference curve, which is the maximum power point. De-loading characteristics can also be realized by this approach in the same principle.

Reactive power control functions includes constant power factor control, constant reactive power control, point of interconnection (POI) voltage control, and virtual impedance. The control diagram is shown in Figure 3-6.

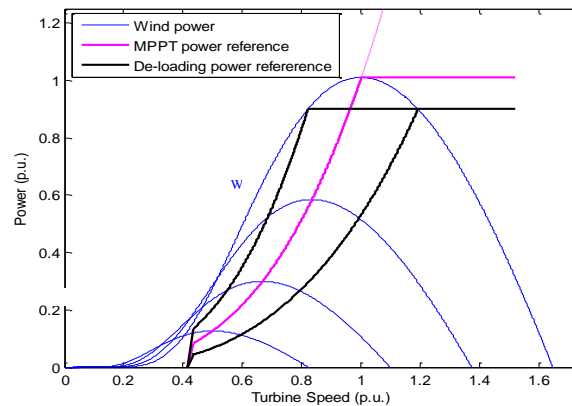


Figure 3-5. MPPT characteristic of FCWT emulator [136].

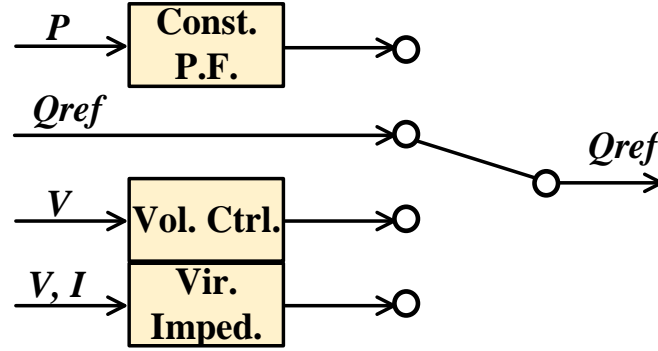


Figure 3-6. Implemented reactive power control for FCWT emulator [136].

3.1.6 Emulator Output Current Reference

The current reference shown in Figure 3-1 is scaled from the current output of the grid side converter. Figure 3-7 shows the two possible ways to set the current reference. One is virtual grid current i_{grid} determined by the grid voltage, the filter, and the converter output voltage, and the other is the current reference i_{grid}^* directly obtained from the output of the DC-link voltage controller.

These two approaches generally speaking have the same performance since the current controller is used to ensure that the output current equals the reference. The former one has two cascaded current controllers, which might introduce delay in the dynamics. And the latter one ignores the physical model, which makes the model less realistic.

In practice, the latter approach is implemented. The emulator current controller is designed to have the same bandwidth as the current controller of the grid side converter. Constraints are set to represent the limitations of the converter duty ratio.

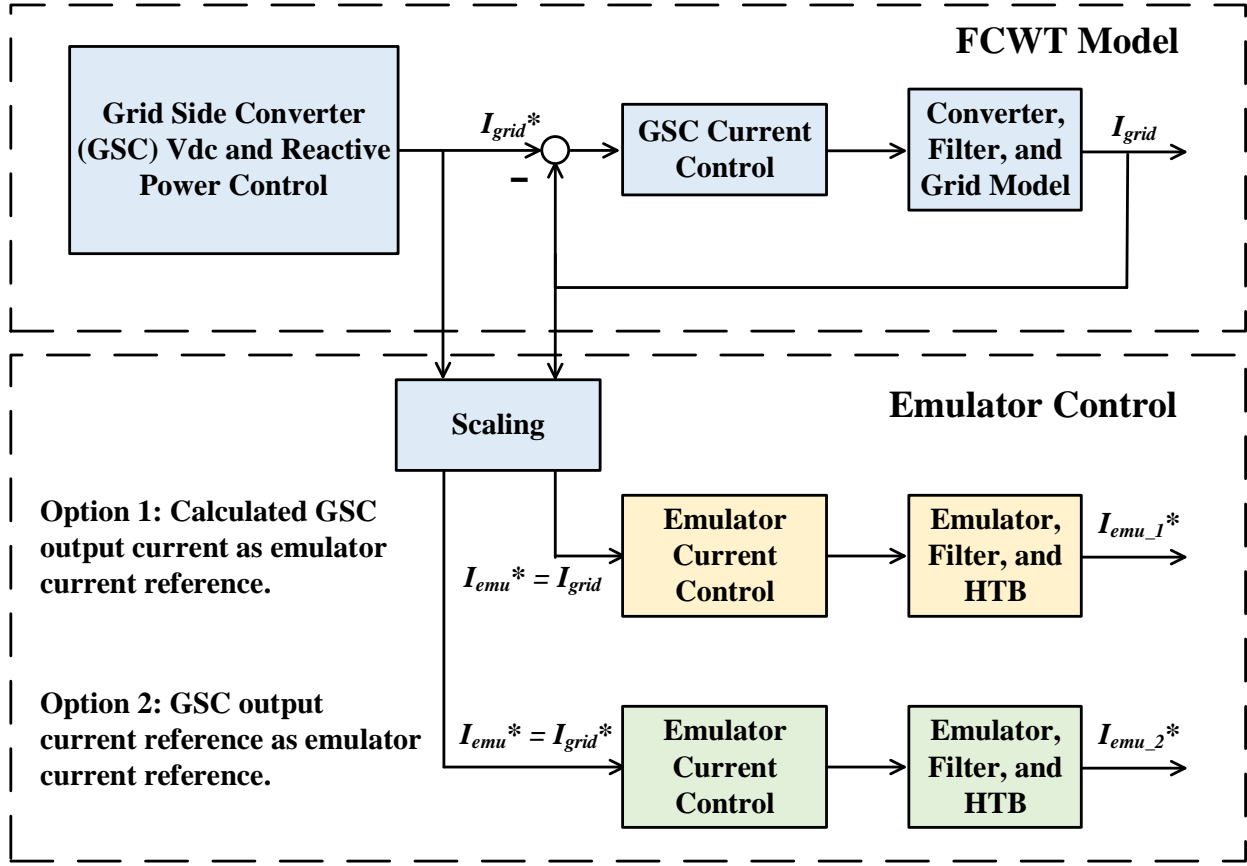


Figure 3-7. Approaches of current reference selection.

3.2 Simulation Results

In order to verify the models above, a detailed switching model of 2 MW PMSG wind turbine was simulated to compare with the emulator in the Simulink platform. The parameters of the PMSG and the passive components are from [12].

Figure 3-8 shows the responses of both models under a turbulent wind speed pattern. Only per unit values were given since the HTB represents the emulated power system by sharing the same

per unit value. In Figure 3-8, high available wind power indicates high wind speed, and turbine speed would be controlled to accelerate to reach optimum tip ratio. Also, when the available power is larger than the rated, the pitch control would start to work to reduce the power input. The two models are well-matched with each other. Thus, the emulator model can be considered as valid.

3.3 Experiment

The experiment topology is developed based on the HTB based two-area system, as shown in Figure 2-3(a). This typical power system allows the testing of inter-area power and frequency oscillation [20]. The system parameters and configuration are shown in Table 3-1. The transmission line is represented by the inductors. The original system parameter in per unit value, designed impedances in the rescaled base, and actual measured impedances are given in Table 3-2 [46].

3.3.1 Case I: Short Period Variable Wind Speed Test

In this case, G1 as infinite bus and G2 as wind turbine are feeding an actual load, other converter emulators are not connected in. Figure 3-9 shows the experiment waveforms when the wind speed changes. The pattern of the wind speed could be either stored in the controller of the wind turbine emulator, or could be specified by the central controller with CAN bus communication in real-time. The waveform indicates that the wind turbine emulator can track to the maximum working point, and if the wind speed is larger than the rated value, the pitch control can be activated to limit the output power.

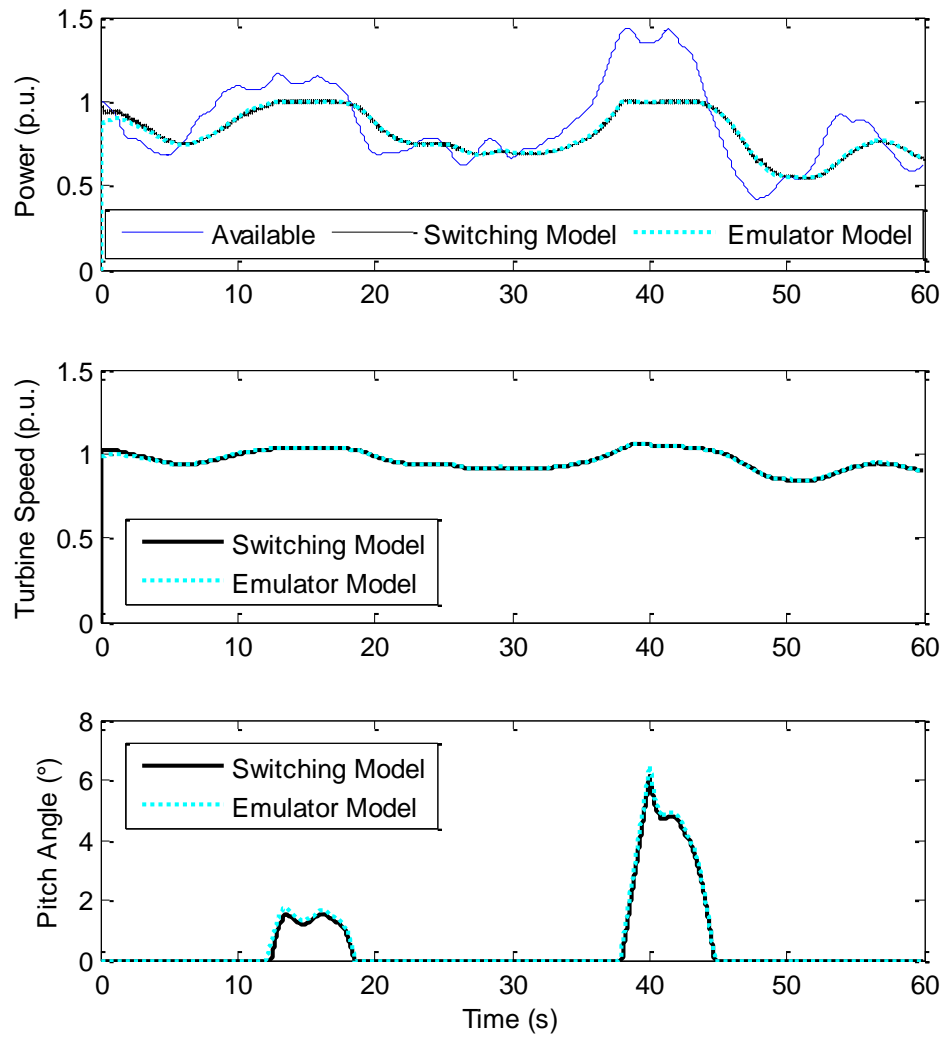


Figure 3-8. Simulation waveforms of wind turbine output power, turbine speed and pitch angle by switching model and emulator model [136].

Table 3-1. Parameters of the experiment platform.

Parameter	Value	Parameter	Value
Original Sys. Voltage	20 kV	Energy Capacity of the Storage	1 min
Original Gen. Power	900 MVA		
Original FCWT Power	630 MVA	$SoC_{setpoint}$	0.75 p.u.
Rescaled Sys. Voltage	85.7 V	SoC_{MPPT}	0.3 p.u.
Rescaled Gen. Power	2552 VA	SoC_{pitch}	0.95 p.u.
Rescaled Wind Power	1876 VA	Inertia (H) G_1	6.5 s
Rescaled Power Base	1876 VA	VSG Emulated H	6.5 s
Rescaled Voltage Base	85.7 V	FCWT Turbine H	4 s
System Freq. Base ω_s	$60 \times 2\pi$ rad/s	Switching Freq. f_{sw}	10 kHz

Table 3-2. Transmission Line Impedances of the Experimental Platform

Name	Original	Rescaled	Measured
L1-6	0.0417 p.u.	2.8 mH + 0.0648 Ω	2.4 mH + 0.15 Ω
L2-6	0.0167 p.u.	1.1 mH + 0 Ω	1.3 mH + 0.06 Ω
L6-7	0.01 p.u.	0.7 mH + 0.026 Ω	0.7 mH + 0.045 Ω
L7-9	0.11 p.u.	7.6 mH + 0.285 Ω	8 mH + 0.39 Ω
L3-10	0.0417 p.u.	2.8 mH + 0.0648 Ω	2.7 mH + 0.16 Ω
L4-10	0.0167 p.u.	1.1 mH + 0 Ω	0.7 mH + 0.02 Ω
L9-10	0.01 p.u.	0.7 mH + 0.026 Ω	0.7 mH + 0.02 Ω

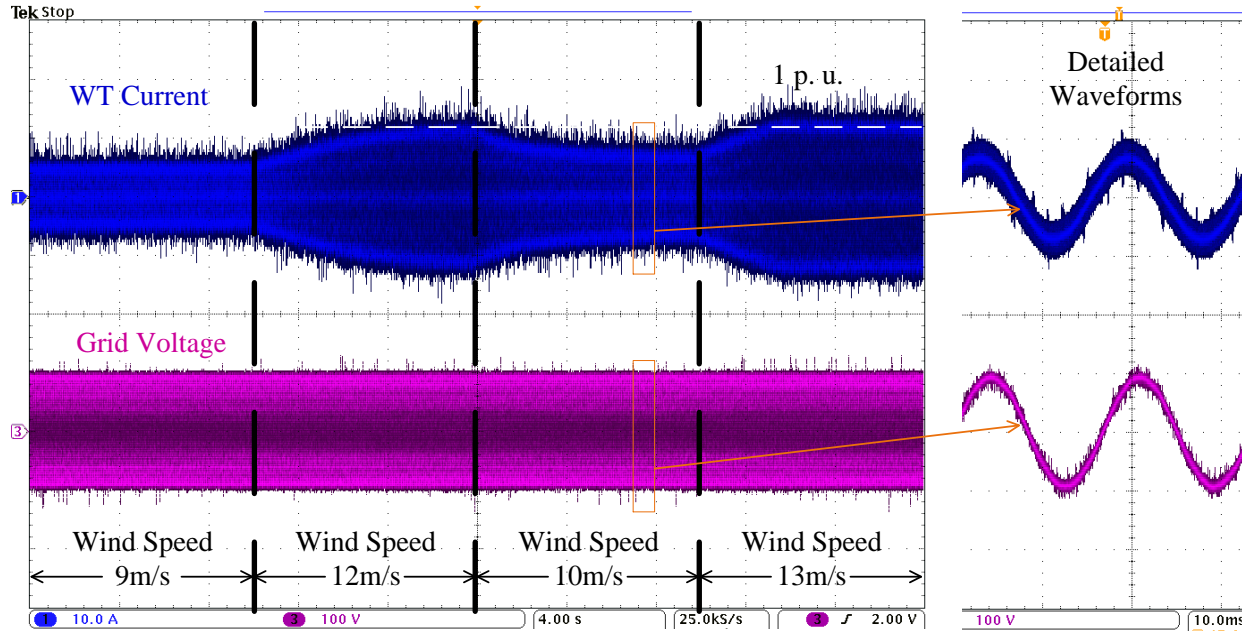


Figure 3-9. Experimental waveforms when emulated wind speed change [136].

3.3.2 Case II: Long Period Variable Wind Speed Test

In order to demonstrate the available control strategies for operation of the future >50% renewable penetration system, a simplified generator-wind-storage system has been established. The capacities of the wind farm and energy storage are chosen to be 58% and 32% respectively, based on the presumed annual profiles to provide the 50% total energy consumption [3, 4]. The actual wind speed time sequence is generated by NREL TurbSim [5]. The experimental result is shown in Figure 3-10. The load was constant with a various wind condition. The storage was controlled in current mode to compensate the active power variation of the wind farm, thus the generators have less power fluctuations due to the storages.

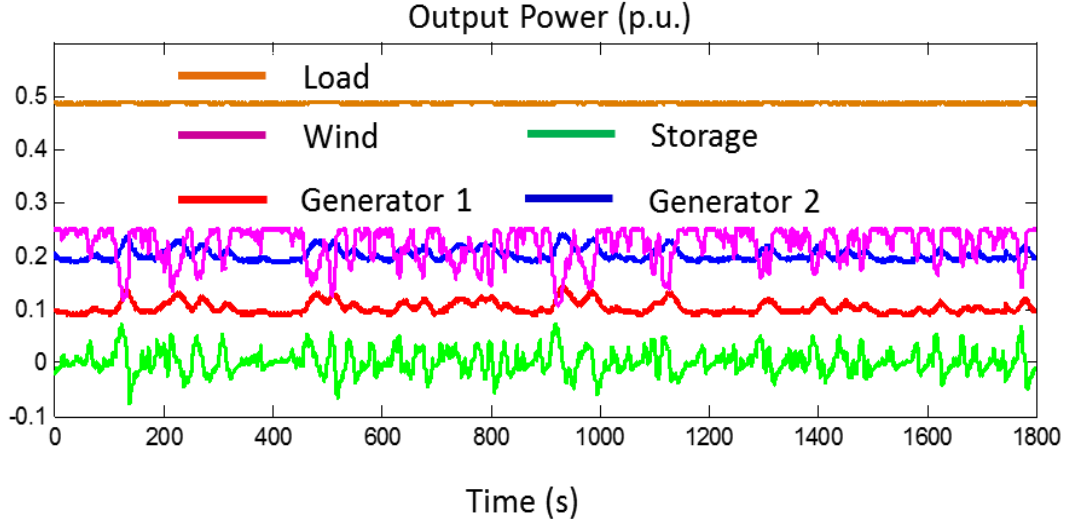


Figure 3-10. Experimental results of FCWT operation in a 50% penetration system.

3.3.3 Case III: Frequency Support by Wind Turbine Test

This case emulates the performance of the frequency support control of the wind turbine. The experiment setup is that G1 as thermal generator and G2 as wind turbine provide power to L7 as a programmable load. Figure 3-11 presents the waveform of the grid frequency, turbine speed, and wind turbine emulator output power when a large sudden load change occurs at 0 s. If frequency support control is enabled, the wind turbine would generate additional power to damp the grid frequency change, and this released kinetic energy from the turbine rotor would cause it to decelerate. This experiment case shows that the wind turbine emulator could react to grid disturbance as expected, and both control strategies can achieve good frequency performance in terms of the oscillation peak of the grid frequency and its changing rate.

3.3.4 Case IV: Two Area System Frequency Oscillation Test

In order to compare the results of the two area system frequency oscillation, three scenarios are tested. Four-generator scenario (G1, G2, G3, G4) serves as the benchmark. And G4 is then substituted to FCWT model with and without frequency control. The grid disturbance is triggered by a 0.1 p.u. load change at L7. Figure 3-12 gives the system frequency performances.

The waveforms show that if without frequency control, the wind penetration deteriorates the system frequency response in both areas. But it can achieve similar results with the four generator case with proper control.

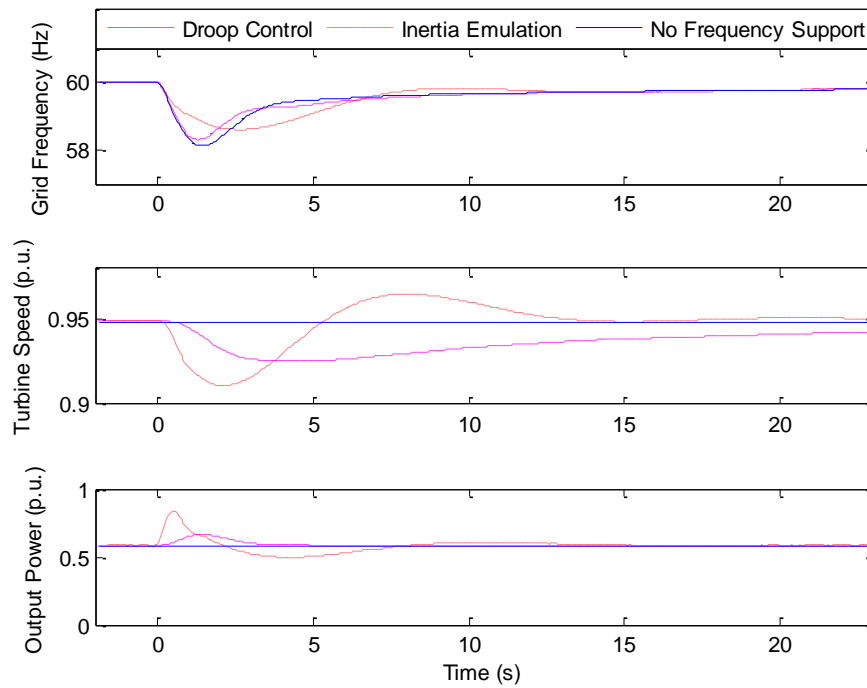


Figure 3-11. Experiment waveforms of grid frequency, turbine speed, and wind turbine output power during frequency drop disturbance [136].

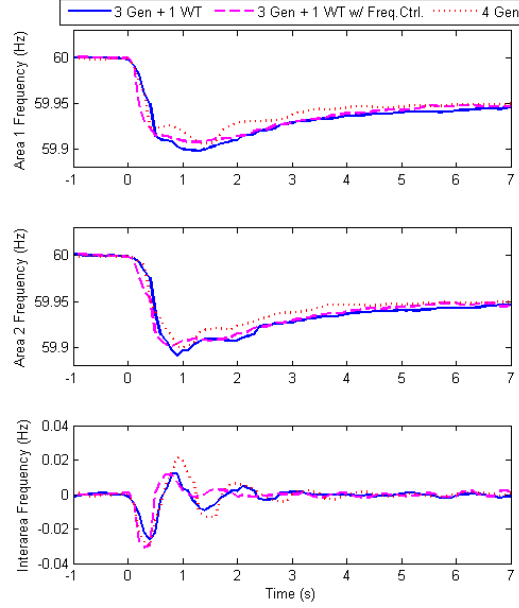


Figure 3-12. Experiment waveforms of grid frequencies of two area system with wind turbine penetration [136].

The two area system topology also offers the opportunities to emulate interaction of the wind turbines inside of a wind farm. It is achieved by switching G3, G4 and L7 to the FCWT emulator. Thus the whole system becomes a remote wind farm connect with the power system through a long transmission line.

3.3.5 Case V: Operation with Low Terminal Voltages

In Figure 3-13, various grid voltage levels were applied to the wind turbine emulator in the HTB experimental set-up, the wind turbine emulator can maintain the output active power, and generate different reactive power to support the PCC voltage. While the voltage is under certain threshold, the active current limiting and reactive current injection will be enabled to help with the

grid voltage recovering. The overall current is within 1 p.u. to prevent damage the converter itself.

3.4 Discussion

The FCWT emulator has been developed and tested in the HTB two-area-system shown in Figure 2-3(a), and continued to serve as critical components in the following expansion of the HTB emulations in the three-area-system and four-area-system shown in Figure 2-3(b) and (c). and participate in different level of system level controls, as shown in Figure 3-14. It has also been used to develop and demonstrate other advanced power system controls including inertia scheduling and wide area damping control [54].

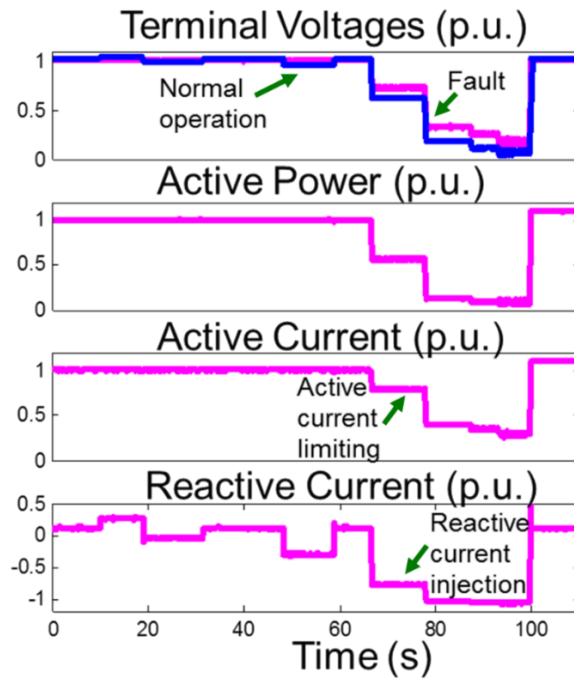


Figure 3-13. Experimental results of FCWT fault operation.

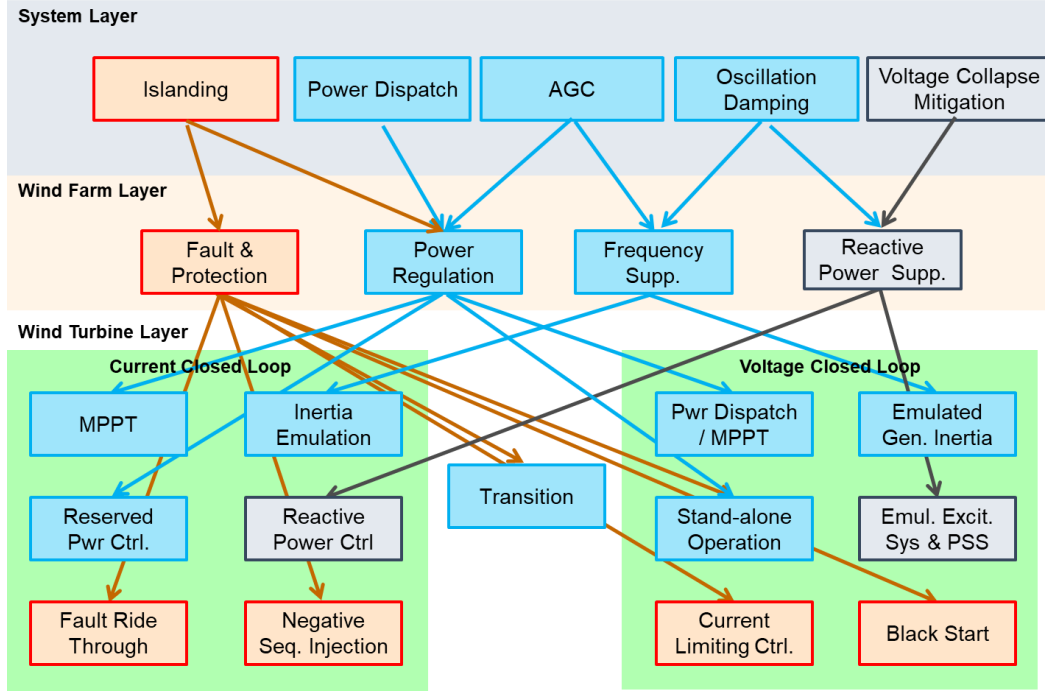


Figure 3-14. System level control of the FCWT.

3.5 Conclusion

A converter based full-converter wind turbine emulator is designed and implemented using the multi-converter emulation experiment scenario. A well-controlled physical model of wind turbine is adopted as the reference for the emulator converter to follow. Thus the emulator behaves in the same way as the modeled wind turbine both under steady-state and transient conditions.

Simulation and experiment results demonstrate the performance of the emulator during variable wind speed, and verified the feasibility of this emulation approach. A two area system of the converter emulators is built to test the interactions between the wind turbine and power system components in real-time, offering possibilities to test various grid control of the system.

4 Virtual Synchronous Generator Control of Full Converter Wind Turbine with Short Term Energy Storage

As mentioned in section 2.5.2, there has been a lot of literature working on the VSG controlled voltage sources. But most of them have assumed the energy storage has infinite capacity to support all the control objectives.

This chapter mainly focuses on the virtual synchronous generator control of the full converter wind turbine. The system structure and detailed control strategies are introduced. The testing result using the previous developed FCWT emulator in the HTB has presented [138, 139].

4.1 Structure and Basic Control Principle

FCWT adopts an ac/dc/ac structure to transfer the captured energy from the wind generator to the grid, as shown in Figure 4-1. A minute-level energy storage is connected to the dc link of the system to help with maintaining the dispatch command.

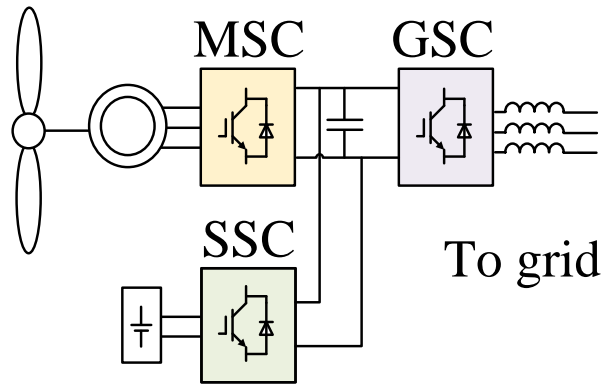


Figure 4-1. FCWT system under study [139].

As the output characteristics of the WT is determined by the emulated generator, the grid side converter (GSC) determines the output power by the grid condition and system dispatch. The other converters will then maintain the power balance of the WT generation system. The storage side converter (SSC) controls the dc link voltage by charging or discharging the energy storage. The machine side converter (MSC) controls the wind generation to match the load condition of the GSC by adjusting the turbine rotating speed.

The operation diagram of the VSG controlled FCWT is shown in Figure 4-2. In VSG normal operation, the State of Charge (SoC) of the storage will be controlled around $SoC_{setpoint}$. If it is higher, that means MSC generates more power than needed by the GSC, the power generation should be reduced, and vice versa. When SoC drops low, the control will make transition to VSG MPPT mode: in which MSC generates the maximum available power, and GSC will output the generated power while preserving the SG dynamics including inertia response, voltage-var control, etc. On the other hand, when SoC is too high, pitch control will be enabled to reduce the power intake. E_1 to E_4 in the figure indicates the energy capacity for each SoC section.

Figure 4-3 gives the overall operation state machine. When a grid fault occurs, power electronic converters based generation cannot sustain as large fault currents as SGs do. During the grid fault, the control will transition to focus on protecting itself, and back to normal VSG control when the fault is cleared. The system will trip and shutdown itself if: 1) the fault lasts too long for the FCWT to ride-through; 2) an internal fault is detected in the FCWT; 3) grid voltage and frequency are outside of normal operation limits for an extended period of time as grid code requires [140]; or 4) the system operator commands it to shut down.

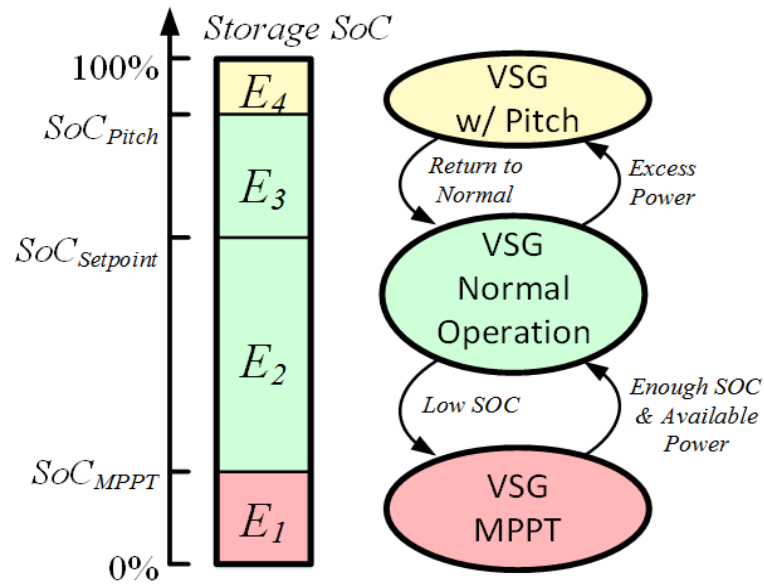


Figure 4-2. Operation diagram for VSG controlled FCWT [139].

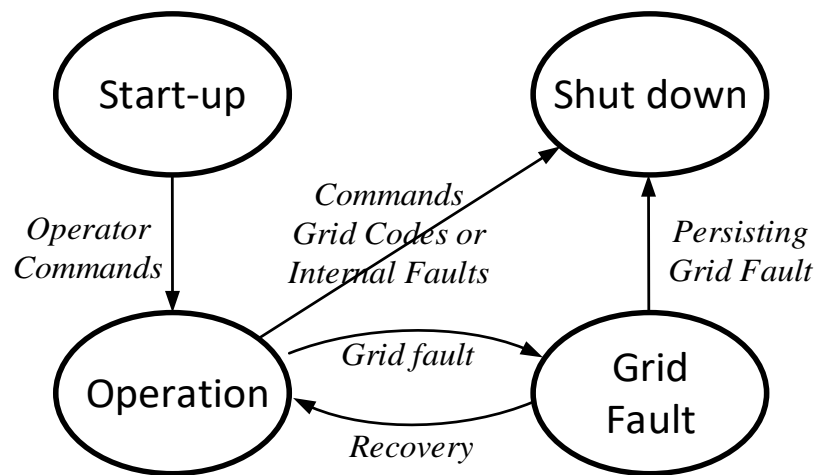


Figure 4-3. Operation state machine for VSG controlled FCWT [139].

The detailed control strategies for each component and sizing discussion of the energy storage will be presented next in subsection 4.3.

4.2 Detailed Control Strategy

4.2.1 Grid Side Converter Control

In order to mimic the behavior of a synchronous generator, the GSC measures the output currents i_{dq} of the WT, and feeds them into the emulated generator's model. The voltage and angular frequency outputs from the model V_{dq}^* and ω_r are closed-loop controlled by the GSC, thus it can be considered to supply steady voltage source to the power system or directly to the loads in the stand-alone operation. The overall control diagram is shown in Figure 4-4(a), where d_{dq} and d_{abc} are the PWM control duty ratios of the GSC in dq and abc axis respectively.

The output voltage reference is calculated through the electrical model of the generator, shown in Figure 4-4(b), where e_{fd} is the field winding voltage, x_d and x_q are the synchronous reactances; x'_d and x'_q are the transient reactances; T'_{do} and T'_{qo} are the transient open-circuit time constants, E'_d and E'_q are transient back EMFs; u_t is the terminal voltage amplitude; U_{tref} is the voltage reference given by the operator; K_A and T_e are the gain and time constant of the excitation system; and E_{fmax} and E_{fmin} are the maximum allowable field voltage.

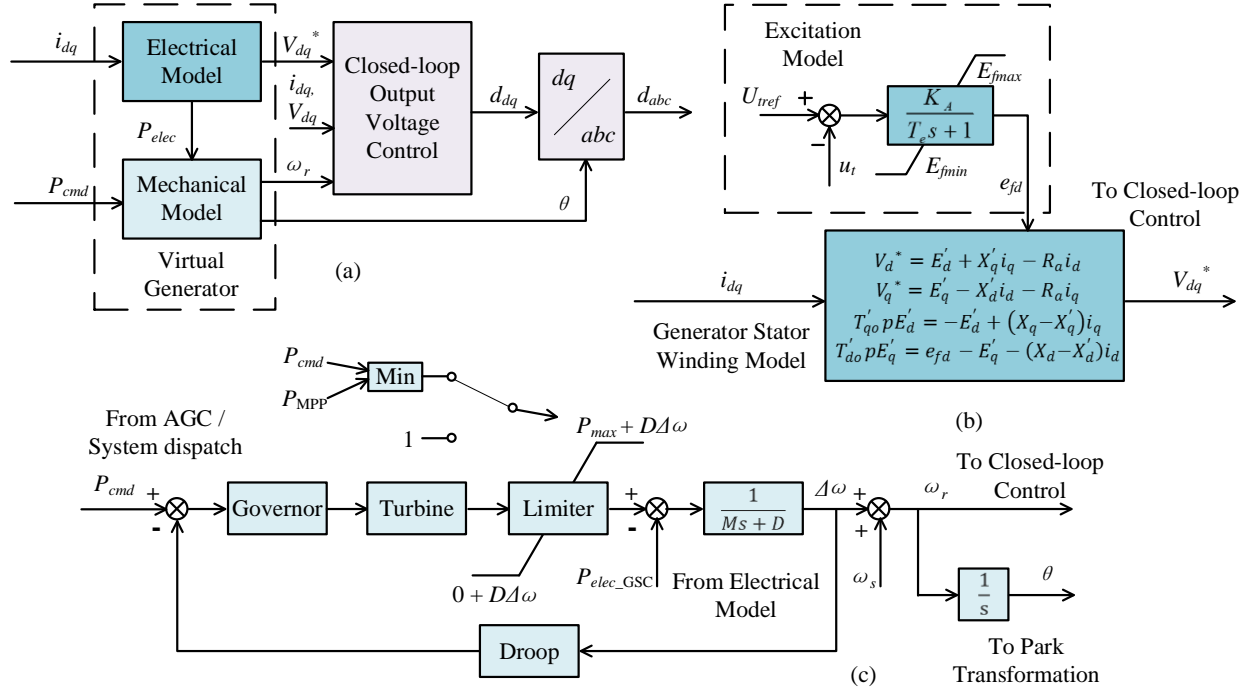


Figure 4-4. GSC control to mimic SG behavior in power system: (a) overall control diagram; (b) electrical model; (c) mechanical model [139].

The output frequency is determined by the mechanical model of the virtual generator, demonstrated in Figure 4-4(c). P_{cmd} is the power reference given by the system dispatch. M and D are the inertia constant and the mechanical friction caused damping factor, ω_r is the rotor speed, ω_s is the synchronous speed and the angle θ is given to the park transformation of the converter control. Different from spinning generators, the parameters of the VSG can be set arbitrarily according to the system needs, and be changed dynamically in real time. In this dissertation, actual generator's parameters are chosen to show the feasibility of the control. The stability analysis can be found in [107-109]

The GSC synchronizes with the grid frequency by using the swing equation provided by the mechanical model of the virtual generator, without the help of the PLL. The inertia-frequency response can be intrinsically emulated through the VSG control. In addition, power system controls developed for SGs can also be implemented, including: automatic generation control (AGC), automatic voltage regulator (AVR), power system stabilizer (PSS), etc [49].

By implementing the electrical and mechanical model of the SG, the output power of the WT is determined by the grid and load condition. It is possible that the output power exceeds the maximum available power from the wind, and it is also possible that the GSC will absorb power when the grid frequency is higher than the nominal value.

A power limiting function is then proposed and implemented in Figure 4-4(c) for these two possible scenarios. P_{max} is the maximum power allowed in steady state, while the minimum power output is 0, keeping it from going negative. $D\Delta\omega$ is the steady state error of the inertia block, and it is added to the limits in order to compensate the error. Thus in grid-connected condition, the implemented limiter will keep the GSC electric power output P_{elec_GSC} within the thresholds in the steady state.

P_{max} is set to be the smaller value between the power dispatch value P_{cmd} and the maximum available wind power P_{MPP} , as it is preferable to output its maximum power when it cannot fulfill the demand during low wind period. P_{MPP} is determined as the WT reaches maximum power point (MPP) through the sector identification explained in subsection 4.2.3. If the FCWT operates in the VSG MPPT mode shown in Figure 4-2, the MPP limiter would be in effect. In this case, the WT can achieve the MPPT control, while maintaining generator dynamics during the transients.

During stand-alone operation, the WT is operating without a voltage source provided by the traditional generator. Thus its output power is solely determined by the load. In this situation, if the output electrical power of the virtual generator becomes larger than the P_{max} provide by the limiter, the output frequency will be greatly decreased. Under Frequency Load Shedding (UFLS) mechanism will then be triggered and reduce the system load until the generation-load system reaches equilibrium. If still not enough, the FCWT will be shut down to prevent further damage.

The inner closed-loop output voltage control of the GSC can be implemented by single loop or double loop with inner current control loop. The control block diagram for d axis is shown in Figure 4-5 as an example, where L_f is the output inductor filter of the GSC, decoupling indicates the cross-coupling terms for current and voltage control in dq axis, LPF indicates the signal conditioning low pass filter for the measured voltage and currents, ω_{fc} and ω_{fv} are the cut-off frequency for the corresponding LPFs. The detailed controller design can refer to [34, 141, 142].

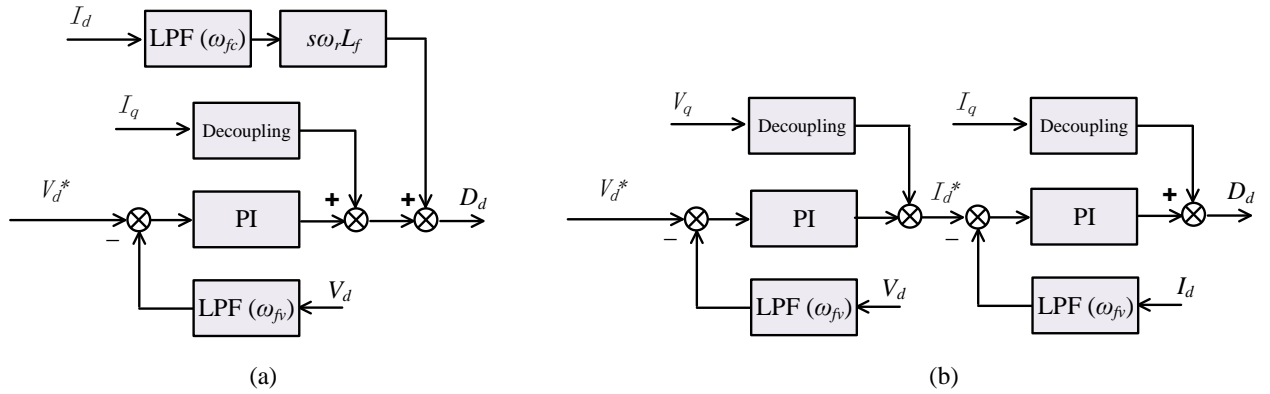


Figure 4-5. GSC inner closed-loop output voltage control for d axis: (a) single loop; (b) double loop with inner current control loop [139].

4.2.2 Storage Side Converter Control

The control diagram is shown in Figure 4-6, where V_{dc} is the dc link voltage of the FCWT, V_{dc}^* is the voltage reference, and $I_{dc_stor}^*$ is the current reference of the energy storage converter. Thus, the dc voltage can be maintained with allowable *SoC*. Since the storage is being charged and discharged whenever there is power unbalance between the MSC generation and GSC consumption, a relatively fast responding storage technology is recommended for the application. The detailed model and corresponding current controls should be selected and designed according to the specific storage technology [115, 143, 144], and will not be further discussed in this dissertation.

4.2.3 Machine Side Converter Control

MSC controls the rotor speed of the turbine, and thus the power balance can be achieved by moving the operating point along the wind characteristic curve. As discussed in Section II, *SoC* of the storage is used as the input of the speed loop, as shown in Figure 4-7.

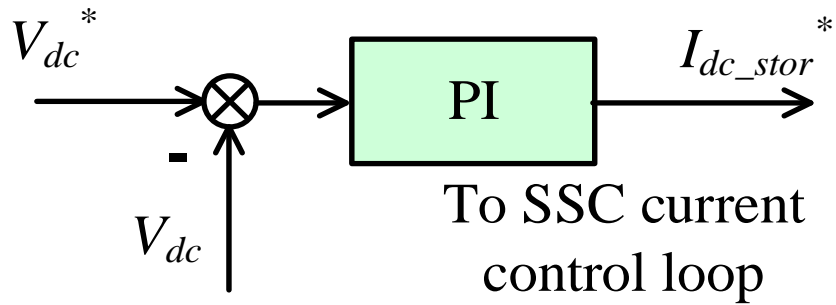


Figure 4-6. SSC control to maintain dc voltage [139].

The speed reference ω^* is generated by a PI controller. The PI parameters are chosen based on the operating condition of the wind turbine [112]. As shown in Figure 4-8, there are two possible operating points *A* and *B*, given a certain desired output wind power: *A* is to the left of the MPP, with positive curve slope, requires positive PI parameters; while *B* is to the right with negative curve slope, and requires negative PI parameters. Note that operating point *A* is in Sector 1 and *B* is in Sector 2. Whenever a sector transition is identified, the PI controller will undergo a procedure to keep the output ω^* the same as the previous control cycle, and hence provide a smooth transition between the sectors.

Typically operating in Sector 2 provides more kinetic energy for dynamic response, and it is easier to design the PI parameters of the turbine speed control [112]. However, due to the mechanical constraints, the wind turbines are not designed to operate at high rotational speed. In this dissertation, a maximum rotor speed ω_{max}^* is assumed to be 1.2 p.u. Thus, the wind turbine has to be able to operate in both Sectors. Then the turbine speed is controlled by inner current loop [145, 146], which will not be discussed further.

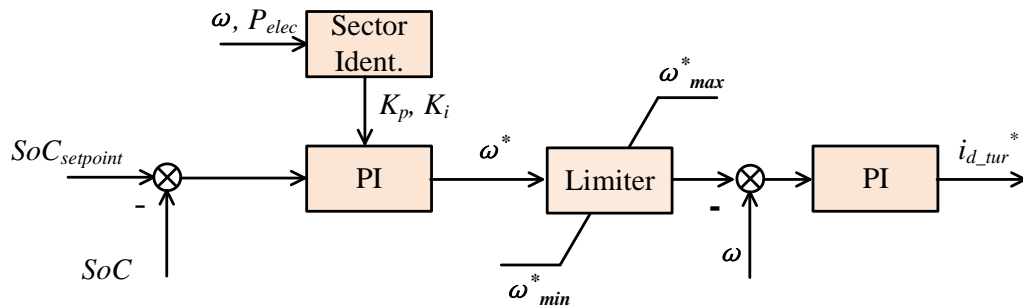


Figure 4-7. MSC control to adjust turbine rotor speed [139].

The identification of the operating point sector is important for the control and operation of the MSC, otherwise the wrong PI parameters will be applied. Intuitively, the operating sector can be recognized by the relationship of the changing direction of the wind power P_w and rotor speed ω , as shown in (4-1). However, since wind turbines usually have relatively large inertia constant, the actual wind power is hard to be estimated through the measurement of the electric power P_e and the rotor speed. Misidentification will be caused by external noise and measurement error of the rotor speed.

$$\begin{cases} \Delta P_w \cdot \Delta \omega > 0 & \text{Sector 1} \\ \Delta P_w \cdot \Delta \omega < 0 & \text{Sector 2} \end{cases} \quad (4-1)$$

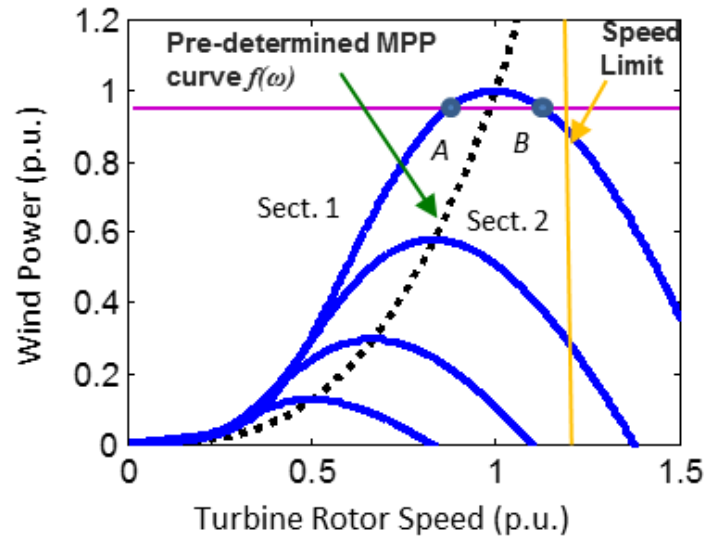


Figure 4-8. Wind characteristic curve showing the sector definition and pre-determined MPP curve $f(\omega)$ [139].

Therefore, identification criterion (4-2) is proposed in this chapter, by directly using ω and P_e , and the pre-determined MPP curve $f(\omega)$, which is the dashed curve shown in Figure 4-8. This curve is usually provided by the manufacturer and used for the traditional maximum power point tracking (MPPT) control, and it is usually close to the cubic function of the rotor speed ($f(\omega) \approx k\omega^3$). Thus, when the electric power output of the wind turbine is above the supposed MPP curve, it is working under Sector 1 and vice versa.

$$\begin{cases} P_e > f(\omega) & \text{Sector 1} \\ P_e < f(\omega) & \text{Sector 2} \end{cases} \quad (4-2)$$

The electric power output P_e is the difference of the wind power and the kinetic energy absorbed by the turbine rotor. Misidentification happens when the turbine is accelerating in Sector 1, or decelerating in Sector 2, in other words, when the turbine is moving toward the MPP. It is tolerable because: (1) when it reaches closer to the MPP, the wind power input does not change much, and (2) it helps to slow down the speed control loop by applying the opposite direction to the controller. When the identification is constantly switching between the sectors, it can be recognized that the WT is already working under the MPP, and no additional wind power is available.

4.2.4 Pitch Control

If SoC of the energy storage rises to the SoC_{Pitch} threshold in Figure 4-2, or the electrical power of MSC is larger than the rated power P_{rated} due to a wind gust, then pitch control is enabled to spill the excess power. The control is adopted as shown in Figure 4-9, in which β represents the pitch angle.

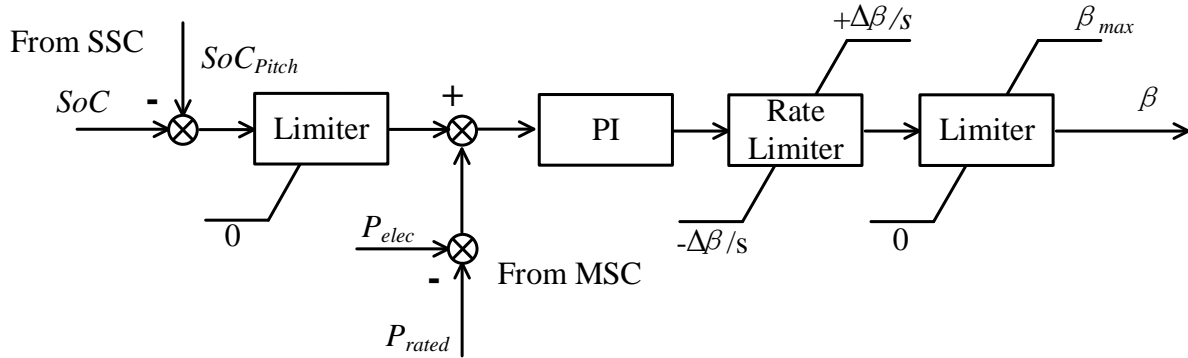


Figure 4-9. Pitch control to reduce excessive power [139].

4.2.5 Discussion on Sizing of the Energy Storage

As described in previous sections, in VSG normal operation, the energy storage helps to maintain the dispatched power until the SoC reaches the thresholds of SoC_{MPPT} and SoC_{Pitch} . Thus the energy capacities E_2 and E_3 in Figure 4-2 will be utilized to: (1) provide the energy to control the rotor speed of the WT to the desired value during the transients; and (2) carry out the power demanded by the load in stand-alone condition, or the commands dispatched from the system operator.

Since E_2 and E_3 is to provide or absorb kinetic energy for the WT rotor during VSG normal operation, the design of them have to be large enough to accelerate or decelerate the wind turbine to its new operating point when wind speed or system command change. Since most modern FCWTs have the inertia constant around 3-5 s [147, 148], E_2 and E_3 should at least be designed to that value, with some margin to provide the GSC output power during the transient. Higher margin

would allow slower transient that the wind turbine move to its new steady-state operating points, which lead to lower strain on the mechanical and power electronics devices. In this chapter, a minimum 12 s rated power of energy capacity of E_2 and E_3 is selected to ensure the smooth operation of the rotor speed control loop.

On the other hand, E_2 will also be used to compensate the power difference between the GSC and MSC during low wind conditions. If the command power is less than the available wind power, the energy capacity of E_2 should be able to provide the requested power until the next control cycle. Thus, E_2 should size:

$$E_{2design} = T_{interv} \times P_{rated} \times Err_{forecast} \quad (4-3)$$

where T_{interv} is the time interval of wind forecast and system dispatch, and $Err_{forecast}$ is the error percentage of the wind forecast. Assuming 5 minutes' interval [116], and 10% error [149], 30 s rated power of energy capacity should be designed for E_2 . As it is always easier to spill extra power through pitch control, E_3 can be designed smaller to support the dynamics of the GSC and MSC, without considering the impact of forecast.

Below the SoC_{MPPT} threshold, the WT will transition to the VSG MPPT mode, in which power limiter in Figure 4-4 will take action and reduce the output power of the wind turbine to the maximum available. This mode allows the system operator to reset the setpoint according to the forecast. The storage will begin to recharge when the wind power is larger than the demanded power. So E_1 should be designed to provide the energy for SG dynamics during contingencies. The required energy for the inertial response to a frequency event can be estimated as

$$E_{1design} = H \times \frac{\omega_s^2 - \omega_{nadir}^2}{\omega_s^2} \times P_{rated} \quad (4-4)$$

where H is the inertia constant of the emulated SG, ω_s is the synchronous speed, and ω_{nadir} is the lowest frequency during the event. Assume the inertia constant is 5 s, and the maximum frequency contingency to be 58 Hz, E_1 should at least be 0.33 s rated power of energy. However, considering that the FCWT system can no longer be controlled if the storage runs out of energy during the transient. E_1 can be designed with larger margin.

Similarly, E_4 is the energy buffer for the surplus power. Its design depends on the speed of the pitch control. Assuming the pitch rate is 8 °/s [150], 2 s will be enough for the power to reduce to the GSC demands, and hence the E_4 energy capacity can be designed around it, with some margin to avoid over-charging the energy storage

Overall, E_1 to E_4 together can be designed to minute-level, which is the assumption of this dissertation.

4.3 Experimental Results

4.3.1 Experiment Platform

The experiment topology is developed based on the Kundur two-area system, where the generators on bus 2 and bus 3 are replaced by the FCWTs with 70% of the original power rating, such that the wind power takes around 40% of the total generation capacity. Figure 4-10 shows the topology of the hardware platform of the emulated two area system. The system parameters and configuration are shown in Table 3-1 and Table 3-2.

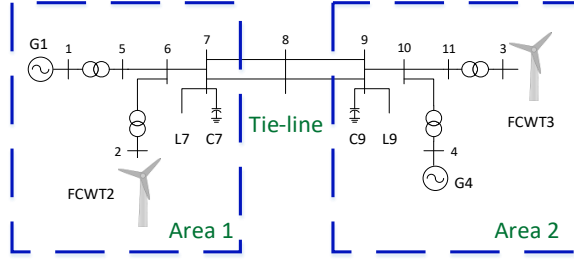


Figure 4-10. Emulated two-area system topology [139].

4.3.2 Control Parameters

Thus, the controller parameters can be designed to make sure the converters can operate stably individually and together in the system, by repetitively applying the stability methods, and check whether if the system is stable under the control parameters under trial.

The single loop voltage control with current feedforward compensation is used for the grid-connected and stand-alone operation experiments, as shown in Figure 4-5(a), and the designed control parameters are given in Table 4-1.

Table 4-1. Voltage Closed-Loop Controller Parameters

Controller Parameters		Values
Voltage controller	K_{vp}	0.016
	K_{vi}	5
Current measurement filter	ω_{fc}	$1000 \times 2\pi$ rad/s
Voltage measurement filter	ω_{fv}	$300 \times 2\pi$ rad/s

4.3.3 Grid Connected Operation of Proposed VSG Control

The experimental results Figure 4-11 to Figure 4-13 are obtained with only area 1 enabled, where G1 and FCWT2 are supplying load at bus 7. Figure 4-11 shows the experimental results with mode transitions of the VSG operation. Before t_1 the wind speed is set to be 10 m/s, and SoC is lower than the SoC_{MPPT} , the FCWT is working under VSG MPPT mode. At t_1 , wind speed changes to 12 m/s, and rotor speed starts to change to capture more wind power, and charge the energy storage. At t_2 it is able to fulfill the system dispatch, and transition to VSG normal operation. After t_3 wind speed changes back to 10 m/s, and FCWT can continue to output the system command power until t_4 when SoC drops to the lower threshold. It transitions back to the VSG MPPT mode. Wind speed changes to 15 m/s at t_5 ; at this moment, the captured wind is larger than the rated value, so pitch control quickly enables to spill the excess power, and back to the normal operation again.

Figure 4-12 shows the experimental results with the FCWT transition between the VSG MPPT mode and the traditional MPPT mode without VSG control, in which the green shaded area indicates the WT is working under VSG MPPT mode, and white area indicates the WT is working under traditional MPPT mode. Both control modes can track the wind variation and output maximum power. But the behavior is different when there is a large disturbance in the grid, such as the load step change in Figure 4-12. Traditional MPPT will not change its power injection, while VSG MPPT will provide the inertia response in the first few seconds, and help with the frequency control of the system.

Figure 4-13 shows the performance of the system under variable wind conditions, the time

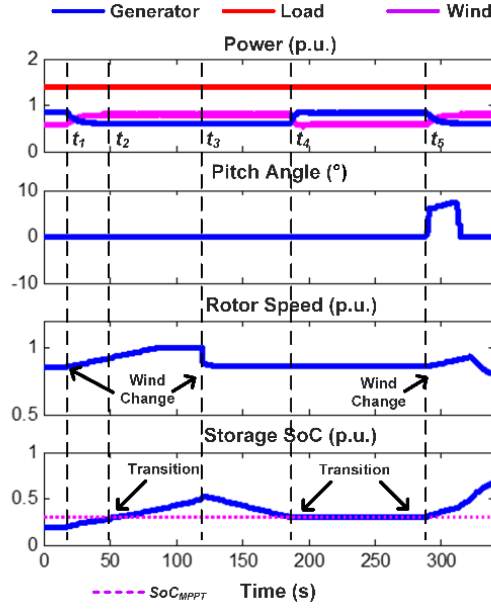


Figure 4-11. Experimental results of grid-connected operation with mode transitions between VSG normal operation and VSG MPPT mode [139].

sequence of the wind speed is generated by NREL TurbSim [151]. A higher SOC_{MPPT} (0.6 p.u.) is assumed in this result just for displaying the transition from VSG MPPT mode to VSG normal operation. After transition at around 150 s, SOC_{MPPT} changed back to 0.3 p.u. to avoid frequent mode transition. In the beginning, the output power is limited to the maximum available power, and the storage charges when the wind power is higher than the system power dispatch (0.8 p.u.); once the SoC is high enough and reaches the predetermined threshold, the WT transitions to normal operation and carries out the dispatch commands.

Dynamic performance of the VSG control is shown in Figure 4-14. The results are obtained with the full two-area system. It shows the power and frequency response at bus 3, when a load

step-change of 0.6 p.u. power happens around 1 s. Traditional MPPT has the worst result, while VSG normal operation and VSG MPPT modes provide active power injection during the frequency event, and hence less frequency nadir.

4.3.4 Stand-alone Operation of Proposed VSG Control

Figure 4-15 shows the experimental result with the FCWT2 supplying the load on bus 7 by its own, while G1 and all components in area 2 were disconnected. In VSG normal operation, the FCWT can adjust the rotor speed and pitch angle according to the load condition, even if the load is larger than the available wind power. When *SoC* drops to the threshold, the power limit block is enabled, and system frequency drops rapidly. The UFLS protection triggers to reduce the load until it is within the available power. The settings are presented in Table 4-2 [152].

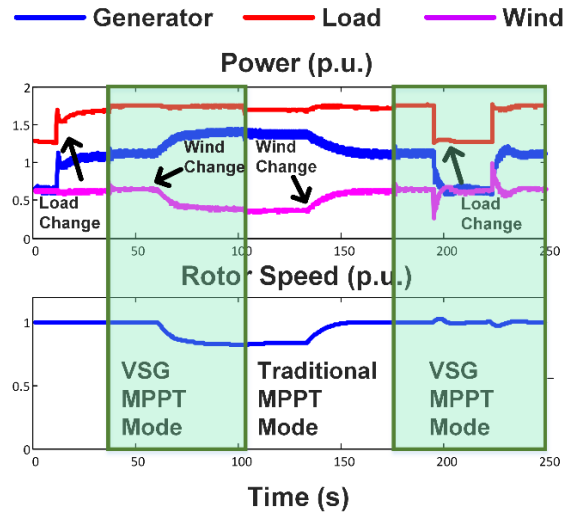


Figure 4-12. Grid-connected operation experimental results to compare traditional MPPT and VSG MPPT mode [139].

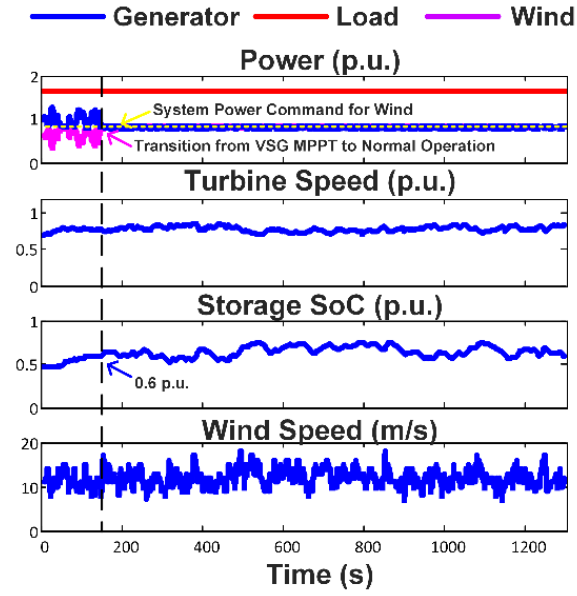


Figure 4-13. Experimental results with variable wind speed showing VSG mode carry out the dispatch commands [139].

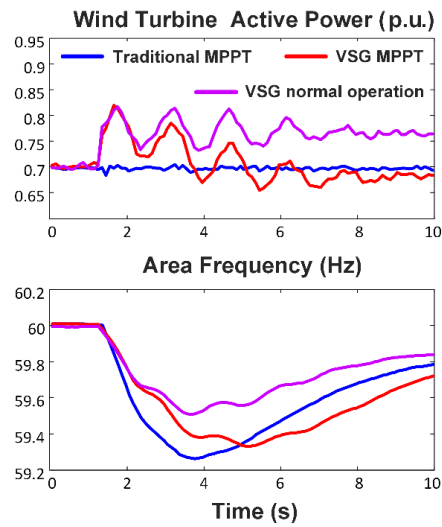


Figure 4-14. Experimental results of dynamic performance of the VSG control showing better frequency responses [139].

Table 4-2. Under-frequency Load Shedding Settings

Load Shedding Block	Percentage of Load Dropped	Frequency Set Point
1	5.3	59.1
2	5.9	58.9
3	6.5	58.7
4	6.7	58.5
5	6.7	58.3

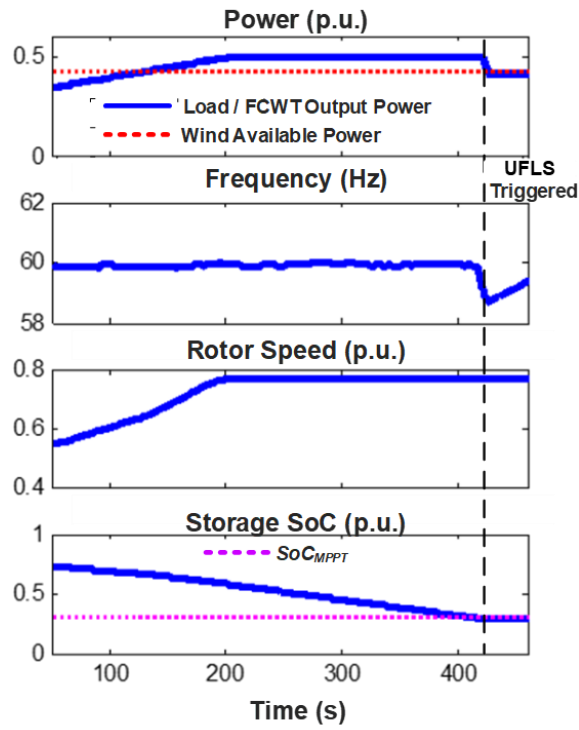


Figure 4-15. Experimental results of FCWT in stand-alone condition, adjusting the operating points to accommodate the load [139].

If the load does not have UFLS protection equipped, the output frequency will keep dropping until the event is then considered as an internal fault, and the FCWT will trip itself and go into the shutdown state as shown in Figure 4-3.

4.3.5 Current Limiting Operation During Fault

To protect the converters from the large fault current, current limiting techniques should be adopted to restrain the output current. For the cases with single voltage control loop, larger virtual impedance can be used to reduce fault current [38]. If the voltage is closed-loop controlled through double loop with inner current loop, current reference limits are set to keep the output current within the safety limits. As shown in Figure 4-16, the control can successfully reduce the fault current.

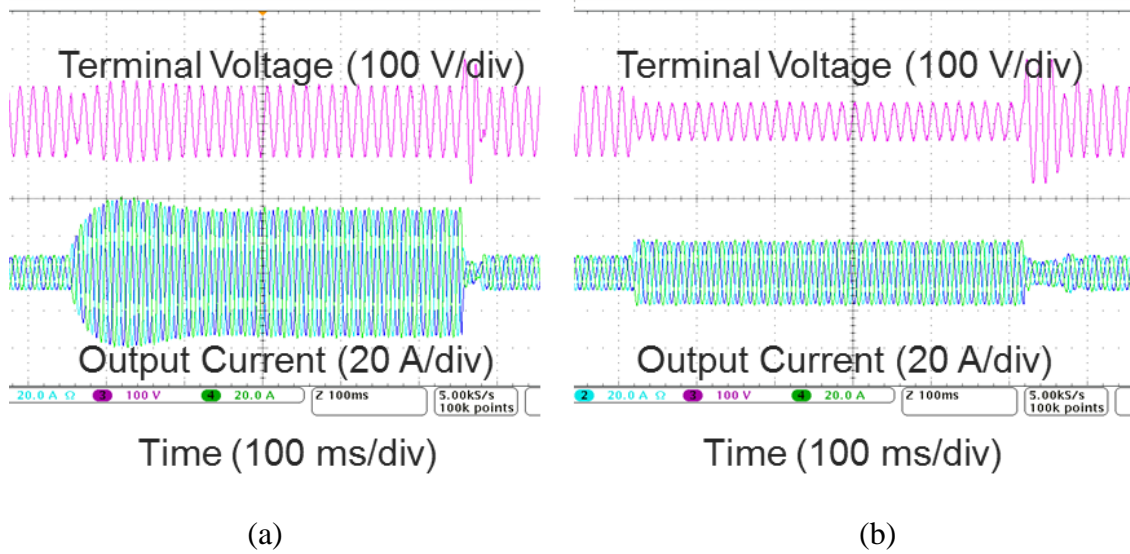


Figure 4-16. Fault operation experimental results showing FCWT terminal voltage and output current. (a) without current limits, (b) with current limits [139].

4.4 Conclusion

VSG control allows the renewable energy sources to behave like the traditional SG to operate in the power system. However, the energy balance of the generation system is not well discussed in the previous literature. This chapter develops the VSG control for FCWTs, with the consideration of a short term minute-level energy storage integrated on the dc link:

- GSC performs the VSG control, with power limitations for the extreme conditions.
- SSC regulates the dc link voltage and provides a buffer for the power generation and grid interfacing control.
- The power balance is maintained by turbine speed control though MSC, according to the *SoC* of the storage.

With the proposed VSG control, FCWTs can display the same output behavior as a conventional SG. This allows FCWTs to:

- Be able to operate in both grid-connected and stand-alone conditions, allowing non-MPPT operation of the wind turbine according to load or dispatch command by the system operators, while providing grid support functions;
- Be able to identify when it is already at the maximum available power, and limit the output power in VSG MPPT control mode to avoid deep discharging of the energy storage, while still exhibiting SG dynamic behavior.

The schemes for power limiting and the identification of the operating conditions are proposed, and the energy capacity required for the energy storage is discussed in this chapter.

The experiments are conducted in a power electronics based power system emulation platform; results demonstrate the feasibility and effectiveness of the control.

5 Short Circuit Fault Emulation in HTB Testing Environment

As a fault mode in electric power systems, short circuit faults create voltage sags and over-currents, which cause excessive stresses on power devices and sometimes lead to cascading failures. As a result, the critical clearing time (CCT) of a short circuit fault can be used to assess the severity of a contingency, and the transient stability of a power system [153]. The fault responses of various devices have also become an important performance and robustness indicator. Grid codes from different countries require the fault ride through capabilities for grid connected generation units [99, 122].

To enhance the testing capability of the HTB, a short circuit fault emulator has been developed in this chapter. The operation principle and detailed control strategy are presented. Simulation and experimental results are also given to demonstrate the feasibility of the emulator [79].

5.1 Operating Principle and Hardware Requirement for the Fault Emulator Converter

Similar to the configuration in Figure 2-14(d) which uses a shunt connected impedance, the proposed method uses a shunt connected VSC to generate the short circuit event. As shown in Figure 5-1, the fault emulator converter is directly connected to the fault location F. In the normal operation, all the switching devices in the VSC are blocked, so that there is no current flowing through the fault location. The EUT and other parts of the system work in the steady state. When the fault is triggered, the VSC starts to generate PWM voltage and control the voltage of the fault location as if the shunt impedances were connected.

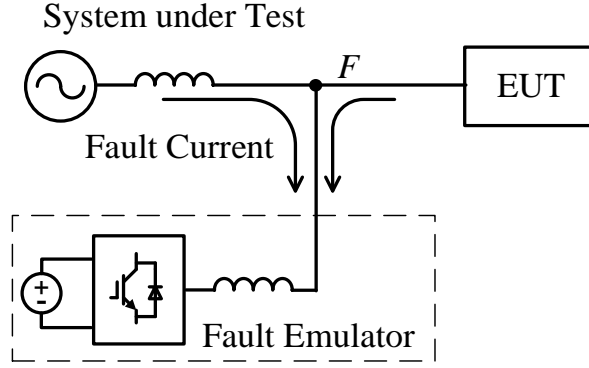


Figure 5-1. Schematics of the shunt connected fault emulator converter [79].

Figure 5-2 shows the equivalent circuit of the fault emulation converter. The outside circuits including the EUT and other part of the system can be considered as a Thevenin equivalent voltage source, E_{Thev} , and an equivalent impedance, Z_{Thev} . The filter of the fault emulator is represented as impedance Z_{fil} , and the voltage and current at the fault locations are V_F and I_F respectively. The fault emulator converter terminal voltage is its duty ratio d times half of the dc link voltage V_{dc} .

Different short circuit events can be emulated by the fault emulator, including single-line-to-ground, double-line-to-ground, line-to-line, and three-phase fault. The fault currents caused by short circuits may be several times larger than the normal operating currents and are determined by the system impedance between the generator (or other source) voltages and the fault. Since all fault currents flow through the VSC, components with a sufficient power rating must be chosen to conduct the fault current, and the dc link of the emulator converter should be able to absorb active power. In addition, the dc voltage of the emulator VSC should be high enough to ensure it does not behave as a diode rectifier during normal operation.

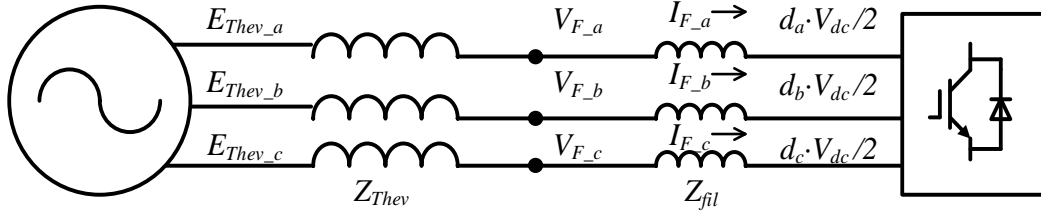


Figure 5-2. Equivalent circuit of the fault emulator converter.

Since the fault emulation is achieved by controlling the voltage and current at the fault locations, the voltage and current sensors should be placed at the fault location F in Figure 5-1 as the feedback to the VSC controller. Line-to-line voltage measurement is enough for the line-to-line and three-phase faults, but for the cases of single and double line-to-ground faults, phase-to-ground voltages have to be measured. The detailed algorithms for the fault voltage and current control will be discussed in the next section.

5.2 Control Strategies for the Fault Emulator Converter

5.2.1 Single-line-to-ground Fault

Since the three phases can be similarly represented, phase a to ground fault is chosen as an example in the following discussion. The constraint equation is:

$$\begin{cases} V_{F_a} = Z_{emu_a} \cdot I_{F_a} \\ I_{F_b} = 0 \\ I_{F_c} = 0 \end{cases} \quad)$$

where Z_{emu_a} is the emulated grounding impedance (impedance between phase a and ground).

Figure 5-3 shows the control block diagram of the fault emulator for single-line-to-ground fault. The reference voltage $V_{F_a}^*$ is calculated by the measured current and impedance value, and the duty ratio of the phase a switches d_a can be obtained through a PI controller. If zero impedance short circuit is emulated, 0 is given as the voltage reference. During the fault period, the switches of phase b and c are blocked, so the current can only flow in phase a .

The control block diagram with the electrical model is given in Figure 5-4. The left part is the controller, which includes a PI regulator, a control delay block z^{-1} , current and voltage measurement low pass filters LPF_V and LPF_I , and the emulated grounding impedance Z_{emu} . The output to the electrical model is the duty ratio d . Through VSC model, and external impedance model, the voltage and current at the fault location V_F and I_F can be obtained. In this case, V_F is phase voltage V_a , and I_F is phase current I_a .

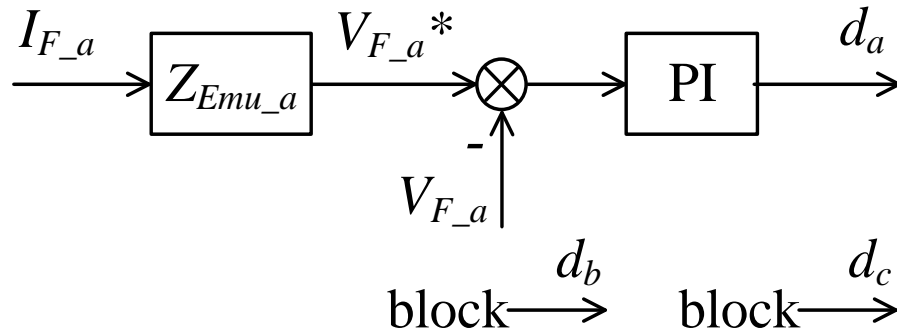


Figure 5-3. Control block diagram of single-line-to-ground fault for phase a [79].

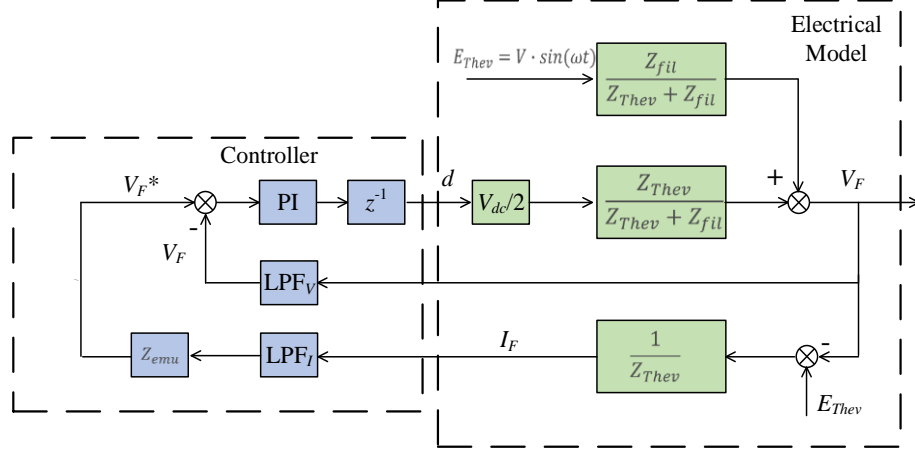


Figure 5-4. Single phase control block diagram with electrical model in abc axis.

5.2.2 Double-line-to-ground Fault

Similar to the single-line-to-ground fault, the constraint equation is:

$$\begin{cases} V_{Fa} = Z_{emu_a} \cdot I_{Fa} \\ V_{Fb} = Z_{emu_b} \cdot I_{Fb} \\ I_c = 0 \end{cases}$$

Since the equivalent circuit of the two phases are identical to each other, the controller design can be derived directly from the single-line-to-ground case. The control diagram of phase a and b to ground is shown in Figure 5-5. The VSC controls the voltage of the phase a and b in accordance with the grounding current, while phase c is blocked with no current. Similarly, the model for each phase is the same as Figure 5-4.

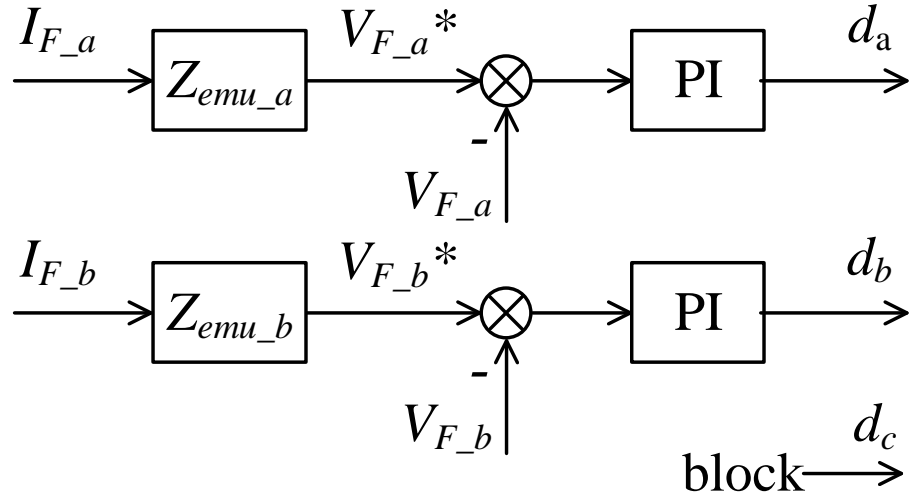


Figure 5-5. Control block diagram of double-line-to-ground fault for phase a and phase b [79].

5.2.3 Line-to-line Fault

The constraint equation of phase a to phase b short circuit is:

$$\begin{cases} I_{F_a} + I_{F_b} = 0 \\ V_{F_a} - V_{F_b} = V_{F_{ab}} = Z_{emu_{ab}} \cdot I_{F_a} \\ I_{F_c} = 0 \end{cases}$$

where $Z_{emu_{ab}}$ is the emulated impedance between the phases. According to the equivalent circuit in Figure 5-2, the relationship of the fault current can be derived as:

$$I_{F_a} + I_{F_b} = \frac{(E_{thev_a} + E_{thev_b}) - (d_a + d_b) \frac{V_{dc}}{2}}{Z_{thev} + Z_{fil}}$$

Thus, the fault current can be regulated by controlling the sum of the duty ratio from both phases, note as common mode duty ratio d_{cm} . On the other hand, the fault voltage is the difference

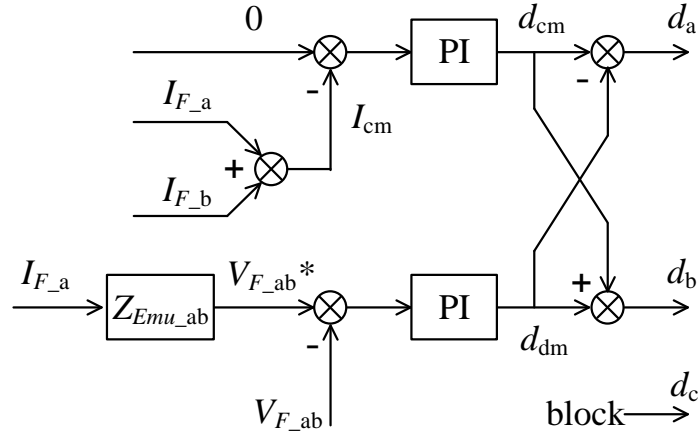


Figure 5-6. Control block diagram of line-to-line fault for phase a and b [79].

of the voltage between phase a and b , and it can be regulated by the difference of the duty ratio from both phases, note as differential mode duty ratio d_{dm} . Voltage and current of the fault emulator converter can be controlled independently, and the control diagram of the line-to-line fault is shown in Figure 5-6.

The modeling and analysis of the voltage and current control loops can also be done independently. The current closed-loop model is shown in Figure 5-7, while the voltage closed-loop model is the same as Figure 5-4.

5.2.4 Three-phase Short Circuit Fault

The three-phase short circuit fault is the most severe condition, and usually there is no impedance between shorted phases. Since it is a balanced condition with no zero sequence voltage, the boundary equation is:

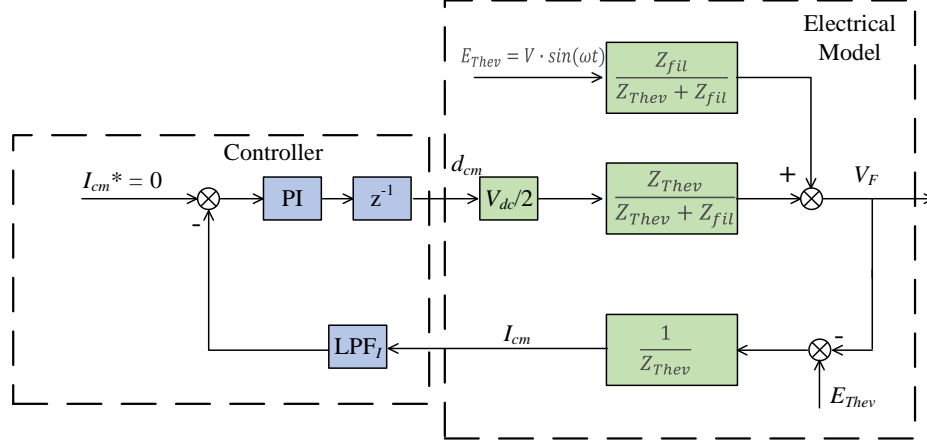


Figure 5-7. Current control block diagram for line-to-line fault with electrical model in abc axis.

$$V_{F_a} = V_{F_b} = V_{F_c} = 0$$

Due to the balanced nature of the case, the corresponding control can be conducted in dq axis, as shown in Figure 5-8, where V_{F_d} , V_{F_q} , I_{F_d} , I_{F_q} indicate the voltage and current measurements in dq axis. For more general cases, fault impedance between shorted phases can also be emulated. Since the control loop model has already been well established [33, 56, 57], it will not be discussed in this chapter.

5.3 Hardware Based Testing Platform and Corresponding Controller Design

The experiment topology is the HTB two-area system shown in Figure 2-3(a) [49]. The system parameters and base values are rescaled to allow the fault current, as shown in Table 5-1.

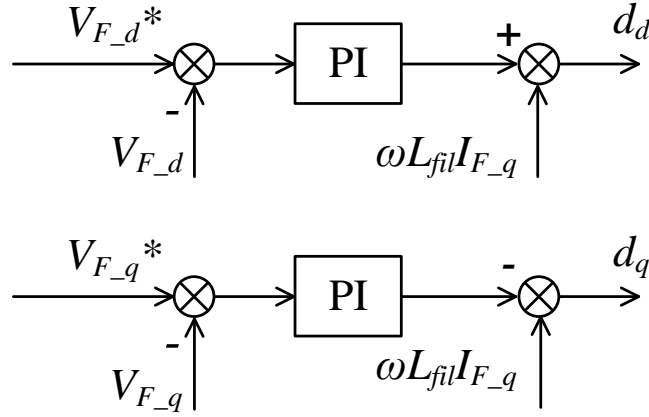


Figure 5-8. Control block diagram of three-phase fault control in dq axis. [79]

5.3.1 Control Parameter Design

Based on the parameters of the testing platform, inductive impedances are dominant for the Thevenin equivalent circuit. Assuming fault location is at bus 9, Thevenin inductance is in the range of 1.5 mH to 10 mH depending on the connection of the generators.

For single-line-to-ground, double-line-to-ground, and line-to-line faults, the voltage closed loop controller models are the same, hence the controller design would be the same. Figure 5-9 shows the open loop bode plot of V_F/V_F^* , and the designed parameters are shown in Table 5-2, the control loops are stable with around 100 Hz bandwidths. Figure 5-10 shows the closed loop bode plot of V_F/E_{Thev} . The higher Thevenin impedance Z_{Thev} , the better control performances the control allows. At 60 Hz line frequency, the attenuation is lower than -23dB, which means the controlled fault voltage amplitude V_F can be reduced to at most 10% of the pre-fault line voltage.

Table 5-1. Parameter Setting of the Experimental Platform

Name	Value	Name	Value
L1-6	2.5 mH	System voltage base	68.6 V
L2-6	0.7 mH	System power base	1633 VA
L6-7	0.7 mH	System frequency base	60 Hz
L7-9	7.6 mH	Converter sw. freq.	10 kHz
L3-10	2.5 mH	G1/G3 inertia constant	6.5 s
L4-10	0.7 mH	G2/G4 inertia constant	6.175 s
L9-10	0.7 mH		

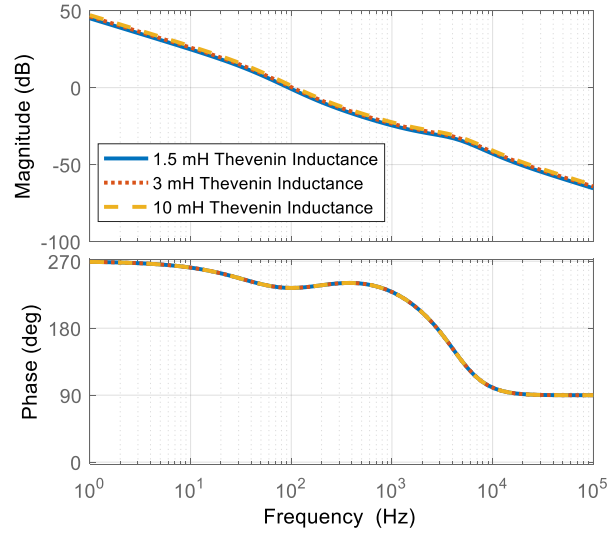


Figure 5-9. Bode plot of open loop transfer function of V_F/V_F^* in *abc* axis for single-line-to-ground, double-line-to-ground and line-to-line fault emulations.

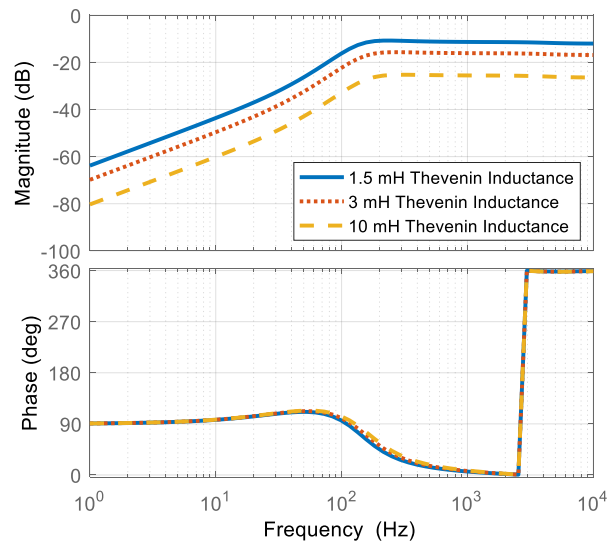


Figure 5-10. Bode plot of closed loop transfer function of V_F/E_{Thev} in *abc* axis for single-line-to-ground, double-line-to-ground and line-to-line fault emulations.

The current control loop of line-to-line fault emulation can be designed similarly for a bandwidth higher than 100 Hz, given Thevenin inductance between 1.5 mH to 10 mH. The open loop bode plot of I_F/V_F^* is given in Figure 5-11, and the corresponding controller parameters are in Table 5-2. The closed loop bode plot of I_F/E_{Thev} is given in Figure 5-12. With higher than -70 dB attenuation, the current difference between phases can be controlled to zero regardless of the fault voltages.

For three-phase-faults, the terminal voltage is controlled in dq axis, thus the fundamental frequency component can be controlled to zero without steady-state errors. The control parameters are shown in Table 5-2, based on the previous control parameter design method [33, 56, 57].

5.3.2 Discussion

From previous analysis, the proposed short circuit emulator and the corresponding control strategies perform well with higher Thevenin impedance of external circuit. For example, the inaccuracy of the voltage control in abc domain will rise to 50%, when the Thevenin impedance reduces to 0.4 mH. This is because when the filter impedance dominates the Thevenin impedance, the magnitude of $\frac{Z_{fil}}{Z_{Thev}+Z_{fil}}$ will be closer to 1, and V_F will be more susceptible to the disturbance of E_{Thev} .

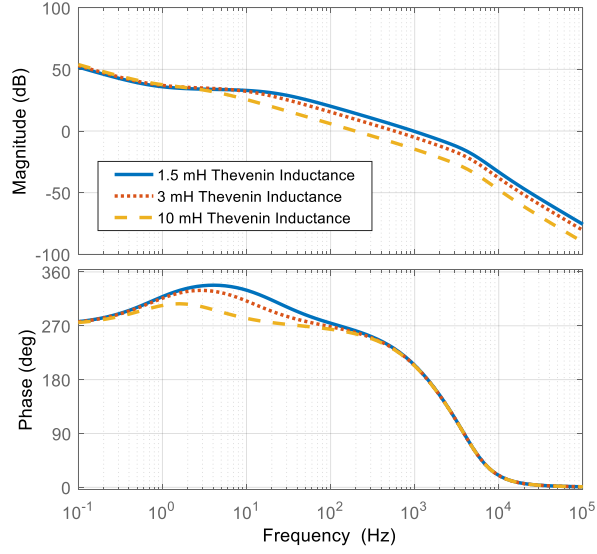


Figure 5-11. Bode plot of open loop transfer function of I_F/V_F^* in abc axis for line-to-line fault emulation.

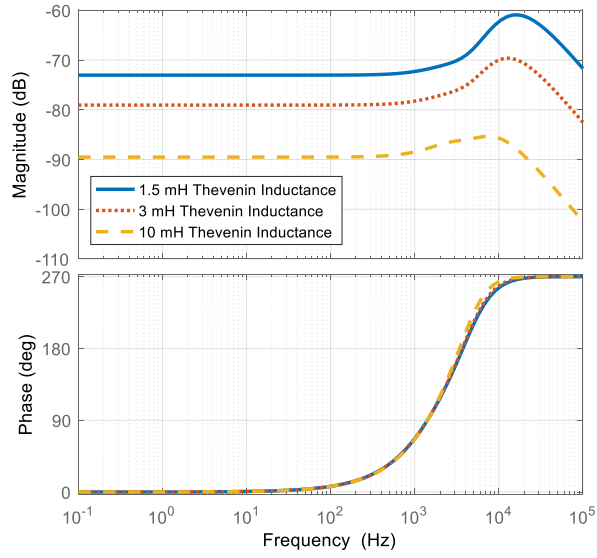


Figure 5-12. Bode plot of closed loop transfer function of I_F/E_{Thev} in abc axis for line-to-line fault emulation.

Table 5-2. Controller Parameters for Short Circuit Fault Emulators

Fault Type	Parameter Name	Value
General	Voltage measurement LPF cut-off frequency	300 Hz
	Current measurement LPF cut-off frequency	1000 Hz
Single-line-to-ground	Proportion regulator Kp	0.023
	Integration regulator Ki	23
Double-line-to-ground	Proportion regulator Kp	0.023
	Integration regulator Ki	23
Line-to-line	Voltage loop proportion regulator Kp	0.023
	Voltage loop integration regulator Ki	23
	Current loop proportion regulator Kp	0.8
	Current loop integration regulator Ki	4
Three-phase	Proportion regulator Kp	0.016
	Integration regulator Ki	5

To address this issue, one way is to reduce the filter inductance, or add a capacitor to allow more decoupling of the Thevenin source and the short circuit fault emulator. The control parameters will be adjusted accordingly. The other way is to introduce a current feed-forward compensation to the control loops shown in Figure 5-8, as introduced in [33].

5.4 Experimental Results

5.4.1 Verification of Proposed Short Circuit Emulator

In order to demonstrate the control performances of the proposed short circuit emulator, only two converters in the hardware testing platform are used: the converter emulator at bus 3 is controlled as open loop voltage source to generate the three-phase voltage, and the converter emulator at the location of L9 is configured as the fault emulator.

Figure 5-13 and Figure 5-14 show the voltages and currents of single-line-to-ground fault with $1\ \Omega$ grounding impedance with pure resistive and pure inductive respectively. The currents and voltages have the same amplitudes. In the resistive case, the current and voltage are in phase; while in the inductive case, the phase difference is 90° .

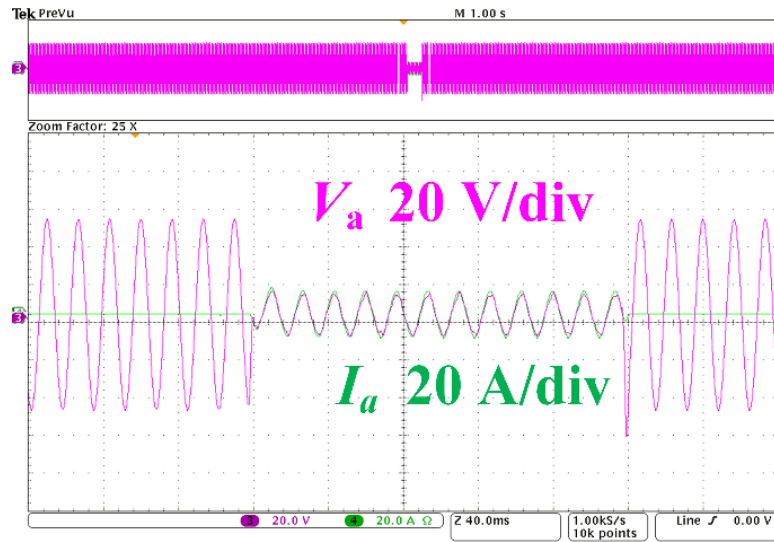


Figure 5-13. Experimental results of single-line-to-ground short circuit with 1 Ω grounding resistance [79].

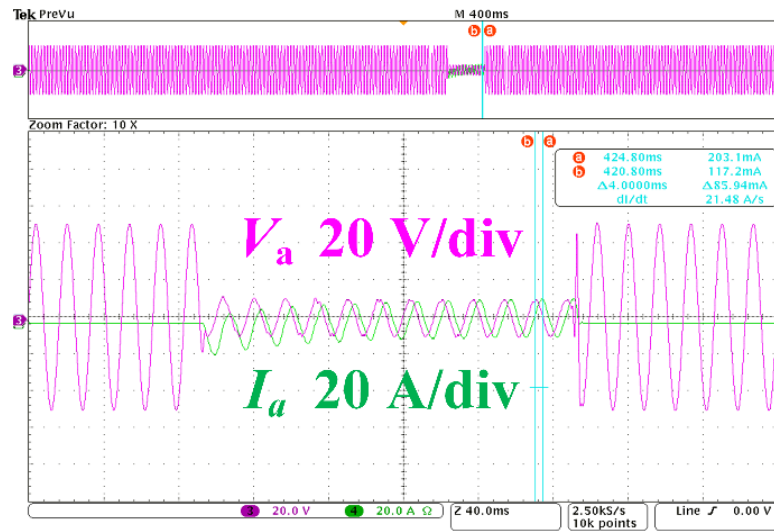


Figure 5-14. Experimental results of single-line-to-ground short circuit with 1 Ω pure inductive grounding impedance [79].

Figure 5-15 gives the results of the double-line-to-ground fault with no grounding impedances. The amplitude difference is caused by the inductance difference between the phases. Figure 5-16 gives the results of the line-to-line short circuit scenario with no fault impedance. As discussed in the control design section, the control conducted in abc axis is subjected to the disturbance with the grid voltage disturbance E_{thev} . The emulated fault voltage in the experimental result is less than 10% of the pre-fault voltage, as expected.

Figure 5-17 and Figure 5-18 show the voltages and currents at the fault location for the three-phase short circuit. Results show that the voltage controller of the fault emulator can control the voltage to zero.

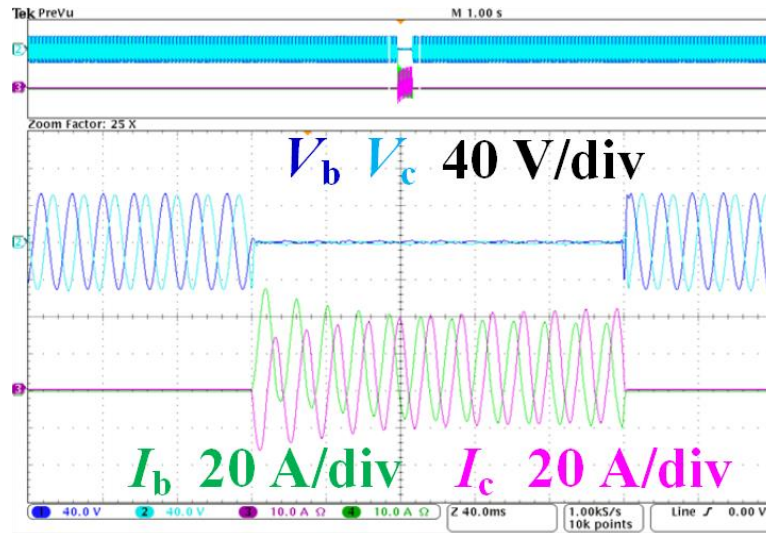


Figure 5-15. Experimental results of double-line-to-ground short circuit [79].

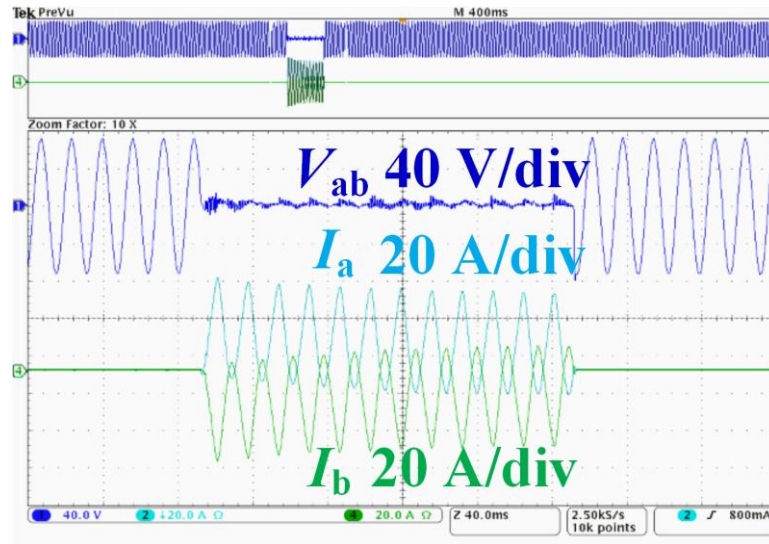


Figure 5-16. Experimental results of line-to-line short circuit [79].

a

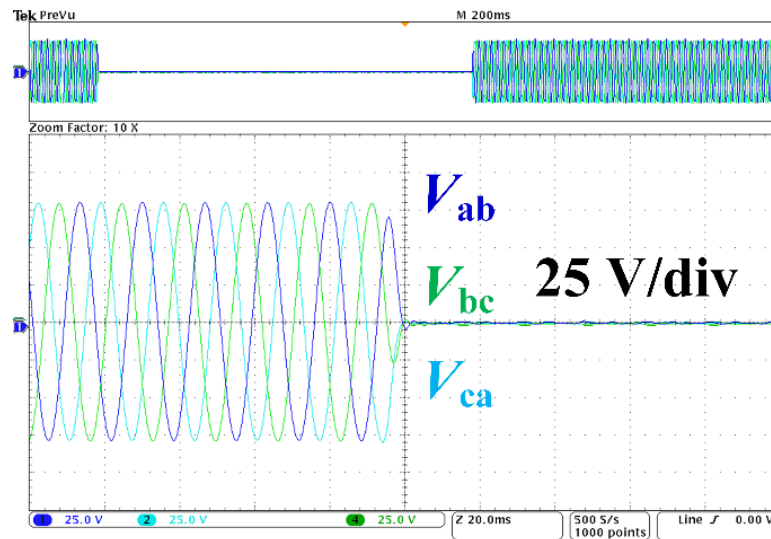


Figure 5-17. Experimental measurement of voltages for three-phase short circuit [79].

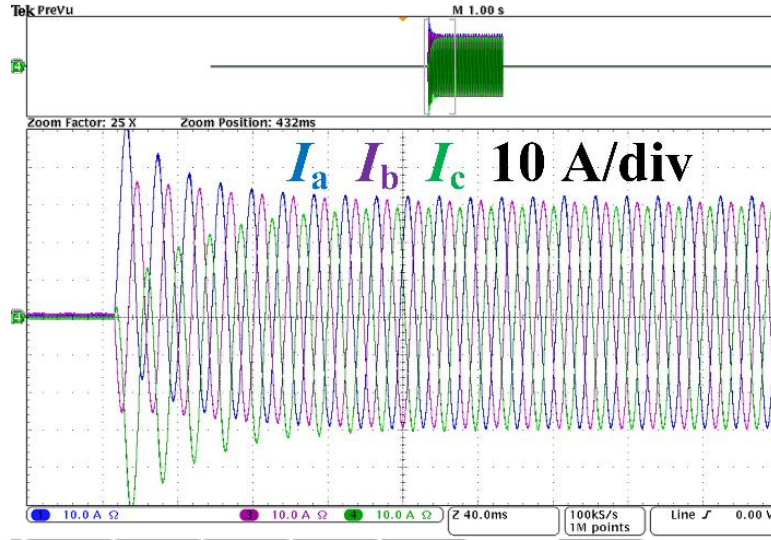


Figure 5-18. Experimental measurement of currents for three-phase short circuit [79].

5.4.2 Application to Determine Critical Clearing Time

Compared with previous fault emulators mentioned in the literature, one advantage of the proposed method is that it can flexibly create different faults to investigate the impact of a short circuit fault to a system with multiple components, rather than a single equipment.

To demonstrate this unique capability, the proposed fault emulator is then integrated with the load emulator at bus 7 in the two-area system shown in Figure 2-3(a). All four generator emulators have 0.7 p.u. active power output, and load active power consumptions are 1.8 p.u. and 1.0 p.u. at bus 7 and 9 respectively. A series of three phase short circuit faults are activated by the emulator at bus 9 with different fault clearing times. Inter-area oscillations are then triggered between Area 1 and Area 2, causing the output power and frequency to fluctuate.

The system variables are extracted with a step time of 0.01 s. The frequencies of the generators are given as an example to demonstrate the oscillation, as shown in Figure 5-19. A longer clearing

time causes larger oscillation transient. At around 120 s in the figure, with 0.32 s fault clearing time, the oscillation is significantly larger than the previous ones, and the system takes much longer to restore to normal operation. This is due to the power swing after the power system disturbance is too large, and the generators at different areas lose synchronization, identified as out-of-step. Thus, the CCT of the system for transient stability is 0.32 s.

Figure 5-20 shows the oscilloscope measurements of the test sequence. When fault is applied, the voltage at bus 7 is controlled to be zero, and the voltage at all other locations are reduced. The fault current is supplied by the generators. The system oscillation can also be observed.

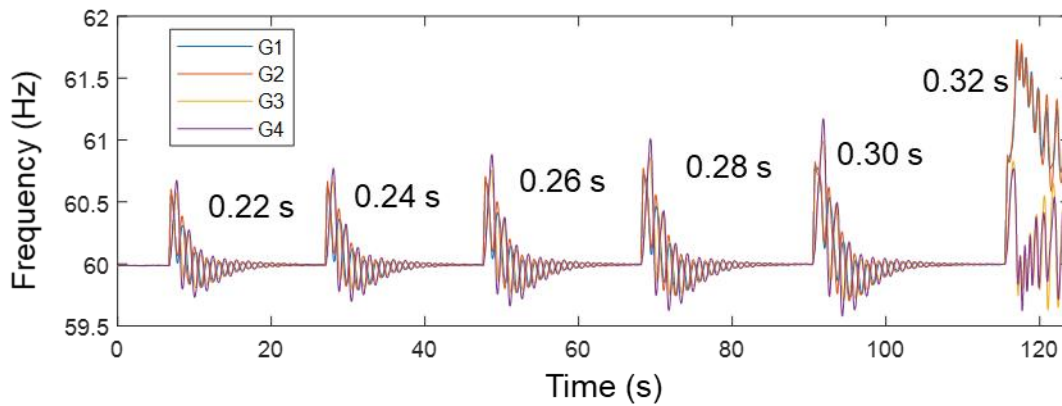


Figure 5-19. Experimental results of a series three-phase short circuit fault at two-area system to determine the critical clearing time.

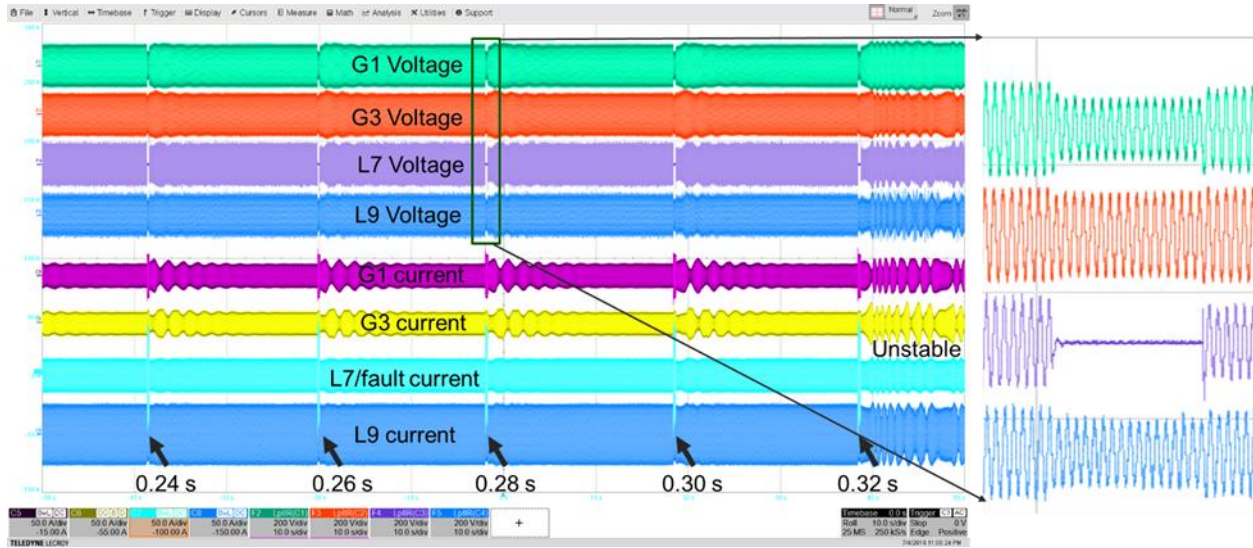


Figure 5-20. Oscilloscope measurements of a series three-phase short circuit fault at two-area system to determine the critical clearing time.

The experimental configuration in the hardware test platform with the proposed fault emulator is then reproduced in the MATLAB/Simulink, with simulated three phase short circuit fault in the circuit at the same location. The simulated output powers and frequencies are shown in Figure 5-21 and Figure 5-22, and zoomed-in waveform of the experimental results are presented side-by-side for comparison.

For the same fault clearing time, the simulated power and frequency have around the same magnitude and damping ratio as the experimental results. And they both have significantly larger transients for the case of 0.32 s clearing time. The out-of-step status could be further verified by the angle difference results shown in Figure 5-23. The 0.32 s result did not go back to the original value after the transient.

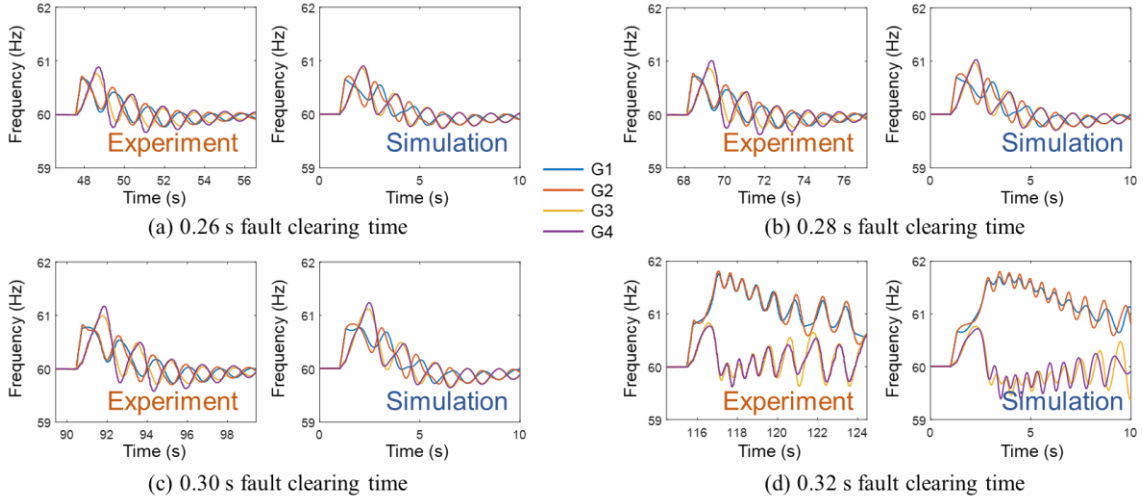


Figure 5-21. Simulated generator frequencies in cases of three-phase short circuit faults with different fault clearing time, in comparison with experimental results.

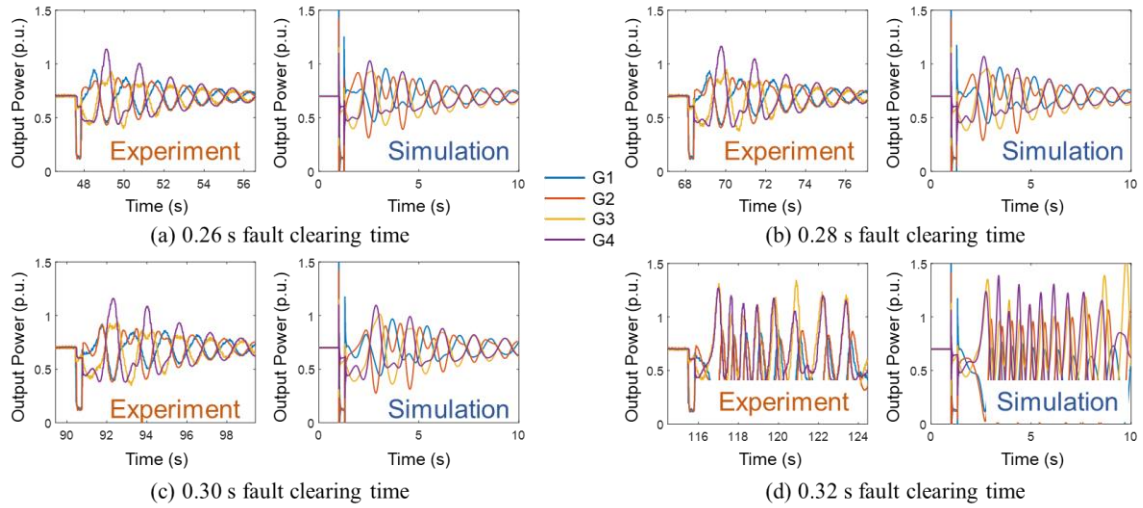


Figure 5-22. Simulated generator output powers in cases of three-phase short circuit faults with different fault clearing time, in comparison with experimental results.

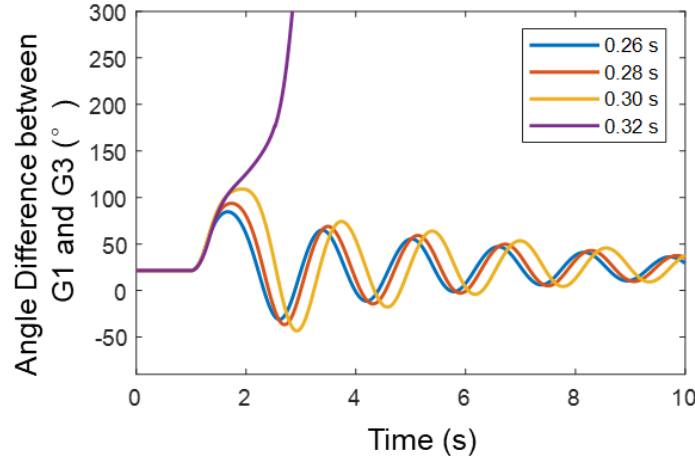


Figure 5-23. Simulated angle differences between G1 and G3, in cases of three-phase short circuit faults with different fault clearing time.

5.5 Conclusion

This chapter proposes a method to emulate four basic types of short circuit fault by using a shunt connected converter. The fault emulator can achieve the same voltage and current boundary condition as the short circuit faults, and essentially has the same impact to the system under tests.

The hardware requirements and limitation of the converter are presented. The control strategies of the fault emulator converter and the design considerations are discussed. Experimental results have shown the feasibility of the method. An example of using it to determine the critical clearing time of a system is presented to demonstrate its unique capability than previous technologies.

Compared with the solutions shown in Figure 2-14, the proposed shunt connected VSC is more flexible than (a) generator, (b) transformer, and (d) shunt impedance solutions, but the

disadvantage is that it still requires high rating converters to conduct the fault current. Unlike the (c) series connected VSC method, the proposed shunt connected VSC focuses on reproducing the short circuit event. It cannot reproduce the cases like harmonics or voltage swells without modeling of other components in the system like generators or non-linear loads, but it can help to investigate the system impact of various short circuit faults with ease.

6 Enhancing Power System Transient Stability by VSG Control Using Wide-area Measurements

In Chapter 4, the basic operation of VSG controlled FCWT has been developed, and controls have been implemented to limit the output current during voltage sags. In Chapter 5, a short circuit fault emulator was developed in the HTB to create disturbance for system transient stability studies. This chapter continues the research work on the fault operation of VSG controlled FCWT to improve the system transient stability without considering current limits, and next chapter will focus on the impact of limited current.

6.1 Previous VSG Control Method to Improve System Stability

As surveyed in Chapter 2, one benefit of the VSG control is that the parameters of the VSG and its traditional SG counterpart do not need to be the exactly same all the time. With the flexibility of the power electronics control, the exhibited impedance or inertia may adaptively change during grid disturbances, to achieve better system stability performance.

Previous literature has suggested to increase the VSG inertia when the output frequency is moving away from the nominal value; and decrease it when the output frequency is returning to the nominal value [123-127]. The basic idea is shown in Figure 6-1 and Table 6-1, where J is the emulated moment of inertia of the SG, f is the output frequency of the VSG, and f_n is its nominal value (50 or 60 Hz). This way, the system frequency is harder to deviate, but easier to recover. Better system damping is thus achieved. The design of the adaptively changed VSG parameters has also been discussed in [124, 125].

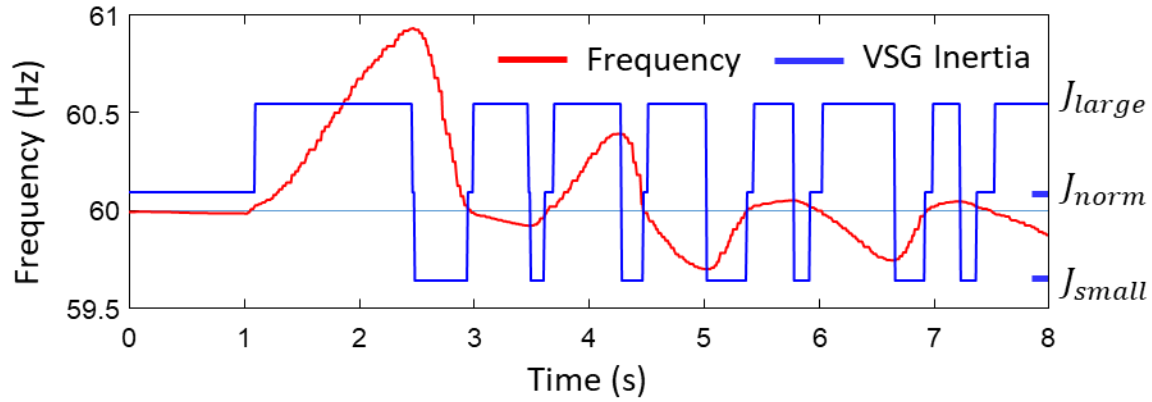


Figure 6-1. Adaptive frequency changing method during transient to minimize frequency disturbance.

Table 6-1. Truth Table of Adaptive Inertia VSG Control

$\frac{df}{dt} > 0$	$f - f_n > 0$	Operating Conditions	Inertia Value Selection	Anticipated Result
T	T	Accelerating, Faster than f_n	J_{large}	Harder to move away from f_n
T	F	Accelerating, Slower than f_n	J_{small}	Easier to return to f_n
F	T	Decelerating, Faster than f_n	J_{small}	Easier to return to f_n
F	F	Decelerating, Slower than f_n	J_{large}	Harder to move away from f_n

However, these methods do not guarantee the benefits to the system transient stability, where the first or first several swings of rotor angle oscillation are of the most significance. Especially on a more complex system when multiple generation units are present, and system faults may occur at any location, these methods may have detrimental effect depending on specific scenarios.

6.2 Limitation Previous Methods and Proposed Control

To demonstrate the limitation of previous adaptive inertia methods, a test case based on Kundur's two area system is selected. The system topology is shown in Figure 2-3(a). In the test system, G1 and G3 are traditional SG, without the capability to change its physical moment of inertia, while G2 and G4 are replaced with renewable sources controlled as VSG of the identical capacities. In this demonstration, all four generation sources have the same output power, while the load L7 has larger power consumption than the load L9, and thus the active power is transferring from bus 9 to bus 7. Two possible short circuit fault locations are assumed at load bus 7 or load bus 9.

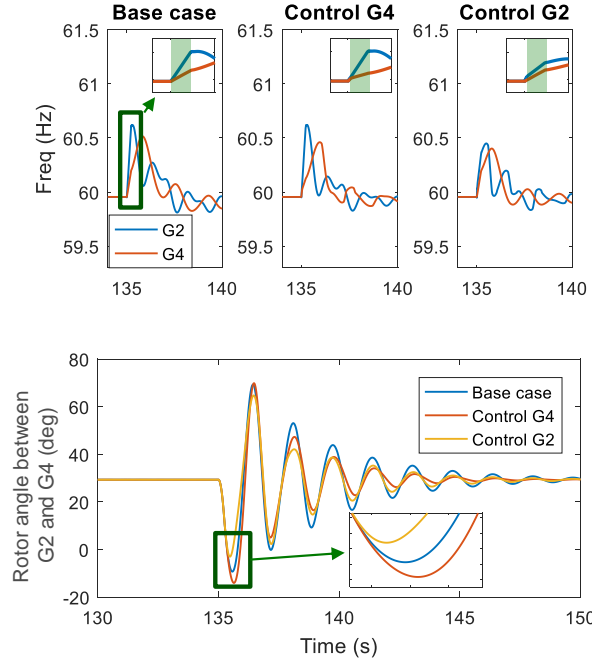
The emulated VSG inertia of G2 and G4 follows the simplest hysteresis scheme in [123], as described in in Table 6-1. But the concept shown in this demonstration would apply to other more complex methods. From the truth table, emulated moment of inertia value can be expressed as:

$$J = \begin{cases} J_{large} & (f - f_n) \frac{df}{dt} > 0 \\ J_{small} & (f - f_n) \frac{df}{dt} < 0 \end{cases} \quad (6-1)$$

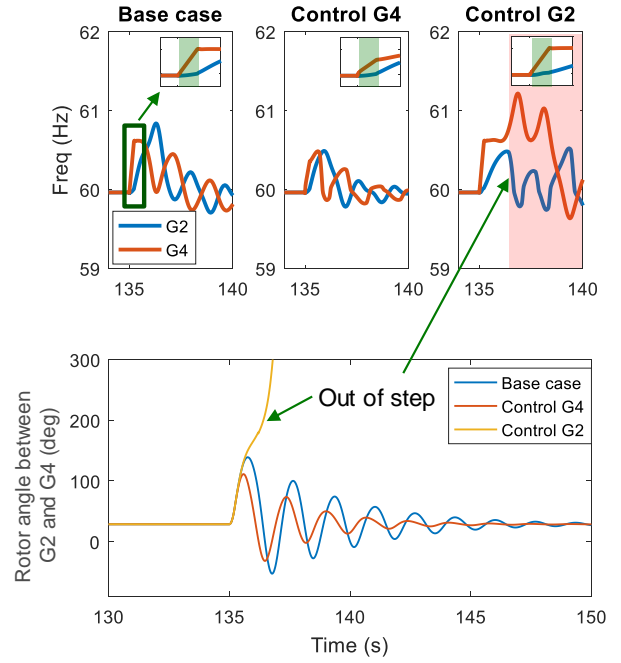
For each fault location, three cases are simulated. ① Base case is when both VSG operate normally with constant inertia. ② Control G4 case is when the adaptive inertia control is applied

to G4, and G2 has constant inertia. ③ Control G2 case is when the adaptive inertia control is applied to G2, and G4 has constant inertia. Figure 6-2(a) shows the results when the fault occurs at load bus 7, and Figure 6-2(b) shows the results when the fault occurs at load bus 9.

Figure 6-2(a) shows that both Control G4 and Control G2 cases have better system damping than the base case, in terms of the rotor angle difference between G2 and G4. This matches with the analysis with existing literature. The difference is the amplitude of the first swing: Control G4 case has slightly larger peak, and Control G2 has slightly lower peak than the base case. This is due to the limitation of the adaptive inertia control scheme. From the zoomed-in figure of the frequency chart, the green shaded area indicates the period when fault occurs. Due to the low voltages in the system, the frequencies of all SGs and VSGs increase. But G1 and G2 accelerate faster than G3 and G4, because the fault is closer to them. Thus, if G4 increases its inertia during the transient, its frequency ramp rate becomes lower. Frequency difference between G2 and G4 is larger, and hence the angle difference is larger. Vice versa, with the Control G2 case, smaller frequency difference yields smaller angle difference.



(a) Fault location at load bus 7



(b) Fault location at load bus 9

Figure 6-2. Simulation results comparison of applying adaptive inertia control of VSG with different fault location.

The difference may have relatively minor impact when the fault is at load bus 7, but not when fault is at load bus 9. In Figure 6-2(b), if the angle difference is large enough to be unstable, the SGs and VSGs are out of step, shown as the red shaded area. This indicates that this inappropriate adaptive inertia control may reduce the critical clearing time (CCT) of the fault, and system out of step protection has less reaction time to prevent it.

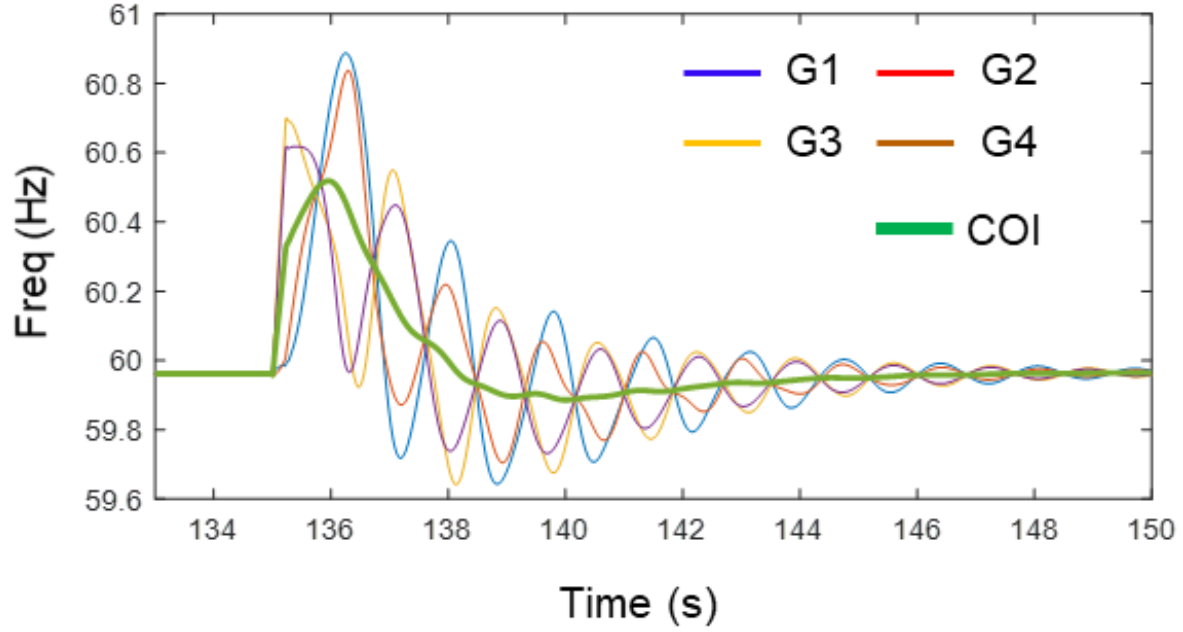


Figure 6-3. System frequency after load bus 9 fault.

Figure 6-3 shows the system frequency response after a short circuit fault at load bus 9. All generation units are oscillating against each other, revolving around the center of inertia (COI) frequency, f_{COI} defined as:

$$f_{COI} = \frac{\sum J \cdot f}{\sum J} \quad (6-2)$$

where J is the moment of inertia value of each generation unit, and f is their output frequency.

The COI frequency is calculated as the weighted average of the system frequency. It can be considered as an index to monitor the dynamics of an individual unit with respect to the general trend of the overall system. At steady-state, the settling frequency of all parts of the system will be the same as the COI frequency, which will not be exactly as its nominal value.

Thus, it is intuitive to improve the existing adaptive inertia VSG methods by using the COI frequency. By knowing whether other parts of the system are faster than itself or not, the individual VSG may decide to catch-up with the COI frequency faster using a smaller inertia value, or resist deviating from the COI frequency using a larger inertia value. The adaptive inertia criterion in (6-1) is modified as:

$$J = \begin{cases} J_{large} & (f - f_{COI}) \frac{df}{dt} > 0 \\ J_{small} & (f - f_{COI}) \frac{df}{dt} < 0 \end{cases} \quad (6-1)$$

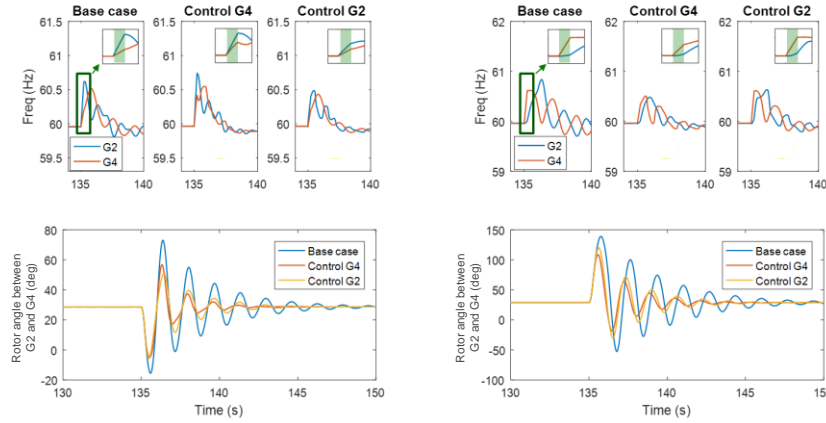
Figure 6-4 shows the simulation results using the improved method with the same three cases as the results in Figure 6-2. For faults at both locations, the proposed control always tries to reduce the frequency differences between VSG and the other generation units. All controlled cases have better performance than the base cases, demonstrating the effectiveness of the proposed method.

6.3 Experiment Implementation and Test Results

6.3.1 Experimental platform

The previous simulation results only showed that the proposed method may enhance the power system transient stability using an adaptive inertia scheme with the system COI frequency information. But there are still many other considerations in practical implementation. In this section, experimental implementation and test results are given to validate the proposed control.

The experiments are conducted in the HTB with two-area system configuration developed in Chapter 5, and the parameters are shown in Table 5-1. In the test cases, all four generation units



(a) Fault location at load bus 7

(b) Fault location at load bus 9

Figure 6-4. Simulation results of applying improved adaptive inertia control of VSG with different fault location.

have the same 0.7 p.u. active power output, while load consumption at L7 and L9 has two configurations. Table 6-2 shows the CCT for four test cases, with all four generation units using traditional SGs as the base case. Since Case 1 and Case 4 have much longer CCT, the system will be much less likely to have transient stability issue.

6.3.2 Implementation of Proposed Control

A LabVIEW based central controller is used to monitor, record data from, and issue commands to the system components. In practice, the proposed control uses wide-area measurements to calculate the COI frequency. It is inevitable to have time delay for the real-time control, while Figure 6-4 showed the simulation results when there is unrealistically no delay. In

Table 6-2. Base case configuration and CCT

Case 1	Value	Case 2	Value
L7	1.8 p.u.	L7	1.8 p.u.
L9	1.0 p.u.	L9	1.0 p.u.
Fault Location	L7	Fault Location	L9
CCT	0.54 s	CCT	0.30 s
Case 3	Value	Case 4	Value
L7	1.0 p.u.	L7	1.0 p.u.
L9	1.8 p.u.	L9	1.8 p.u.
Fault Location	L7	Fault Location	L9
CCT	0.30 s	CCT	0.54 s

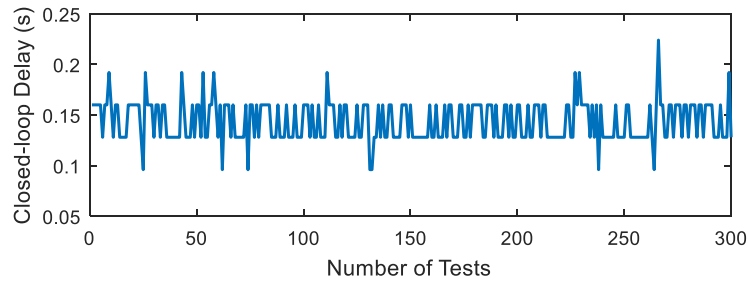


Figure 6-5. Measured time-delay.

experiments, the frequencies of all four generators are collected by the central controller, and the COI frequency is calculated and sent to the VSG unit. The measured time-delay for the experimental platform is shown in Figure 6-5. Artificial delay can be added to the central controller to investigate its impact as demonstrated in the next section.

In addition, a dead-band is added to reduce the impact of measurement errors:

$$J = \begin{cases} J_{large} & f - f_{COI} > f_{th}, \frac{df}{dt} > ROCOF_{th} \\ J_{large} & f - f_{COI} < -f_{th}, \frac{df}{dt} < -ROCOF_{th} \\ J_{small} & f - f_{COI} > f_{th}, \frac{df}{dt} < -ROCOF_{th} \\ J_{small} & f - f_{COI} < -f_{th}, \frac{df}{dt} > ROCOF_{th} \\ J_{norm} & |f - f_{COI}| < f_{th}, \left| \frac{df}{dt} \right| < ROCOF_{th} \end{cases} \quad (6-2)$$

where f_{th} is the threshold for frequency deviation, and $ROCOF_{th}$ is the threshold for rate of change of frequency. The thresholds are positive. In the following experiments, J_{large} is two times of its original value J_{norm} (6.175 s for G4), J_{small} is half of J_{norm} , f_{th} is 0.02 Hz, and $ROCOF_{th}$ is 0.01 Hz/s. These parameters can be better designed according to the specific system configuration and utility requirements

6.3.3 Experimental Results

In the tests, G4 is changed to a VSG unit, with different control methods applied to study their impact. Table 6-3 shows the measured CCT for the test cases. Previous literature method using f_n as criterion may be beneficial or detrimental to the system transient stability, depending on the power flow and fault location. Proposed method using f_{COI} as criterion can always improve the transient stability. However, if the communication is not as fast, the proposed method may also

get worse than the base case.

Figure 6-6 shows the frequency of G2 and G4 for Case 3 with 0.26 s fault clearing time using literature method. The exhibited inertia of the VSG as G4 is also plotted in the same figure for better demonstration. For comparison, the result using the proposed method with 0.36 s fault clearing time is shown in Figure 6-7.

In Figure 6-6 using literature method, G4 is controlled to have larger inertia immediately after the fault, since its output frequency is deviating from 60 Hz. This will create larger angle difference between G2 and G4, which is easier to reach the unstable equilibrium point and causes the

Table 6-3. Measured CCT with different control method

Control Methods	Case 1	Case 2	Case 3	Case 4
Base case	0.54 s	0.30 s	0.30 s	0.54 s
Literature method using f_n	0.52 s	0.38 s	0.26 s	0.64 s
Proposed method using f_{COI}	0.60 a	0.42 s	0.36 s	0.98 s
Proposed (100 ms additional delay)	0.54 s	0.42 s	0.32 s	0.96 s
Proposed (200 ms additional delay)	0.52 s	0.42 s	0.30 s	0.96 s
Proposed (300 ms additional delay)	0.52 s	0.42 s	0.26 s	0.96 s

generator sources out of step. In Figure 6-7 using the proposed method, G4 has an instance of larger inertia, then change to smaller inertia due to the time delay. This way, smaller angle difference leads to better transient stability performance.

The results also explain the effect of time delay in Table 6-3. If there are longer time delays, the instance of larger inertia may get longer, which will have the same effect as previous literature method during the first swing. The minimal time delay required for the proposed method will be studied in the future.

Figure 6-8 shows the result comparison for Case 2 with 0.28 s fault clearing time. With larger closed-loop time delay, system damping for oscillation may get worse. But for the same disturbance, the proposed method still has a better result than the literature method in terms of small-signal stability.

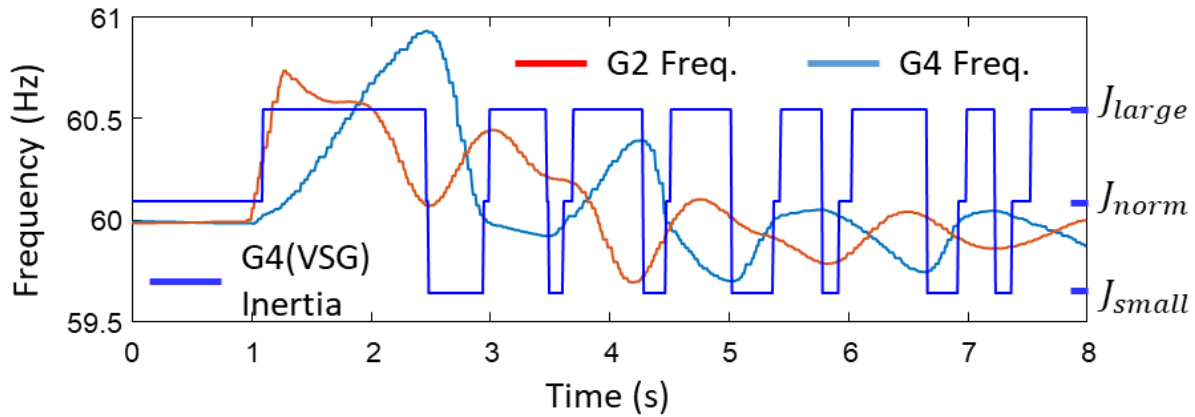


Figure 6-6. Experimental result for Case 3 with 0.26 s fault clearing time using literature method.

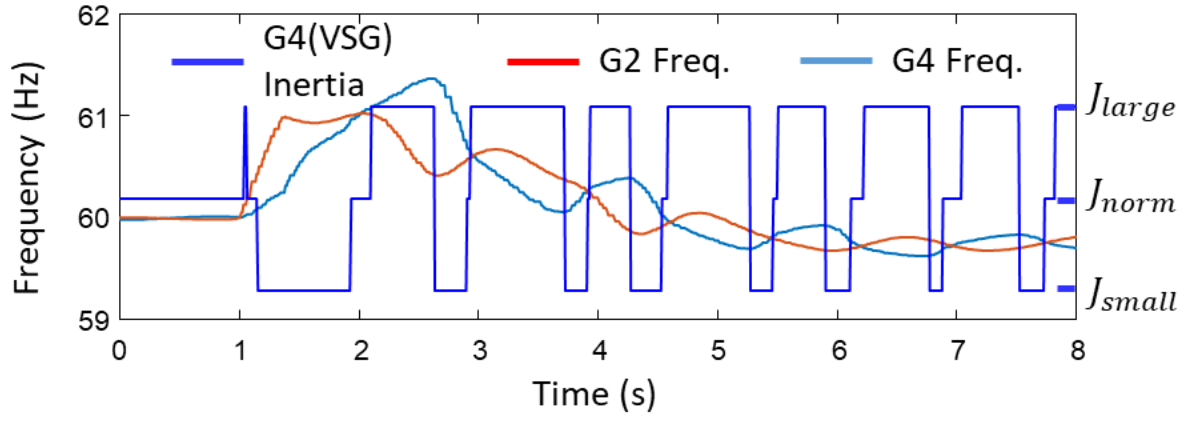


Figure 6-7. Experimental result for Case 3 with 0.36 s fault clearing time using proposed method.

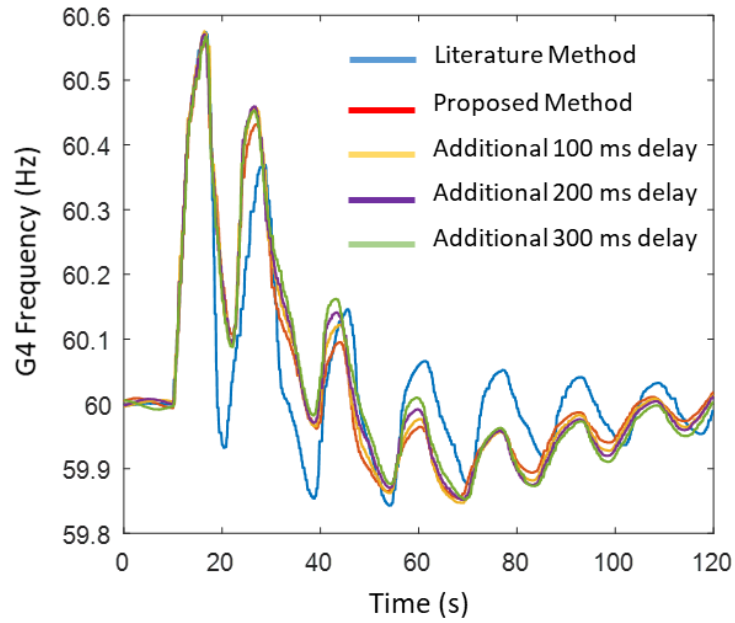


Figure 6-8. Experimental result comparison for Case 2 with 0.28 s fault clearing time with different controls.

6.4 Practicality Discussion

There have been previous studies on time delay of wide-area closed-loop control in the actual power system. The operational delay (caused by measurement or others) is around 51 ms, and the communication delay is around 36 ms [154]. Thus, it is reasonable to consider that closed-loop delay is less than 0.1 s at present, which is around the experimental set-up. The newer technology Time Sensitive Network (TSN) [155] may reduce the communication delay to around 2 ms [156]. The closed-loop delay may still likely be reduced further in the future.

In addition, extensive Phasor Measurement Units (PMU) deployment and its communications networks are required to determine the COI frequency, which is the trend of the future grid, and can be assumed available. A lower cost frequency measurement device Frequency Disturbance Recorder (FDR) may also be deployed [157]. As an alternative, the COI frequency can also be estimated by different system observing techniques [158].

In some systems where the fault locations do not make difference, the proposed method may not be needed. A control based on local information may be adopted to improve system transient stability.

6.5 Conclusion

This chapter proposes to use the center of inertia frequency as the reference criterion for the adaptive inertia scheme of virtual synchronous generator control. The proposed method provides enhancement to power system transient stability, whereas the existing methods may have adverse effect. Experimental results are presented to show the feasibility of the proposed method.

7 Impact of Limited Current to System Transient Stability and Its Mitigation

In the previous chapter, it is assumed that the output current of the VSG converter does not have any limit, which may not be the case in practical implementation. This chapter will introduce the impact of limited current to system transient stability, and propose methods to mitigate the impact.

7.1 Transient Stability Analysis in a Single Machine Infinite Bus System

This section starts to analyze the impact of current limitation in a single machine infinite bus system, as shown in Figure 7-1, where a VSG controlled power electronics source is connected to an infinite bus through a paralleled line. The disturbance is a three-phase short circuit fault, and relay protection trips one line to isolate the fault.

Figure 7-2 shows a typical locus of the VSG's output power and rotor angle as the base case when there is no current limit. To simplify the analysis, the assumptions include: a very slow excitation system, and large X/R ratio for the line impedance, and negligible transient and sub-transient dynamics for VSG control. The system starts from point A, with no active power output from the VSG. The rotor angle with respect to the infinite bus is 0° . Output power is then ramped to 0.7 p.u., at point B, before the short circuit fault triggers. The curve AB in Figure 7-2(d) follows the power angle characteristic estimated by:

$$P = \frac{EV}{X} \sin \theta \quad (7-1)$$

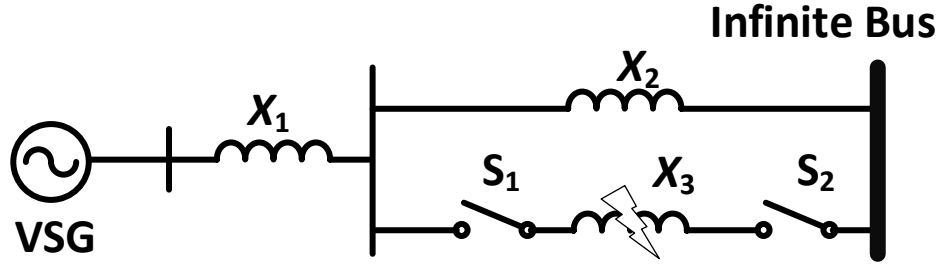


Figure 7-1. Simulation configuration for single machine infinite bus system.

where P is the output power, E is the internal excitation voltage for the VSG, X is the equivalent impedance of the system, which includes the line impedance and the emulated impedance of the VSG.

The fault current is around 3 p.u., at point B', and output electrical power reduces to around 0.2 p.u. Since the output electrical power is less than the emulated mechanical input of the VSG, the frequency increases, and rotor angle increases, until the fault is cleared at point C. The red shaded area in Figure 7-2(d) defined by point B, B' and C is the acceleration area, which represents the emulated kinetic energy stored in the rotor during the fault [49].

After the fault is cleared, the output power rises to another power angle curve different than curve AB, since the equivalent impedance is higher due to the line trip. The output electrical power is more than the mechanical input, the frequency starts to decrease. The rotor angle will rise to its peak value at point D, and decrease as the frequency of the VSG continues to decrease. The blue shaded area in Figure 7-2(d) is the deceleration area, which represents the kinetic energy released. The acceleration area is equal to the deceleration area, because the kinetic energy stored during the fault is all released at point D. After some oscillations, the operating point stabilized to point

E.

In this event, the potential deceleration area is larger than the acceleration area, and the system is stable after the fault. However, with a delayed fault clearing, the acceleration will be larger, the kinetic energy may not be completely expended before the electrical power output drops to be lower than the mechanical input. Beyond that, the frequency starts to increase again, and can lead to loss of synchronization. From the power angle diagram, once the acceleration area is larger than the deceleration area, the system is subject to transient stability issues.

Figure 7-2(e) shows the output current of the VSG during this event. During the fault, due to the low external voltage, the VSG may output larger current than its rated value. The amplitude is determined by the excitation, fault location, and VSG's internal impedance. After the fault, the output current may also be higher than rated. The amplitude is determined by the power angle characteristics (7-1). In the following sections, the response of a system with limited current will be analyzed

7.2 Impact of Limited Current in Single Machine Infinite Bus System

Figure 7-3 shows the voltage closed-loop control diagram for the VSG. Reference for the voltage output E_{t_ref} is calculated by current measurements I_{meas} and the model of the emulated SG. If there are no limitations on the output currents, the current reference input to the controller $I_{t_limited}$ will be equal to the output of the voltage controller I_{t_ref} . The output of the current controller is the duty-ratio of the power electronics converter d_{out} .

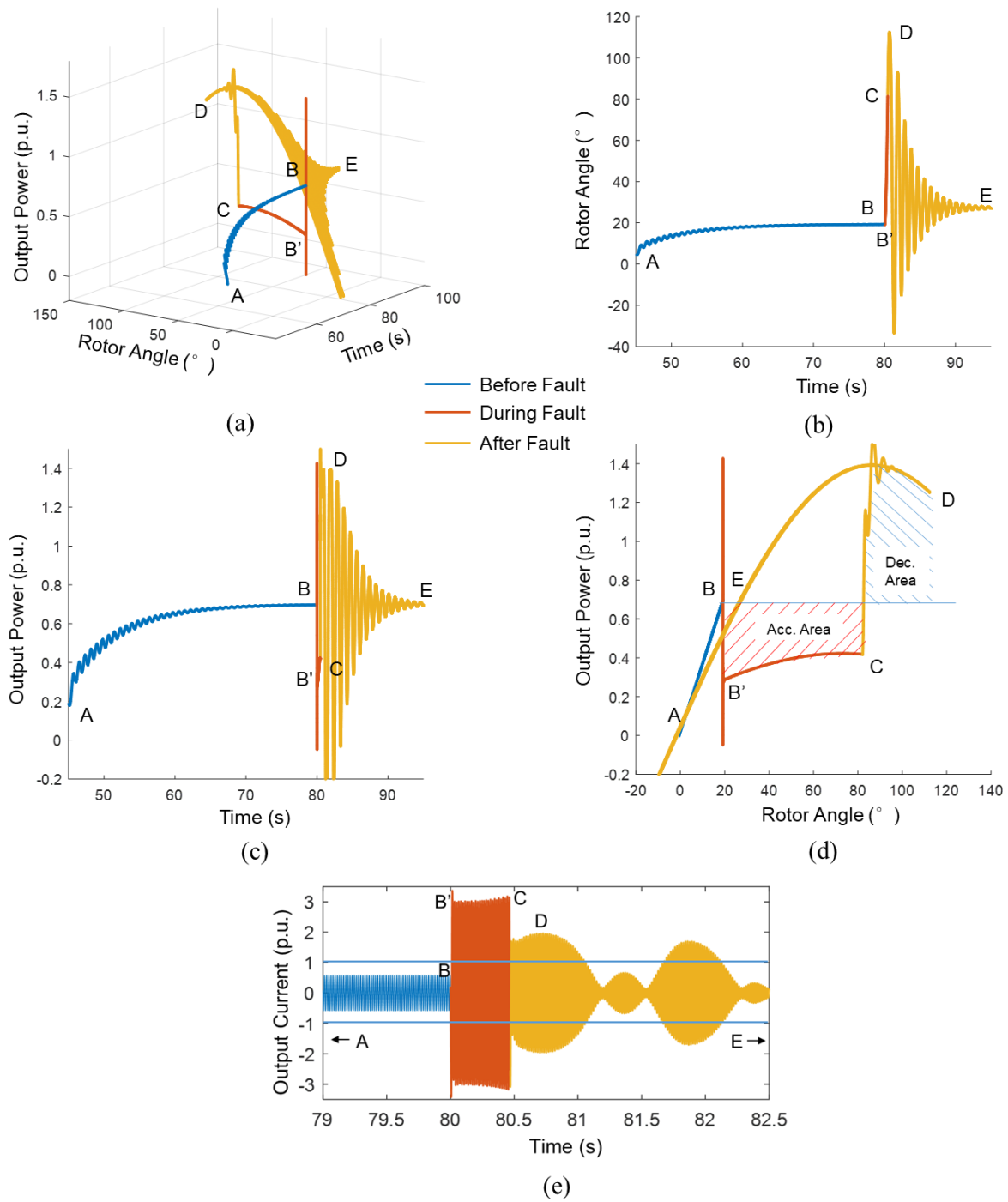


Figure 7-2. System response for a short circuit fault in a single machine infinite bus system, without current limitation.

There are multiple options on how to limit the current, as shown in Figure 7-4. For a given output current I_t , the output current may be proportionally reduced to $I_{t,p}$, or prioritize the current components in certain axes. In the figure, d-axis priority $I_{t,d}$ and q-axis priority $I_{t,q}$ are shown. There are also other limiting methods proposed in the literature [129, 130, 159].

After the output current is limited, the output voltage E_t will also be changed. It will not be equal to $E_q - jXI_t - R_a I_t$ anymore, and power angle relationship will not follow the equation described in (7-1).

Figure 7-5 shows the system responses for a VSG in the infinite bus system with the different settings, subjected to a fault with the same fault clearing time. The cases are indicated in the same manner as the power angle characteristics in Figure 7-2(d).

As discussed in the previous section, the impact of limited current is twofold. During the fault, the VSG will produce less current, which leads to less electrical power output, hence faster acceleration, and larger rotor angle deviation. From the power angle diagram, a larger acceleration area is then determined.

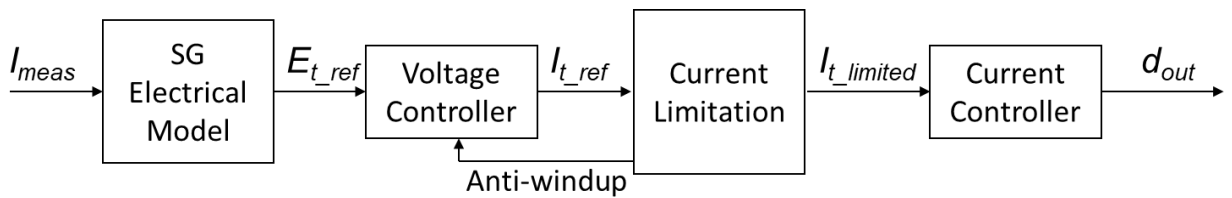


Figure 7-3. Diagram of VSG voltage closed-loop control.

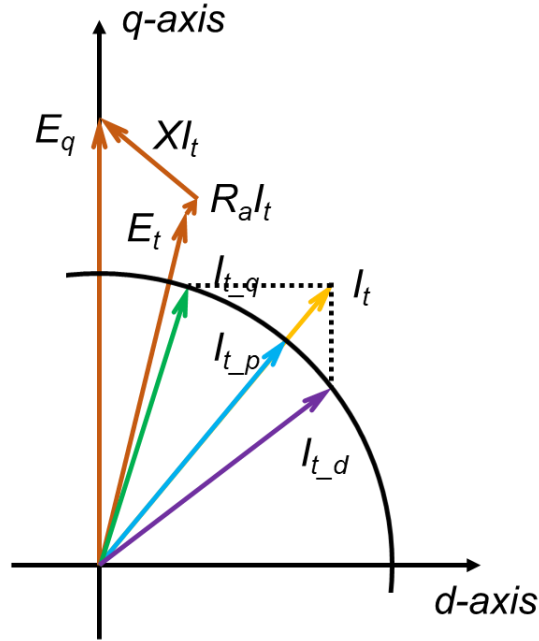


Figure 7-4. Current limitation methods.

After the fault is cleared, the operating point returns to follow the same power angle curve as the one without limit, until the current limit is triggered. No matter the limiting algorithm, the output power will be less than the one without a limit. From the power angle diagram, a smaller deceleration area is determined. This result matches with the analysis for droop controlled converter in [135].

As a result, a VSG with limited current output capacity will impair the system transient stability, in a single machine infinite bus system. This result is drawn from previous assumptions to simplify the analysis. If considering the excitation control, and transient and sub-transient

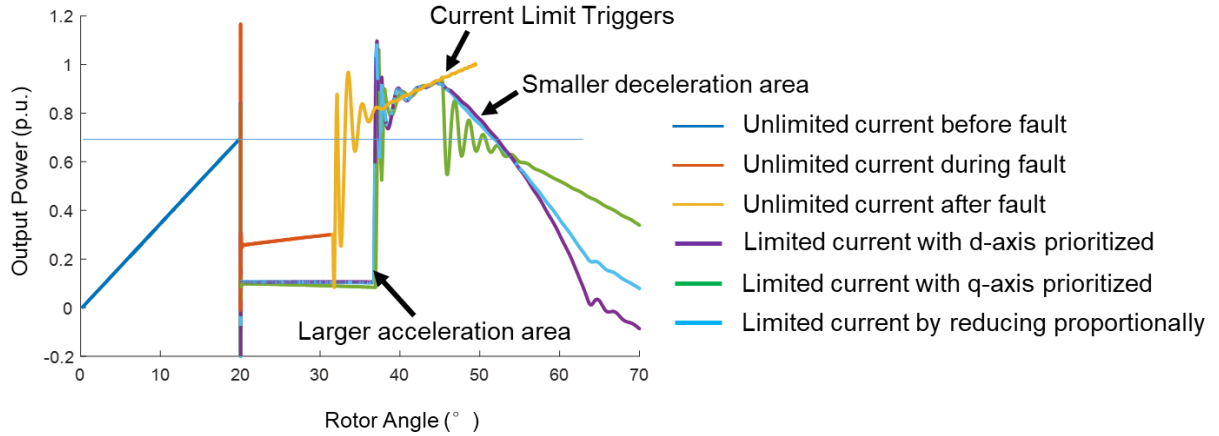


Figure 7-5. System response for a short circuit fault in a single machine infinite bus system, with limited current.

dynamics, the VSG should output additional current during the fault or after the fault, and eventually be limited. Thus, these factors should amplify the difference even more.

7.3 Proposed Control to Enhance Transient Stability When Current is Limited

To counter the disadvantage brought by the limited current, the VSG should (1) accelerate slower during the fault, and (2) allow more room for deceleration when the current is limited after the fault, before the electrical power output is less than the mechanical input.

Thanks to the flexibility of the power electronics control, the VSG does not have to exactly follow the physics of the SGs. An artificial electrical power output can be forged to be the input of the mechanical model of the VSG, instead of the actual electrical power output.

During the period of fault, the artificial electrical power should be larger than the actual output,

but smaller than the mechanical input. Such that the VSG may still accelerate, but slower than without the compensation. Thus, a weighted average between the mechanical input and electrical power output can be chosen as the artificial electrical power output. After the fault, once the current limit is triggered, it is advisable to create a large artificial electrical power, and let the VSG quickly decelerate, and exit the current limitation zone. During other times when the current is not limited, the proposed control should not interfere the normal operation of the VSG.

The proposed method can be summarized in Figure 7-6. In the actual implementation, m and n are set to 1, and k is set to 2. The value can be better designed depending on the specific cases.

Figure 7-7 shows the simulation result for a single machine infinite bus system. With the proposed control, the acceleration area is reduced, and the deceleration area is enlarged. Once the VSG enters the current limit zone, the large artificial electrical output helps the VSG to decelerate faster, and return to normal operation, and finally stabilize.

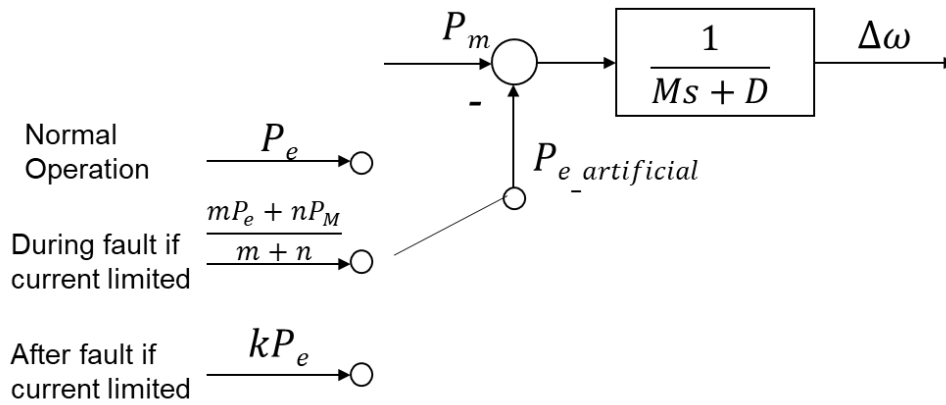


Figure 7-6. Proposed method to set artificial electrical power output to mitigate the impact of the limited current.

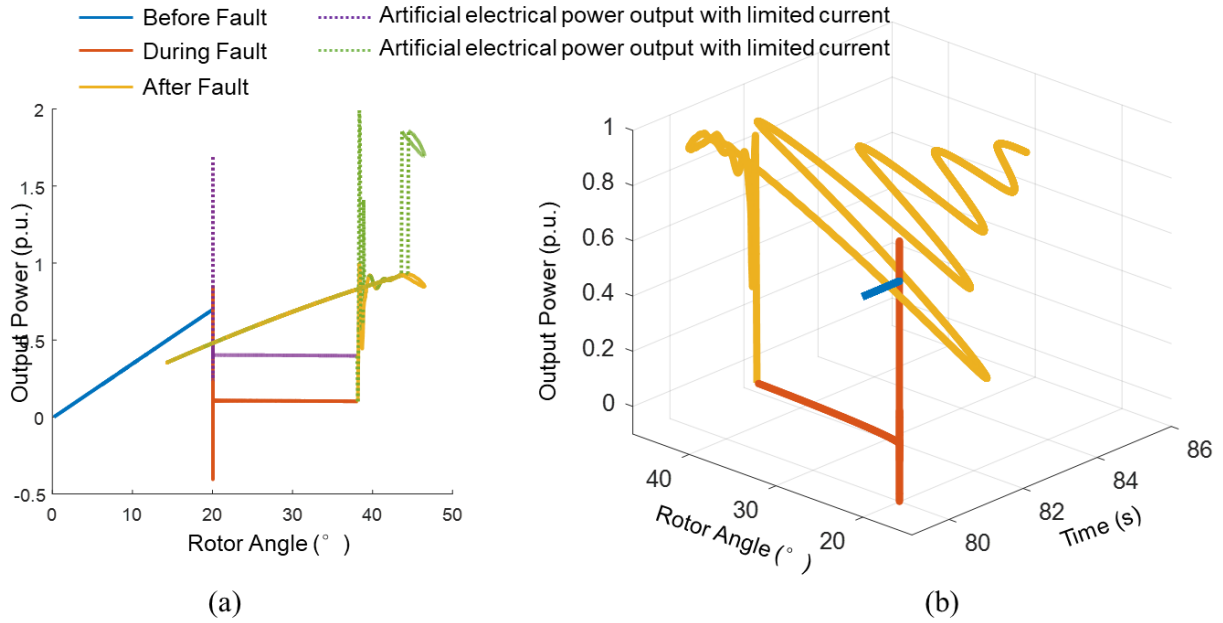


Figure 7-7. System response for a short circuit fault in a single machine infinite bus system, with proposed control to enhance the transient stability.

7.4 Experimental Result in HTB

Experiments are conducted in the HTB two-area system environment. The system configuration is shown in Table 5-1.

Figure 7-8 shows the oscilloscope measurement when the system is operated as Case 2 in Table 6-2. G4 is configured to be a VSG, with 0.30 s as the fault clearing time. In this case, the fault is closed to the VSG unit, and current limitation is triggered during the fault. If the current is limited during the fault, with the proposed control the system can still be stable. But without the proposed control, the system is unstable. This case has demonstrated the negative impact of current

limitation during the fault, and the proposed control helps to compensate it.

Similarly, Figure 7-9 shows the oscilloscope measurement when the system is operated as Case 3 in Table 6-2. G4 is configured to be a VSG, with 0.30 s as the fault clearing time. In this case, the fault is far away to the VSG unit, and current limitation did not trigger during the fault, but triggered after the fault. If the current is limited during the fault, with the proposed control the system can still be stable. But without the proposed control, the system is unstable. This case has demonstrated the negative impact of current limitation after the fault, and the proposed control also helps to compensate it.

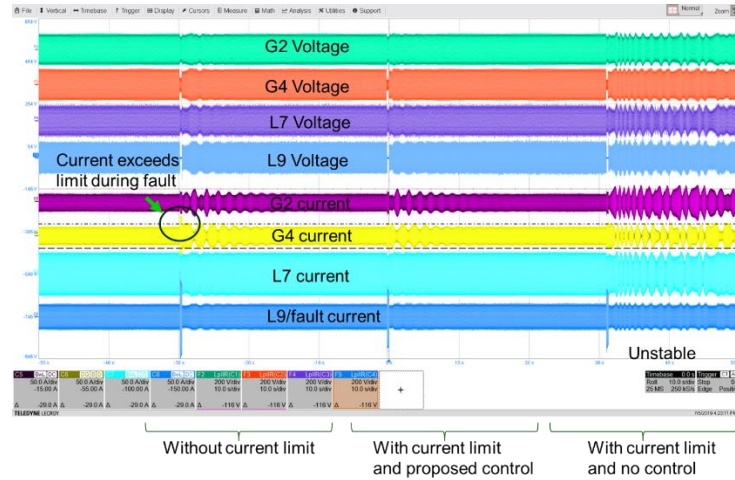


Figure 7-8. Oscilloscope measurement for a short circuit fault at bus 9 in the HTB two area system setup to compare the stability with no current limit, with current limit and proposed control, and with current limit and no control.

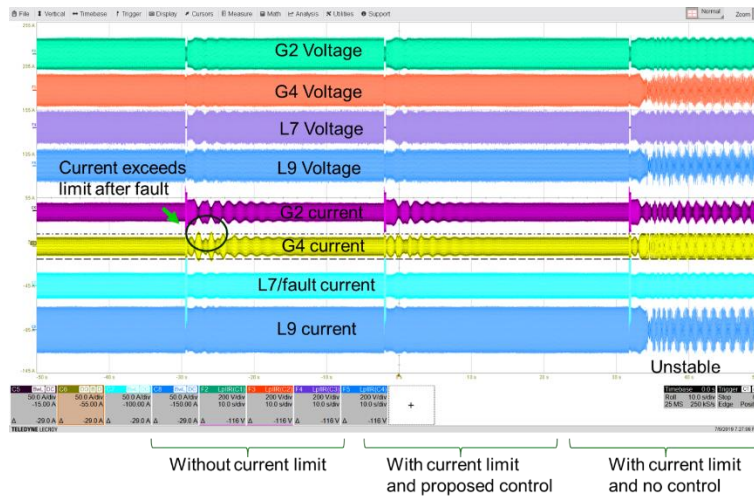


Figure 7-9. Oscilloscope measurement for a short circuit fault at bus 7 in the HTB two area system setup to compare the stability with no current limit, with current limit and proposed control, and with current limit and no control.

7.5 Discussion

It has been demonstrated in the HTB two area test platform, that the proposed control will help to alleviate the negative impact of the current limits. But it is still not theoretically proven that the proposed method will work all the time.

In some complexed system with multiple machines, it may be difficult to identify whether if the current limitation is caused by fault itself or the oscillation after the fault, especially the fault is far away from the VSG unit. If identified wrongly, the proposed control may have adverse effect to the system stability.

In addition, depending on whether if the rest of the system is accelerating or not, it may be beneficial to accelerate faster during the fault. In this case, wide-area measurement will be helpful to assist the identification of operating points.

It should be noted that since the purpose of the proposed control is not to enhance the transient stability, but to alleviate the adverse impact introduced by current limitation. It is not expected to have better CCT compared with the case with no current limitation. But the method can be combined with adaptive inertia method proposed in Chapter 6, to achieve better system transient stability.

7.6 Conclusion

During fault triggered large disturbance, a generator will produce large current during and after the fault. By limiting the output current of the VSG, the system transient stability becomes worse. This chapter proposed to artificially modify the electrical power input to the mechanical

model of the VSG, to enhance the transient stability when the output current is limited. Simulation in a single machine infinite bus system, and experiments in HTB two area system are conducted. The results have shown the effectiveness of the proposed control.

8 Conclusions and Future Work

8.1 Summary

This dissertation has explored the virtual synchronous generator (VSG) operation of full converter wind turbine (FCWT) under normal and fault condition, to actively provide grid support for renewable integrations. An FCWT emulator and a short circuit fault emulator have been developed in a power electronics based power system emulation platform, which is used to test the proposed control methods.

8.2 Contribution

The detailed contribution of this dissertation is as follows.

- A FCWT generation system emulator using one single converter is developed. The developed emulator can represent the static and dynamic behavior of the wind turbine without the need of real rotating machine. It allows the testing of different grid support functions in an emulated power system with high renewable penetration.
- A VSG control for FCWTs has been developed, with the consideration of a short term minute-level energy storage integrated on the dc link. It allows the FCWT to operate in both grid-connected and stand-alone conditions. Other grid supporting functions have been achieved by enabling non-MPPT operation of the wind turbine, and the FCWT can still exhibit SG dynamic behavior.
- A method to emulate four basic types of short circuit fault by using a shunt connected converter has been demonstrated. The developed fault emulator can achieve the same

voltage and current boundary condition as the short circuit faults, and essentially has the same impact to the system under tests. The transient stability of a power system under study can be investigated using the proposed fault emulator.

- An adaptive inertia method is proposed to improve the system transient stability for VSG control. By utilizing the center-of-inertia frequency obtained through wide-area measurements, the VSG unit may accelerate or decelerate in accordance with the rest of the system, which will in turn prevent the loss-of-synchronization.
- Limited output current for VSG controlled generation unit will impair the system transient stability, due to its less power output capability during and after the fault. A compensation method is proposed can mitigate the negative effect introduced by limited current.

8.3 Recommended Future Work

Some recommended future work is listed as follows.

(1) Power electronics design of VSG controlled wind turbine considering power system performance and requirements.

The research work in this dissertation mainly focused on the control of the wind turbine system under normal and fault operations. The energy capacity design of the storage is also briefly discussed. However, there are still knowledge gaps for the design of power electronics interface converters considering the power system performance and requirements. Previous studies have shown that providing more power from wind turbines during transient disturbances may help with system frequency and rotor angle stability. The power capacity design of the power electronics interface converter may be better designed for VSG applications.

(2) Modeling of the VSG controlled wind turbine in power system simulation software

Currently all the models used in this dissertation are user-defined models in MATLAB/Simulink, or C-based code for HTB emulators. A model is needed that can be used by power system simulation software, such as PSS/E, PSLF, etc. The model should have a unified approach to model the dynamic behaviors of the wind turbine incorporating both current and voltage control modes, as well as mode transitions. This will greatly help with power system researchers to identify the impact of integration of renewable energy sources with different potential control algorithms.

(3) Coordinated control of multiple VSG controlled wind turbines

In this dissertation, the wind turbine emulator could represent a single wind turbine, or the aggregation of a wind farm with the assumption that the wind speed is similar for all the wind turbines in the area. Simulation and experimental results have proven that the proposed VSG control may be applied to wind turbines with different wind speed in different region of the test system without any issues. But it is still beneficial to develop coordinated control strategies for the wind turbines in a wind farm or a larger area with different available wind power. By adjusting the power setpoint of the wind turbines within the wind farm, it is possible to minimize the line losses, and maximize the utilization of the headroom for system frequency support.

Reference

- [1] *U.S. number one in the world in wind energy production*, AWEA, [Online]. Available: <https://www.awea.org/resources/press-releases/2016/u-s-number-one-in-the-world-in-wind-energy-product>
- [2] *Renewables 2014 Global Status Report*, REN21, [Online]. Available: <http://www.ren21.net>
- [3] *Wind Vision: A New Era for Wind Power in the United States*, US DOE, [Online]. Available: <http://www.energy.gov/windvision>
- [4] J. Serrano - González and R. Lacal - Arántegui, “Technological evolution of onshore wind turbines—a market - based analysis,” *Wind Energy*, vol. 19, no. 12, pp. 2171-2187, 2016.
- [5] F. Blaabjerg and K. Ma, “Future on power electronics for wind turbine systems,” *IEEE Trans. Emerg. Sel. Topics Power Electron.*, vol. 1, no. 3, pp. 139-152, 2013.
- [6] J. Morren, S. W. De Haan, W. L. Kling, and J. Ferreira, “Wind turbines emulating inertia and supporting primary frequency control,” *IEEE Trans. Power Syst.*, vol. 21, no. 1, pp. 433-434, 2006.
- [7] N. R. Ullah, K. Bhattacharya, and T. Thiringer, “Wind farms as reactive power ancillary service providers—technical and economic issues,” *IEEE Trans. Energy Convers.*, vol. 24, no. 3, pp. 661-672, 2009.
- [8] N. R. Ullah, T. Thiringer, and D. Karlsson, “Temporary primary frequency control support by variable speed wind turbines—Potential and applications,” *IEEE Trans. Power Syst.*, vol. 23, no. 2, pp. 601-612, 2008.
- [9] M. Liserre, R. Cardenas, M. Molinas, and J. Rodriguez, “Overview of multi-MW wind turbines and wind parks,” *IEEE Trans. Ind. Electron.*, vol. 58, no. 4, pp. 1081-1095, 2011.
- [10] Q.-C. Zhong and G. Weiss, “Synchronverters: Inverters that mimic synchronous generators,” *IEEE Trans. Ind. Electron.*, vol. 58, no. 4, pp. 1259-1267, 2011.
- [11] J. Driesen and K. Visscher, “Virtual synchronous generators,” in *Proc. IEEE PES Meeting*, 2008, pp. 20-24.
- [12] Y. Chen, R. Hesse, D. Turschner, and H.-P. Beck, “Improving the grid power quality using virtual synchronous machines,” in *Proc. Power engineering, energy and electrical drives (POWERENG)*, 2011, pp. 1-6.
- [13] M. Torres and L. A. Lopes, “Virtual synchronous generator control in autonomous wind-diesel power systems,” in *Proc. IEEE EPEC*, 2009, pp. 1-6.
- [14] C. Li, R. Burgos, I. Cvetkovic, D. Boroyevich, L. Mili, and P. Rodriguez, “Evaluation and control design of virtual-synchronous-machine-based STATCOM for grids with high penetration of renewable energy,” in *Proc. IEEE ECCE*, 2014, pp. 5652-5658.
- [15] J. Mahseredjian, V. Dinavahi, and J. A. Martinez, “Simulation tools for electromagnetic

- transients in power systems: Overview and challenges,” *IEEE Trans. Power Del.*, vol. 24, no. 3, pp. 1657-1669, 2009.
- [16] R. Kuffel, J. Giesbrecht, T. Maguire, R. Wierckx, and P. McLaren, “RTDS-a fully digital power system simulator operating in real time,” in *Proc. IEEE EMPD*, 1995, pp. 498-503.
 - [17] S. Abourida, C. Dufour, J. Bélanger, G. Murere, N. Lechevin, and B. Yu, “Real-time PC-based simulator of electric systems and drives,” in *Proc. IEEE APEC*, 2002, pp. 433-438.
 - [18] E. Adzic, S. Grabic, M. Vekic, V. Porobic, and N. F. Celanovic, “Hardware-in-the-loop optimization of the 3-phase grid connected converter controller,” in *Proc. IEEE IECON*, 2013, pp. 5392-5397.
 - [19] I. A. Hiskens and J. Alseddiqui, “Sensitivity, approximation, and uncertainty in power system dynamic simulation,” *IEEE Trans. Power Syst.*, vol. 21, no. 4, pp. 1808-1820, 2006.
 - [20] X. Wu, S. Lentijo, A. Deshmuk, A. Monti, and F. Ponci, “Design and implementation of a power-hardware-in-the-loop interface: a nonlinear load case study,” in *Proc. IEEE APEC*, 2005, pp. 1332-1338.
 - [21] O. Schurig, “A miniature ac transmission system for the practical solution of network and transmission-system problems,” *Transactions of the American Institute of Electrical Engineers*, vol. 42, pp. 831-840, 1923.
 - [22] H. L. Hazen, O. Schurig, and M. F. Gardner, “The mit network analyzer design and application to power system problems,” *Transactions of the American Institute of Electrical Engineers*, vol. 49, no. 3, pp. 1102-1113, 1930.
 - [23] B. Kroposki, D. Mooney, T. Markel, and B. Lundstrom, “Energy systems integration facilities at the national renewable energy laboratory,” in *Proc. IEEE Energytech*, 2012, pp. 1-4.
 - [24] R. H. Lasseter, J. H. Eto, B. Schenkman, J. Stevens, H. Vollkommer, D. Klapp, E. Linton, H. Hurtado, and J. Roy, “CERTS microgrid laboratory test bed,” *IEEE Trans. Power Del.*, vol. 26, no. 1, pp. 325-332, 2011.
 - [25] J. Bone, “Influence of rotor diameter and length on the rating of induction motors,” *IEE Journal On Electric Power Applications*, vol. 1, no. 1, pp. 2-6, 1978.
 - [26] L. Lopes, J. Lhuillier, M. Khokar, and A. Mukherjee, “A wind turbine emulator that represents the dynamics of the wind turbine rotor and drive train,” in *Proc. IEEE PESC*, 2005, pp. 2092-2097.
 - [27] Y. Ma, J. Wang, F. Wang, and L. M. Tolbert, “Converter-based reconfigurable real-time electrical system emulation platform,” *Chinese Journal of Electrical Engineering*, vol. 4, no. 1, pp. 20-27, 2018.
 - [28] H. Slater, D. Atkinson, and A. Jack, “Real-time emulation for power equipment development. Part 2: The virtual machine,” *IEE Proceedings-Electric Power*

- Applications*, vol. 145, no. 3, pp. 153-158, 1998.
- [29] W. A. Peterson, "Methods and apparatus for motor emulation," U.S. Patent US8587322, 2013.
 - [30] *AVTestSystems/AV-900/900CE* [Online]. Available: <http://www.avtest-systems.com/av-900>
 - [31] *The SPS E-Motor Emulator (EME)* [Online]. Available: <http://www.set-powersys.de/en/eme/>
 - [32] L. Yang, Y. Ma, J. Wang, J. Wang, X. Zhang, L. M. Tolbert, F. Wang, and K. Tomsovic, "Development of converter based reconfigurable power grid emulator," in *Proc. IEEE ECCE*, 2014, pp. 3990-3997.
 - [33] L. Yang, X. Zhang, Y. Ma, J. Wang, L. Hang, K. Lin, L. M. Tolbert, F. Wang, and K. Tomsovic, "Stability analysis of inverter based generator emulator in test-bed for power systems," in *Proc. IEEE ECCE*, 2013, pp. 5410-5417.
 - [34] L. Yang, X. Zhang, Y. Ma, J. Wang, L. Hang, K. Lin, L. M. Tolbert, F. Wang, and K. Tomsovic, "Hardware implementation and control design of generator emulator in multi-converter system," in *Proc. IEEE APEC*, 2013, pp. 2316-2323.
 - [35] L. Yang, J. Wang, Y. Ma, J. Wang, X. Zhang, L. M. Tolbert, F. Wang, and K. Tomsovic, "Three-Phase Power Converter-Based Real-Time Synchronous Generator Emulation," *IEEE Trans. Power Electron.*, vol. 32, no. 2, pp. 1651-1665, 2017.
 - [36] J. Wang, L. Yang, Y. Ma, J. Wang, L. M. Tolbert, F. Wang, and K. Tomsovic, "Static and dynamic power system load emulation in a converter-based reconfigurable power grid emulator," *IEEE Trans. Power Electron.*, vol. 31, no. 4, pp. 3239-3251, 2016.
 - [37] J. Wang, L. Yang, Y. Ma, X. Shi, X. Zhang, L. Hang, K. Lin, L. M. Tolbert, F. Wang, and K. Tomsovic, "Regenerative power converters representation of grid control and actuation emulator," in *Proc. IEEE ECCE*, 2012, pp. 2460-2465.
 - [38] J. Wang, Y. Ma, L. Yang, L. M. Tolbert, and F. Wang, "Power converter-based three-phase induction motor load emulator," in *Proc. IEEE APEC*, 2013, pp. 3270-3274.
 - [39] W. Cao, Y. Ma, J. Wang, L. Yang, J. Wang, F. Wang, and L. M. Tolbert, "Two-stage PV inverter system emulator in converter based power grid emulation system," in *Proc. IEEE ECCE*, 2013, pp. 4518-4525.
 - [40] J. Wang, L. Yang, C. Blalock, and L. M. Tolbert, "Flywheel energy storage emulation using reconfigurable hardware test-bed of power converters," in *Proc. Elect. Energy Storage Appl. Technol.*, 2013.
 - [41] J. D. Boles, Y. Ma, L. M. Tolbert, and F. Wang, "Frequency support comparison for vanadium and lithium-ion BESSs using a converter-based grid emulator," in *Proc. IEEE APEC*, 2018, pp. 623-630.
 - [42] J. D. Boles, Y. Ma, W. Cao, L. M. Tolbert, and F. Wang, "Battery energy storage

- emulation in a converter-based power system emulator,” in *Proc. IEEE APEC*, 2017, pp. 2355-2362.
- [43] S. Zhang, B. Liu, S. Zheng, Y. Ma, F. Wang, and L. M. Tolbert, “Development of a converter-based transmission line emulator with three-phase short-circuit fault emulation capability,” *IEEE Trans. Power Electron.*, 2018.
 - [44] S. Zhang, B. Liu, S. Zheng, Y. Ma, F. Wang, and L. M. Tolbert, “Three-phase short-circuit fault implementation in converter based transmission line emulator,” in *Proc. IEEE ECCE*, 2017, pp. 2914-2920.
 - [45] B. Liu, S. Zheng, Y. Ma, F. Wang, and L. M. Tolbert, “Control and implementation of converter based ac transmission line emulation,” in *Proc. IEEE APEC*, 2015, pp. 1807-1814.
 - [46] B. Liu, S. Zhang, S. Zheng, Y. Ma, F. Wang, and L. M. Tolbert, “Design consideration of converter based transmission line emulation,” in *Proc. IEEE APEC*, 2016, pp. 966-973.
 - [47] Y. Li, X. Shi, B. Liu, W. Lei, F. Wang, and L. M. Tolbert, “Development, demonstration, and control of a testbed for multiterminal HVDC system,” *IEEE Trans. Power Electron.*, vol. 32, no. 8, pp. 6069-6078, 2017.
 - [48] Y. Ma, L. Yang, J. Wang, X. Shi, F. Wang, and L. M. Tolbert, “Circulating current control and reduction in a paralleled converter test-bed system,” in *Proc. IEEE ECCE*, 2013, pp. 5426-5432.
 - [49] P. Kundur, *Power System Stability and Control*. New York: McGraw-Hill, 1994.
 - [50] S. Zhang, Y. Ma, L. Yang, F. Wang, and L. M. Tolbert, “Development of a hybrid emulation platform based on RTDS and reconfigurable power converter-based testbed,” in *Proc. IEEE APEC*, 2016, pp. 3121-3127.
 - [51] L. Zhu, Y. Zhao, Y. Ma, J. Wang, Y. Liu, E. Farantatos, M. Patel, and D. Ramasubramanian, “Adaptive wide-area damping control using transfer function model derived from ring-down measurements,” in *Proc. CIGRE US National Committee Grid of the Future Symposium* 2018, pp. 1-8.
 - [52] L. Zhu, H. Liu, Y. Ma, Y. Liu, E. Farantatos, M. Patel, and S. McGuinness, “Adaptive and coordinated oscillation damping control using measurement-driven approach,” in *Proc. Power Systems Computation Conference (PSCC)*, 2016, pp. 1-7.
 - [53] F. Bai, L. Zhu, Y. Liu, X. Wang, K. Sun, Y. Ma, M. Patel, E. Farantatos, and N. Bhatt, “Design and implementation of a measurement-based adaptive wide-area damping controller considering time delays,” *Electric Power Systems Research*, vol. 130, pp. 1-9, 2016.
 - [54] “Demonstration of oscillation damping control using measurement-based transfer function model on the CURENT hardware testbed,” Electric Power Research Institute, Dec 14, 2016, Available: <https://www.epri.com/#/pages/product/3002008407/>.
 - [55] F. Hu, L. Yang, J. Wang, Y. Ma, K. Sun, L. M. Tolbert, and F. Wang, “Measurement-

- based voltage stability assessment and control on CURENT hardware test bed system,” in *Proc. IEEE PESGM*, 2016, pp. 1-5.
- [56] W. Cao, Y. Ma, L. Yang, F. Wang, and L. M. Tolbert, “D–q impedance based stability analysis and parameter design of three-phase inverter-based ac power systems,” *IEEE Trans. Ind. Electron.*, vol. 64, no. 7, pp. 6017-6028, 2017.
 - [57] W. Cao, Y. Ma, and F. Wang, “Sequence-Impedance-Based Harmonic Stability Analysis and Controller Parameter Design of Three-Phase Inverter-Based Multibus AC Power Systems,” *IEEE Trans. Power Electron.*, vol. 32, no. 10, pp. 7674-7693, 2017.
 - [58] W. Cao, Y. Ma, and F. Wang, “Harmonic stability analysis and controller parameter design of three-phase inverter-based multi-bus ac systems based on sequence impedances,” in *Proc. IEEE ECCE*, 2016, pp. 1-8.
 - [59] A. Ellis, E. Muljadi, J. Sanchez-Gasca, and Y. Kazachkov, “Generic models for simulation of wind power plants in bulk system planning studies,” in *Proc. IEEE PESGM*, 2011, pp. 1-8.
 - [60] A. D. Hansen, C. Jauch, P. Sørensen, F. Iov, and F. Blaabjerg, “Dynamic wind turbine models in power system simulation tool DIGSILENT,” *Report Risoe*, pp. 1-80, 2003.
 - [61] D. S. Dolan and P. W. Lehn, “Simulation model of wind turbine 3p torque oscillations due to wind shear and tower shadow,” in *Proc. IEEE PSCE*, 2006, pp. 2050-2057.
 - [62] D. Dolan and P. Lehn, *Real-time wind turbine emulator suitable for power quality and dynamic control studies*. University of Toronto, 2005.
 - [63] M. Monfared, H. M. Kojabadi, and H. Rastegar, “Static and dynamic wind turbine simulator using a converter controlled dc motor,” *Renewable Energy*, vol. 33, no. 5, pp. 906-913, 2008.
 - [64] S. Kumsup and C. Tarasantisuk, “Real-time wind turbine emulator for testing wind energy conversion systems,” in *Proc. IEEE EnergyCon*, 2010, pp. 7-9.
 - [65] R. V. Gokhale, S. M. Mahajan, B. W. Abegaz, and R. P. Craven, “Development of a real time wind turbine emulator based on RTDS using advanced perturbation methods,” in *Proc. IEEE IEEEIC*, 2015, pp. 1713-1718.
 - [66] H. Guo, B. Zhou, J. Li, F. Cheng, and L. Zhang, “Real-time simulation of BLDC-based wind turbine emulator using RT-LAB,” in *Proc. IEEE ICEMS*, 2009, pp. 1-6.
 - [67] M. Moness, M. O. Mahmoud, and A. M. Moustafa, “A real-time heterogeneous emulator of a high-fidelity utility-scale variable-speed variable-pitch wind turbine,” *IEEE Trans. Ind. Informat.*, vol. 14, no. 2, pp. 437-447, 2018.
 - [68] M. Y. Borodulin, “Effect of numerical integration on critical time evaluation in power system stability studies,” in *Proc. IEEE PESGM*, 2013, pp. 1-5.
 - [69] R. Concepcion, R. Elliott, M. Donnelly, and J. Sanchez-Gasca, “On extended-term dynamic simulations with high penetrations of photovoltaic generation,” in *Proc. IEEE*

- PESGM*, 2016, pp. 1-5.
- [70] P. Flannery and G. Venkataramanan, "Unbalanced voltage sag ride-through of a doubly fed induction generator wind turbine with series grid side converter," in *Proc. IEEE IAS Annual Meeting*, 2008, pp. 1-8.
 - [71] D. Atkinson, G. Pannell, W. Cao, B. Zahawi, T. Abeyasekera, and M. Jovanovic, "A doubly-fed induction generator test facility for grid fault ride-through analysis," *IEEE Instrumentation & Measurement Magazine*, vol. 15, no. 6, 2012.
 - [72] N. R. Averous, H. Stagge, and R. W. De Doncker, "Performance characteristics of a doubly-fed generator on a test-rig with full-scale converter-based grid emulator," in *Proc. IEEE PEMWA*, 2014, pp. 1-8.
 - [73] M. S. Almas, R. Leelaruiji, and L. Vanfretti, "Over-current relay model implementation for real time simulation & Hardware-in-the-Loop (HIL) validation," in *Proc. IEEE IECON*, 2012, pp. 4789-4796.
 - [74] D. J. Hogan, M. G. Egan, J. G. Hayes, G. Lightbody, and F. Gonzalez-Espin, "A rapid prototyping tool for load and source emulation in a microgrid test laboratory," in *Proc. IEEE APEC*, 2014, pp. 2245-2252.
 - [75] Y. Liu, C. Farnell, J. C. Balda, and H. A. Mantooth, "A 13.8-kV 4.75-MVA microgrid laboratory test bed," in *Proc. IEEE APEC*, 2015, pp. 697-702.
 - [76] E. Collins and R. Morgan, "A three-phase sag generator for testing industrial equipment," *IEEE Trans. Power Del.*, vol. 11, no. 1, pp. 526-532, 1996.
 - [77] C. Wessels, R. Lohde, and F. Fuchs, "Transformer based voltage sag generator to perform LVRT and HVRT tests in the laboratory," in *Proc. IEEE EPE/PEMC*, 2010, pp. T11-8-T11-13.
 - [78] M. García-Gracia, M. P. Comech, J. Sallán, D. López-Andía, and O. Alonso, "Voltage dip generator for wind energy systems up to 5 MW," *Applied Energy*, vol. 86, no. 4, pp. 565-574, 2009.
 - [79] Y. Ma, L. Yang, F. Wang, and L. M. Tolbert, "Short circuit fault emulation by shunt connected voltage source converter," in *Proc. IEEE ECCE*, 2015, pp. 2622-2628.
 - [80] J. López, E. Gubía, E. Olea, J. Ruiz, and L. Marroyo, "Ride through of wind turbines with doubly fed induction generator under symmetrical voltage dips," *IEEE Trans. Industrial Electronics*, vol. 56, no. 10, pp. 4246-4254, 2009.
 - [81] M. Mesbah, P. S. Moses, S. M. Islam, and M. A. Masoum, "Digital implementation of a fault emulator for transient study of power transformers used in grid connection of wind farms," *IEEE Trans. Sustain. Energy*, vol. 5, no. 2, pp. 646-654, 2014.
 - [82] S. M. R. Kazmi, H. Goto, H.-J. Guo, and O. Ichinokura, "Review and critical analysis of the research papers published till date on maximum power point tracking in wind energy conversion system," in *Proc. IEEE ECCE*, 2010, pp. 4075-4082.

- [83] J. C. Vieira, W. Freitas, W. Xu, and A. Morelato, "Performance of frequency relays for distributed generation protection," *IEEE Trans. Power Del.*, vol. 21, no. 3, pp. 1120-1127, 2006.
- [84] B. Wang, Y. Zhang, K. Sun, and K. Tomsovic, "Quantifying the synthetic inertia and load-damping effect of a converter-interfaced power source," in *Proc. 2018 IEEE International Energy Conference (ENERGYCON)*, 2018.
- [85] J. Van de Vyver, J. D. De Kooning, B. Meersman, L. Vandeveld, and T. L. Vandoorn, "Droop control as an alternative inertial response strategy for the synthetic inertia on wind turbines," *IEEE Trans. Power Syst.*, vol. 31, no. 2, pp. 1129-1138, 2016.
- [86] J. Brisebois and N. Aubut, "Wind farm inertia emulation to fulfill Hydro-Québec's specific need," in *Proc. IEEE PESGM*, 2011, pp. 1-7.
- [87] Y. Wang, G. Delille, H. Bayem, X. Guillaud, and B. Francois, "High wind power penetration in isolated power systems—Assessment of wind inertial and primary frequency responses," *IEEE Trans. Power Syst.*, vol. 28, no. 3, pp. 2412-2420, 2013.
- [88] L. Rutledge, N. W. Miller, J. O'Sullivan, and D. Flynn, "Frequency response of power systems with variable speed wind turbines," *IEEE Trans. Sustain. Energy*, vol. 3, no. 4, pp. 683-691, 2012.
- [89] M. S. Griffith, "Modern ac generator control systems: some plain and painless facts," *IEEE Trans. Ind. Appl.*, no. 6, pp. 481-491, 1978.
- [90] K. De Brabandere, B. Bolsens, J. Van den Keybus, A. Woyte, J. Driesen, and R. Belmans, "A voltage and frequency droop control method for parallel inverters," *IEEE Trans. Power Electron.*, vol. 22, no. 4, pp. 1107-1115, 2007.
- [91] E. Hinrichsen, "Controls for variable pitch wind turbine generators," *IEEE Trans. Power App. Syst.*, no. 4, pp. 886-892, 1984.
- [92] Y.-z. Sun, Z.-s. Zhang, G.-j. Li, and J. Lin, "Review on frequency control of power systems with wind power penetration," in *Proc. IEEE POWERCON*, 2010, pp. 1-8.
- [93] K. Vidyandandan and N. Senroy, "Primary frequency regulation by deloaded wind turbines using variable droop," *IEEE Trans. Power Syst.*, vol. 28, no. 2, pp. 837-846, 2013.
- [94] W. Cao, Y. Ma, J. Wang, and F. Wang, "Virtual series impedance emulation control for remote PV or wind farms," in *Proc. IEEE APEC*, 2014, pp. 411-418.
- [95] W. Zhang, F. Li, and L. M. Tolbert, "Review of reactive power planning: objectives, constraints, and algorithms," *IEEE Trans. Power Syst.*, vol. 22, no. 4, pp. 2177-2186, 2007.
- [96] A. Tapia, G. Tapia, and J. Ostolaza, "Reactive power control of wind farms for voltage control applications," *Renewable energy*, vol. 29, no. 3, pp. 377-392, 2004.
- [97] M. Kayikci and J. V. Milanovic, "Reactive power control strategies for DFIG-based

- plants,” *IEEE Trans. Energy Convers.*, vol. 22, no. 2, pp. 389-396, 2007.
- [98] N. Jelani, M. Molinas, and S. Bolognani, “Reactive power ancillary service by constant power loads in distributed AC systems,” *IEEE Trans. Power Del.*, vol. 28, no. 2, pp. 920-927, 2013.
 - [99] M. Tsili and S. Papathanassiou, “A review of grid code technical requirements for wind farms,” *IET Renewable power generation*, vol. 3, no. 3, pp. 308-332, 2009.
 - [100] Y. Zhou, D. Nguyen, P. Kjaer, and S. Saylor, “Connecting wind power plant with weak grid-Challenges and solutions,” in *Proc. IEEE PESGM*, 2013, pp. 1-7.
 - [101] A. Golieva, “Low short-circuit ratio connection of wind power plants,” Master Thesis, NTNU, 2015.
 - [102] S.-H. Huang, J. Schmall, J. Conto, J. Adams, Y. Zhang, and C. Carter, “Voltage control challenges on weak grids with high penetration of wind generation: ERCOT experience,” in *Proc. IEEE PESGM*, 2012, pp. 1-7.
 - [103] Q.-C. Zhong, P.-L. Nguyen, Z. Ma, and W. Sheng, “Self-synchronized synchronverters: Inverters without a dedicated synchronization unit,” *IEEE Trans. Power Electron.*, vol. 29, no. 2, pp. 617-630, 2014.
 - [104] J. Liu, Y. Miura, and T. Ise, “Comparison of dynamic characteristics between virtual synchronous generator and droop control in inverter-based distributed generators,” *IEEE Trans. Power Electron.*, vol. 31, no. 5, pp. 3600-3611, 2016.
 - [105] P. Rodriguez, C. Citro, J. I. Candela, J. Rocabert, and A. Luna, “Flexible grid connection and islanding of SPC-based PV power converters,” *IEEE Trans. Ind. Appl.*, vol. 54, no. 3, pp. 2690-2702, 2018.
 - [106] T. Shintai, Y. Miura, and T. Ise, “Reactive power control for load sharing with virtual synchronous generator control,” in *Proc. Power Electronics and Motion Control Conference (IPEMC), 2012 7th International*, 2012, pp. 846-853.
 - [107] S. D’Arco, J. A. Suul, and O. B. Fosso, “Control system tuning and stability analysis of virtual synchronous machines,” in *Proc. IEEE ECCE*, 2013, pp. 2664-2671.
 - [108] C. Li, R. Burgos, I. Cvetkovic, D. Boroyevich, and L. Mili, “Design, analysis and experimental evaluation of a virtual-synchronous-machine-based STATCOM with LCL filter,” in *Proc. IEEE ECCE*, 2015, pp. 5771-5778.
 - [109] R. Aouini, B. Marinescu, K. B. Kilani, and M. Elleuch, “Synchronverter-based emulation and control of HVDC transmission,” *IEEE Trans. Power Syst.*, vol. 31, no. 1, pp. 278-286, 2016.
 - [110] S. Wang, J. Hu, and X. Yuan, “Virtual synchronous control for grid-connected DFIG-based wind turbines,” *IEEE Trans. Emerg. Sel. Topics Power Electron.*, vol. 3, no. 4, pp. 932-944, 2015.
 - [111] Q.-C. Zhong, Z. Ma, W.-L. Ming, and G. C. Konstantopoulos, “Grid-friendly wind power

- systems based on the synchronverter technology,” *Energy Conversion and Management*, vol. 89, pp. 719-726, 2015.
- [112] X. Yuan, F. Wang, D. Boroyevich, Y. Li, and R. Burgos, “DC-link voltage control of a full power converter for wind generator operating in weak-grid systems,” *IEEE Trans. Power Electron.*, vol. 24, no. 9, pp. 2178-2192, 2009.
 - [113] Y. Q. Bao and Y. Li, “On deloading control strategies of wind generators for system frequency regulation,” *International Transactions on Electrical Energy Systems*, vol. 25, no. 4, pp. 623-635, 2015.
 - [114] S. Mueen, R. Takahashi, T. Murata, and J. Tamura, “Integration of an energy capacitor system with a variable-speed wind generator,” *IEEE Trans. Energy Convers.*, vol. 24, no. 3, pp. 740-749, 2009.
 - [115] R. Cárdenas, R. Peña, G. M. Asher, J. Clare, and R. Blasco-Giménez, “Control strategies for power smoothing using a flywheel driven by a sensorless vector-controlled induction machine operating in a wide speed range,” *IEEE Trans. Ind. Electron.*, vol. 51, no. 3, pp. 603-614, 2004.
 - [116] N. W. Miller. (2014). *GE Experience with Turbine Integrated Battery Energy Storage* [Online]. Available: <http://www.ieee-pes.org/presentations/gm2014/PESGM2014P-000717.pdf>
 - [117] *IEEE 1547 - IEEE Standard for Interconnecting Distributed Resources with Electric Power Systems*, 2003.
 - [118] Y. Liu, Y. Li, Y. Chi, and W. Wang, “Analysis on a large scale wind turbines cascading trip-off accident in North China,” in *Proc. IEEE PowerTech*, 2013, pp. 1-6.
 - [119] W. Qureshi, G. Demler, and N.-K. Nair, “Developing transmission fault ride-through criteria for New Zealand wind farms,” in *Proc. IEEE PESGM*, 2011, pp. 1-7.
 - [120] R. Seguin, J. Woyak, D. Costyk, J. Hambrick, and B. Mather, “High-penetration PV integration handbook for distribution engineers,” *National Renewable Energy Laboratory, Golden, CO NREL/TP-5D00-63114*, 2016.
 - [121] T. Ackermann, A. Ellis, J. Fortmann, J. Matevosyan, E. Muljadi, R. Piwko, P. Pourbeik, E. Quitmann, P. Sorensen, and H. Urdal, “Code shift: Grid specifications and dynamic wind turbine models,” *IEEE Power and Energy Magazine*, vol. 11, no. 6, pp. 72-82, 2013.
 - [122] F. Iov, A. D. Hansen, P. Sørensen, and N. A. Cutululis, “Mapping of grid faults and grid codes,” Technical University of Denmark, Risø National Laboratory, 2007.
 - [123] J. Alipoor, Y. Miura, and T. Ise, “Power system stabilization using virtual synchronous generator with alternating moment of inertia,” *IEEE Trans. Emerg. Sel. Topics Power Electron.*, vol. 3, no. 2, pp. 451-458, 2015.
 - [124] X. Hou, H. Han, C. Zhong, W. Yuan, M. Yi, and Y. Chen, “Improvement of transient stability in inverter-based AC microgrid via adaptive virtual inertia,” in *Proc. IEEE*

- ECCE, 2016, pp. 1-6.
- [125] P. Hu, H. Chen, K. Cao, Y. Hu, D. Kai, L. Chen, and Y. Wang, "Coordinated Control of Multiple Virtual Synchronous Generators in Mitigating Power Oscillation," *Energies*, vol. 11, no. 10, p. 2788, 2018.
 - [126] R. Shi, X. Zhang, C. Hu, H. Xu, J. Gu, and W. Cao, "Self-tuning virtual synchronous generator control for improving frequency stability in autonomous photovoltaic-diesel microgrids," *Journal of Modern Power Systems and Clean Energy*, vol. 6, no. 3, pp. 482-494, 2018.
 - [127] S. Wang, R. Qi, and Y. Li, "Fuzzy Control Scheme of Virtual Inertia for Synchronverter in Micro-Grid," in *Proc. IEEE ICEMS*, 2018, pp. 2028-2032.
 - [128] P. Rodriguez, A. Luna, R. Munoz-Aguilar, F. Corcoles, R. Teodorescu, and F. Blaabjerg, "Control of power converters in distributed generation applications under grid fault conditions," in *Proc. IEEE ECCE*, 2011, pp. 2649-2656.
 - [129] X. Yu and Z. Jiang, "Dynamic current limiting control of voltage source inverters," in *Proc. IEEE IEMDC*, 2009, pp. 1664-1668.
 - [130] A. Gkountaras, S. Dieckerhoff, and T. Sezi, "Evaluation of current limiting methods for grid forming inverters in medium voltage microgrids," in *Proc. IEEE ECCE*, 2015, pp. 1223-1230.
 - [131] G. Denis, T. Prevost, M.-S. Debry, F. Xavier, X. Guillaud, and A. Menze, "The Migrate project: the challenges of operating a transmission grid with only inverter-based generation. A grid-forming control improvement with transient current-limiting control," *IET Renewable Power Generation*, vol. 12, no. 5, pp. 523-529, 2018.
 - [132] H. Wu and X. Wang, "Transient stability impact of the phase-locked loop on grid-connected voltage source converters," in *Proc. IEEE IPEC*, 2018, pp. 2673-2680.
 - [133] H. Wu and X. Wang, "Transient angle stability analysis of grid-connected converters with the first-order active power loop," in *Proc. IEEE APEC*, 2018, pp. 3011-3016.
 - [134] H. Wu and X. Wang, "Design-Oriented Transient Stability Analysis of Grid-Connected Converters with Power Synchronization Control," *IEEE Trans. Ind. Electron.*, pp. 6473-6482, 2018.
 - [135] H. Xin, L. Huang, L. Zhang, Z. Wang, and J. Hu, "Synchronous instability mechanism of Pf droop-controlled voltage source converter caused by current saturation," *IEEE Trans. Power Syst.*, vol. 31, no. 6, pp. 5206-5207, 2016.
 - [136] Y. Ma, L. Yang, J. Wang, F. Wang, and L. M. Tolbert, "Emulating full-converter wind turbine by a single converter in a multiple converter based emulation system," in *Proc. IEEE APEC*, 2014, pp. 3042-3047.
 - [137] F. Deng and Z. Chen, "Power control of permanent magnet generator based variable speed wind turbines," in *Proc. IEEE ICEMS*, 2009, pp. 1-6.

- [138] Y. Ma, L. Yang, F. Wang, and L. M. Tolbert, "Voltage closed-loop virtual synchronous generator control of full converter wind turbine for grid-connected and stand-alone operation," in *Proc. IEEE APEC*, 2016, pp. 1261-1266.
- [139] Y. Ma, W. Cao, L. Yang, F. Wang, and L. M. Tolbert, "Virtual synchronous generator control of full converter wind turbines with short-term energy storage," *IEEE Trans. Ind. Electron.*, vol. 64, no. 11, pp. 8821-8831, 2017.
- [140] A. D. Paquette and D. M. Divan, "Virtual impedance current limiting for inverters in microgrids with synchronous generators," *IEEE Trans. Ind. Appl.*, vol. 51, no. 2, pp. 1630-1638, 2015.
- [141] X. Chen, X. Ruan, D. Yang, H. Wu, and W. Zhao, "Step-by-step controller design of voltage closed-loop control for virtual synchronous generator," in *Proc. IEEE ECCE*, 2015, pp. 3760-3765.
- [142] J. Sun, "Impedance-based stability criterion for grid-connected inverters," *IEEE Trans. Power Electron.*, vol. 26, no. 11, p. 3075, 2011.
- [143] X. Dou, X. Quan, Z. Wu, M. Hu, J. Sun, K. Yang, and M. Xu, "Improved control strategy for microgrid ultracapacitor energy storage systems," *Energies*, vol. 7, no. 12, pp. 8095-8115, 2014.
- [144] A. Forsyth, C. Jia, D. Wu, C. Tan, S. Dimler, Y. Yang, and W. Bailey, "Cryogenic converter for superconducting coil control," *IET Power Electronics*, vol. 5, no. 6, pp. 739-746, 2012.
- [145] A. D. Hansen and G. Michalke, "Modelling and control of variable - speed multi - pole permanent magnet synchronous generator wind turbine," *Wind Energy*, vol. 11, no. 5, pp. 537-554, 2008.
- [146] M. Chinchilla, S. Arnaltes, and J. C. Burgos, "Control of permanent-magnet generators applied to variable-speed wind-energy systems connected to the grid," *IEEE Trans. Energy Convers.*, vol. 21, no. 1, pp. 130-135, 2006.
- [147] B. Wu, Y. Lang, N. Zargari, and S. Kouro, *Power conversion and control of wind energy systems*. John Wiley & Sons, 2011.
- [148] K. Clark, N. W. Miller, and J. J. Sanchez-Gasca, "Modeling of GE wind turbine-generators for grid studies," GE Energy, 2010.
- [149] Y.-K. Wu and J.-S. Hong, "A literature review of wind forecasting technology in the world," in *Proc. IEEE Power Tech*, 2007, pp. 504-509.
- [150] E. Muljadi and C. P. Butterfield, "Pitch-controlled variable-speed wind turbine generation," *IEEE Trans. Ind. Appl.*, vol. 37, no. 1, pp. 240-246, 2001.
- [151] N. Kelley and B. Jonkman. (2015). *TurbSim: A stochastic, full-field, turbulence simulator primarily for use with InflowWind/AeroDyn-based simulation tools*, [Online]. Available: <https://nwtc.nrel.gov/TurbSim>

- [152] WECC off-nominal frequency load shedding plan, [Online]. Available: <https://www.wecc.biz>
- [153] T. Athay, R. Podmore, and S. Virmani, "A practical method for the direct analysis of transient stability," *IEEE Trans. Power App. Syst.*, no. 2, pp. 573-584, 1979.
- [154] F. Zhang, Y. Sun, L. Cheng, X. Li, J. H. Chow, and W. Zhao, "Measurement and modeling of delays in wide-area closed-loop control systems," *IEEE Trans. Power Syst.*, vol. 30, no. 5, pp. 2426-2433, 2015.
- [155] I. Alvarado, "Deterministic Communications in Distributed Data Acquisition and Control Systems for Smart Energy Applications," presented at the IEEE APEC, 2018.
- [156] M. E. Smith Jr, "Evaluation of IEEE 802.1 Time Sensitive Networking Performance for Microgrid and Smart Grid Power System Applications," M. S. Thesis, Dept. Elec. Engr. and Comp. Sci., Univ. of Tenn., Knoxville, 2018.
- [157] Y. Zhang, P. Markham, T. Xia, L. Chen, Y. Ye, Z. Wu, Z. Yuan, L. Wang, J. Bank, and J. Burgett, "Wide-area frequency monitoring network (FNET) architecture and applications," *IEEE Trans. Smart Grid*, vol. 1, no. 2, pp. 159-167, 2010.
- [158] J. Zhao, Y. Tang, and V. Terzija, "Robust Online Estimation of Power System Center of Inertia Frequency," *IEEE Trans. Power Syst.*, 2018.
- [159] Q.-C. Zhong and G. C. Konstantopoulos, "Current-limiting droop control of grid-connected inverters," *IEEE Trans. Ind. Electron.*, vol. 64, no. 7, pp. 5963-5973, 2016.

Vita

Yiwei Ma received the B.S. degree and M.S. degree from Tsinghua University, Beijing, China, in 2009 and 2011, both in electrical engineering. He started his Ph.D. study in 2011 at the Center for Ultra-wide-area Resilient Electric Energy Transmission Networks (CURENT), The University of Tennessee, Knoxville, where he received the Ph.D. degree in 2019.